

1977

Interpretation of neutron noise spectra measured in the presence of fluctuating voids

Massoud Nabavian
Iowa State University

Follow this and additional works at: <https://lib.dr.iastate.edu/rtd>

 Part of the [Nuclear Engineering Commons](#), and the [Oil, Gas, and Energy Commons](#)

Recommended Citation

Nabavian, Massoud, "Interpretation of neutron noise spectra measured in the presence of fluctuating voids " (1977). *Retrospective Theses and Dissertations*. 5837.
<https://lib.dr.iastate.edu/rtd/5837>

This Dissertation is brought to you for free and open access by the Iowa State University Capstones, Theses and Dissertations at Iowa State University Digital Repository. It has been accepted for inclusion in Retrospective Theses and Dissertations by an authorized administrator of Iowa State University Digital Repository. For more information, please contact digirep@iastate.edu.

INFORMATION TO USERS

This material was produced from a microfilm copy of the original document. While the most advanced technological means to photograph and reproduce this document have been used, the quality is heavily dependent upon the quality of the original submitted.

The following explanation of techniques is provided to help you understand markings or patterns which may appear on this reproduction.

1. The sign or "target" for pages apparently lacking from the document photographed is "Missing Page(s)". If it was possible to obtain the missing page(s) or section, they are spliced into the film along with adjacent pages. This may have necessitated cutting thru an image and duplicating adjacent pages to insure you complete continuity:
2. When an image on the film is obliterated with a large round black mark, it is an indication that the photographer suspected that the copy may have moved during exposure and thus cause a blurred image. You will find a good image of the page in the adjacent frame.
3. When a map, drawing or chart, etc., was part of the material being photographed the photographer followed a definite method in "sectioning" the material. It is customary to begin photoing at the upper left hand corner of a large sheet and to continue photoing from left to right in equal sections with a small overlap. If necessary, sectioning is continued again — beginning below the first row and continuing on until complete.
4. The majority of users indicate that the textual content is of greatest value, however, a somewhat higher quality reproduction could be made from "photographs" if essential to the understanding of the dissertation. Silver prints of "photographs" may be ordered at additional charge by writing the Order Department, giving the catalog number, title, author and specific pages you wish reproduced.
5. PLEASE NOTE: Some pages may have indistinct print. Filmed as received.

University Microfilms International

300 North Zeeb Road
Ann Arbor, Michigan 48106 USA
St. John's Road, Tyler's Green
High Wycombe, Bucks, England HP10 8HR

77-16,968

NABAVIAN, Massoud, 1949-
INTERPRETATION OF NEUTRON NOISE
SPECTRA MEASURED IN THE PRESENCE
OF FLUCTUATING VOIDS.

Iowa State University, Ph.D., 1977
Engineering, nuclear

Xerox University Microfilms, Ann Arbor, Michigan 48106

**Interpretation of neutron noise spectra measured
in the presence of fluctuating voids**

by

Massoud Nabavian

**A Dissertation Submitted to the
Graduate Faculty in Partial Fulfillment of
The Requirements for the Degree of
DOCTOR OF PHILOSOPHY**

**Department: Chemical Engineering and
Nuclear Engineering
Major: Nuclear Engineering**

Approved:

Signature was redacted for privacy.

In Charge of Major Work

Signature was redacted for privacy.

For the Major Department

Signature was redacted for privacy.

For the Graduate College

**Iowa State University
Ames, Iowa**

1977

TABLE OF CONTENTS

	Page
NOMENCLATURE	ix
I. INTRODUCTION	1
II. LITERATURE REVIEW	4
III. THEORY	13
A. Multiple Reactivity Input and Multiple Feedback System	13
1. Spectral density of neutron fluctuations	13
2. Spectral density of detector current fluctuations	15
B. Local Perturbations and their Effect on Observed Spectra	17
1. Fluctuations in void fraction in a boiling channel and its auto- and cross-spectra	18
2. Fluctuations in flux, and finite volume of sensitivity	20
3. Fluctuations in detector current, and effect of finite detector size	21
C. Single Detector Measurement System	26
D. Two Detector Measurement System	31
1. The cross-spectral density function	31
2. The transfer function	34
3. The coherence function	37
IV. EXPERIMENTAL APPARATUS	41
A. The Reactor System	41
B. The Experimental Channel	41
C. The Signal Processing System	45
D. System for Equipment Transfer Function Measurement	45

	Page
V. EXPERIMENTAL PROCEDURES	49
A. Modes of Operation	49
B. Signal Conditioning	50
C. Calculation of Spectra	51
VI. EXPERIMENTAL RESULTS	52
A. Flux Measurements	52
B. System Checks	54
1. Single frequency signals	54
2. White noise signals	56
C. Neutron Noise Measurements in Absense of any Artificially Introduced Perturbation	60
1. Test of stationarity of reactor noise signals	60
2. Reactor noise spectra	62
D. Measurements with Air Bubbles as the Source of Induced Perturbations	71
1. Test of stationarity of neutron noise signals	72
2. Effect of air flow rate on the neutron noise spectra	74
3. Finite volume of sensitivity study	79
4. Pulsating air flow measurements	81
5. Phase angle measurements	83
6. The coherence function	88
E. Measurements with Boiling as the Source of Induced Perturbation	90
1. Measurements with a single heater	91
2. Measurements with three heaters	91

	Page
VII. DISCUSSION AND CONCLUSIONS	97
VIII. SUGGESTIONS FOR FUTURE WORK	101
IX. LITERATURE CITED	103
X. ACKNOWLEDGMENTS	107
XI. APPENDIX A: POWER SPECTRAL DENSITY OF THE FLUCTUATIONS IN THE NEUTRON DENSITY OF THE REACTOR SYSTEM OF FIG. 1	108
XII. APPENDIX B: VOID FRACTION FLUCTUATIONS AND THEIR AUTO- AND CROSS-SPECTRA	114
A. Void Fraction Fluctuations	114
B. The Auto- and Cross-Spectra of Void Fraction Fluctuations	117
XIII. APPENDIX C: FLUCTUATIONS IN FLUX AS A FUNCTION OF FLUCTUATIONS IN VOID FRACTION	123
XIV. APPENDIX D: AUTO- AND CROSS-SPECTRAL DENSITIES OF DETECTOR CURRENT FLUCTUATIONS DUE TO FLUCTUATIONS IN LOCAL VOID FRACTION	131
XV. APPENDIX E: ALGORITHM FOR THE CALCULATION OF SPECTRA	138

LIST OF TABLES

Table	Page
1. Results of neutron flux measurements inside the experimental channel	53
E-1. Frequency resolutions and normalized standard errors for the measured spectra	143

LIST OF FIGURES

Figure	Page
1. Reactor noise source and reactor kinetic model	14
2. The local transfer function for $d = 0.1524$ m, $\mu = 25\text{m}^{-1}$, and $V = 0.24$ m/s	27
3. The local transfer function for $d = 0.0762$ m, $\mu = 12.5\text{m}^{-1}$, and $V = 0.24$ m/s	28
4. Theoretical transfer function or coherence function	40
5. The position of the experimental channel in the ALRR reactor	42
6. Schematic diagram of the boiling channel	43
7. Signal processing system	46
8. Block diagram of the system for transfer function measurement	47
9. APSD plot for a set of input frequencies from 1 to 10 Hz, in 1 Hz steps	55
10. APSD plot for wide-band white noise as input signal and anti-aliasing filter set at 10 Hz	57
11. Magnitude of the transfer function of the anti- aliasing filter B with cut-off frequency set at 1 Hz	58
12. Comparison of measured phase of anti-aliasing filter with manufacturer's specifications	59
13. Test of stationarity of neutron noise signals in the unperturbed case	61
14. The NAPSD of the fluctuations in the signal of detector A in the unperturbed case	63
15. The NAPSD of the fluctuations in the signal of detector B in the unperturbed case	64

Figure	Page
16. The NCPSD of the fluctuations in the signals of detectors A and B in the unperturbed case	66
17. The phase difference of the detector signals in the unperturbed case	67
18. The transfer function in the unperturbed case	68
19. The coherence function in the unperturbed case with the detectors at the same level	69
20. The coherence function in the unperturbed case with the detectors separated by 12 inches	70
21. Test of stationarity of neutron noise signals in the presence of air bubbles	73
22. NMSV as a function of air flow rate	75
23. Multiple NAPSD plot showing the variation of NAPSD with air flow rate	76
24. The local NAPSD for the case of 0.34 cfpm of air flow	78
25. NMSV's of detector current fluctuations as a function of detector center-line position	80
26. The NAPSD for an air pulsing frequency of 0.72 Hz	82
27. The NAPSD for an air pulsing frequency of 1.89 Hz	84
28. The coherence function for detector separation of 12 inches and air flow rate of 0.34 cfpm	86
29. Phase angle versus frequency for three detector separation distances	87
30. The coherence function for detector separation of 12 inches and air flow rate of 0.0659 cfpm	89
31. The NAPSD of detector A for the case of boiling with three heaters	92

Figure	Page
32. The NAPSD of detector B for the case of boiling with three heaters	93
33. The coherence function for detector separation of 12 inches and boiling with three heaters	94
34. Phase angle vs. frequency for the case of boiling with three heaters	96

NOMENCLATURE

Acronyms

ACF	Auto Correlation Function
ALRR	Ames Laboratory Research Reactor
APSD	Auto-Power Spectral Density
BWR	Boiling Water Reactor
CCF	Cross Correlation Function
CHRNCF	Coherence Function
CPSD	Cross-Power Spectral Density
LWR	Light Water Reactor
NAPSD	Normalized Auto-Power Spectral Density
NAAPSD	NAPSD of signal of detector A
NBAPSD	NAPSD of signal of detector B
NCPSD	Normalized Cross-Power Spectral Density
NMSV	Normalized Mean Square Value
NRMS	Normalized Root Mean Square
PHASE	Phase of the CPSD function
PWR	Pressurized Water Reactor
TRNSFN	Transfer function

Roman

		<u>units</u>
A	Cross sectional area	$\frac{m^2}{m}$
A_v	Avogadro's number	
$b(z, t, v)$	Fluctuating part of bubble number density	bubbles/ m^3

<u>Roman</u>		<u>units</u>
$B(z, t, v)$	Bubble number density	bubbles/m ³
$B_o(z, v)$	Mean bubble number density	bubbles/m ³
$B_e = \frac{1}{T}$	Resolution bandwidth	Hz
$c_i(t)$	Fluctuating part of the delayed neutron precursor number density of group i	nuclei/m ³
$C_i(t)$	Delayed neutron precursor number density of group i	nuclei/m ³
C_{io}	Steady state delayed neutron precursor number density of group i	nuclei/m ³
$\tilde{C}_{xy}(k)$	Real part of CPSD function	
d	Detector length	m
$D = \frac{\sqrt{2} - \bar{v}}{\bar{v}^2}$	Diven factor	
$\bar{D}(z, t)$	Diffusion coefficient	m
$\bar{D}(z)$	Time averaged diffusion coefficient	m
\bar{D}	Time and space averaged diffusion coefficient	m
$\delta\bar{D}(z, t)$	Fluctuating component of diffusion coefficient	m
E	Expectation operator	
f	Frequency	Hz
f_c	Nyquist or folding frequency	Hz
f_n	Null frequency	Hz
f_o	Corner or break frequency	Hz
f_s	Analog to digital sampling rate	s ⁻¹

<u>Roman</u>		<u>unit</u>
$F = \frac{N_0}{\nu \ell}$	Fission rate	fissions/s
$g(z, t, v)$	Fluctuating component of bubble source	bubbles/m ³ -s
$G(z, t, v)$	Bubble source	bubbles/m ³ -s
$G_0(z, t)$	Time averaged bubble source	bubbles/m ³ -s
$\tilde{G}(k)$	Raw estimate of APSD	
$G(k)$	Smoothed estimate of APSD	
h	Time interval between samples	s
$h_m(t)$	Feedback kernel	
$h_0(t)$	Zero-power reactor impulse response function	
$H_m(\omega)$	Feedback transfer function	ρ /neutrons
$H_r(\omega)$	Reactivity transfer function	neutrons
$H_{r0}(\omega)$	Zero-power reactivity transfer function	neutrons
$H_s(\omega)$	Source transfer function	s
$H_{s0}(\omega)$	Zero-power source transfer function	s
$H_\mu(\omega)$	Finite volume of sensitivity transfer function	
$H_d(\omega)$	Finite detector size transfer function	
$H_\ell(\omega) = H_\mu(\omega)H_d(\omega)$	Local effect transfer function	
$H_{12}(\omega)$	Input output transfer function	
$i = \sqrt{-1}$	Imaginary number	
i	Delayed neutron group number	
$i(z, t)$	Fluctuating component of detector current	A

<u>Roman</u>		<u>units</u>
$i(z, \omega)$	Fourier transform of $i(z, t)$	A
$\bar{I} = W\bar{q}F$	Mean current output of fission chamber	A
$j(z, t, v)$	Fluctuating component of bubble current density	bubbles/m ² -s
$J(z, t, v)$	Bubble current density	bubbles/m ² -s
$J_0(z, v)$	Time averaged bubble current density	bubbles/m ² -s
k	Neutron multiplication factor	
δk	Fluctuations in k	
$K(\omega)$	Ratio of local to global NAPSD functions	
λ	Prompt neutron lifetime	s
L	Thermal neutron diffusion length	m
m_v	Mass of voids per unit volume	kg/m ³
m_w	Mass of water per unit volume	kg/m ³
M	Molecular weight	kg
$n(t)$	Fluctuating component of neutron density	neutrons/m ³
$N(t)$	Neutron density	neutrons/m ³
N_0	Time averaged neutron density	neutrons/m ³
\bar{q}	Average charge produced in a fission chamber per neutron detected	C/neutron
Q	Void flow rate	m ³ /s
\tilde{Q}_{xy}	Raw estimate of the imaginary part of CPSD	
Q_{xy}	Smoothed estimate of the imaginary part of CPSD	

<u>Roman</u>		<u>units</u>
$R_{g',g''}$	CCF of g' and g''	
$R_{\alpha}(z, \epsilon)$	ACF of void fraction fluctuation	
$s=i\omega$	Laplace transform variable	radians/s
t	Time	s
T	Length of data segment	s
T_{12}	Bubble transit time between positions z_1 and z_2	s
$u(t)$	Noise equivalent source	neutrons/m ³ -s
$U(t)$	Neutron source density	neutrons/m ³ -s
U_0	Time averaged neutron source density	neutrons/m ³ -s
v	Volume of bubble	m ³
v_m	Maximum bubble volume	m ³
$V(z)$	Speed of bubbles at position z along the channel	m/s
$\bar{V}(z)$	Bubble speed averaged over the volume of sensitivity centered at z	m/s
\bar{V}_{12}	Mean bubble speed between positions z_1 and z_2	m/s
\bar{V}	Mean bubble speed	m/s
V_v	Specific volume of void	
V_w	Specific volume of water	
$w(t)$	Window function	
W	Detector efficiency	detections/ fission
$x(n)$	Signal of detector A	
$X(k)$	Fourier transform of $x(n)$	

<u>Roman</u>		<u>units</u>
$y(n)$	Signal of detector B	
$Y(k)$	Fourier transform of $y(n)$	
z	position along the experimental channel	m
$z(n)$	Complex record $x(n)+iy(n)$	
$Z(k)$	Fourier transform of $z(n)$	
 <u>Greek</u>		
$\alpha = \frac{V_v}{V_w + V_v}$	Void fraction	
$\alpha(z)$	Mean void fraction at z	
$\alpha(z, t)$	Fluctuating component of void fraction at z	
$\alpha(z, \omega)$	Fourier transform of $\alpha(z, t)$	
β	Total delayed neutron fraction	
β_i	Delayed neutron fraction of group i	
$\gamma^2(\omega)$	The coherence function	
δ	Designates perturbation in time domain	
$\delta(\epsilon)$	Delta function at ϵ	
$\theta(\omega)$	Phase of NCPSD function	radians
λ	Delayed neutron precursor decay constant	s^{-1}
λ_i	Delayed neutron precursor decay constant of group i	s^{-1}
$\Lambda = \frac{\rho}{k}$	Prompt neutron generation time	s
$\mu = \frac{1}{L}$		m^{-1}
ν	Neutrons produced per fission	neutrons/ fission

<u>Greek</u>		<u>units</u>
ρ	Reactivity	$\delta k/k$
$\rho_f(t)$	Feedback reactivity	$\delta k/k$
$\rho_k(t)$	Extraneous reactivity	$\delta k/k$
$\rho_t(t)$	Total reactivity	$\delta k/k$
$\rho_u(t)$	Noise equivalent reactivity source	$\delta k/k$
$\bar{\rho}$	Density	kg/m^3
Σ	Summation symbol	
σ_a	Microscopic absorption cross section	m^2
$\bar{\Sigma}_a(z, t)$	Macroscopic absorption cross section	m^{-1}
$\bar{\Sigma}_a(z)$	Time averaged macroscopic absorption cross section	m^{-1}
$\bar{\Sigma}_a$	Time and space averaged macroscopic absorption cross section	m^{-1}
τ_{z_1, z_2}	Bubble transit time between positions z_1 and z_2	 s
$\tau_d = \frac{d}{2\bar{V}}$	Detector length time constant	s
$\tau_\mu = \frac{1}{\mu\bar{V}}$	Volume of sensitivity time constant	s
v_n	Thermal neutron speed	m/s
ϕ_z	Time and space averaged neutron flux at z	$\text{neutrons/m}^2\text{-s}$
$\phi(z)$	Time averaged neutron flux	"
$\phi(z, t)$	Thermal neutron flux	"
$\delta\phi(z, t)$	Fluctuating component of neutron flux	"

<u>Greek</u>		<u>units</u>
$\delta\phi(z, s)$	Laplace transform of $\phi(z, t)$	neutrons/m ² -s
$\delta\phi(z, \omega)$	Fourier transform of $\phi(z, t)$	"
$\phi_g(z, \omega, v)$	APSD of fluctuations in bubble source	$\frac{\text{bubbles/m}^3\text{-s}}{\text{Hz}}$
$\phi_i(z, \omega)$	APSD of detector current fluctuations	A ² /Hz
$\bar{\phi}_i(z, \omega)$	NAPSD of detector current fluctuations	Hz ⁻¹
$\phi_{i,gl}(\omega)$	APSD of detector current fluctuations due to fluctuations in global neutron density	A ² /Hz
$\bar{\phi}_{i,gl}(\omega)$	NAPSD of detector current fluctuations due to fluctuations in global neutron density	Hz ⁻¹
$\phi_{i,l}(z, \omega)$	APSD of detector current fluctuations due to local fluctuations in neutron flux	A ² /Hz
$\bar{\phi}_{i,l}(z, \omega)$	NAPSD of detector current fluctuations due to local fluctuations in neutron flux	Hz ⁻¹
$\phi_{n,gl}(\omega)$	APSD of global neutron density fluctuations	neutron ² /Hz
$\phi_u(\omega)$	APSD of noise equivalent source	neutron ² /s
$\phi_\alpha(z, \omega)$	APSD of fluctuations in void fraction	Hz ⁻¹
$\phi_\rho(\omega)$	APSD of total reactivity driving force	ρ^2 /Hz
$\phi_{\rho_k}(\omega)$	APSD of extraneous reactivity fluctuation ρ_k	ρ^2 /Hz
$\phi_{\rho_u}(\omega)$	APSD of reactivity equivalent source	ρ^2 /Hz
$\psi_{i;z_1,z_2}(\omega)$	CPSD of detector current fluctuations for detectors at z_1 and z_2	A ² /Hz
$\bar{\psi}_{i;z_1,z_2}(\omega)$	NCPSD of detector current fluctuations for detectors at z_1 and z_2	Hz ⁻¹

<u>Greek</u>		<u>units</u>
$\psi_{i,\ell; z_1, z_2}(\omega)$	CPSD of detector current fluctuations due to local fluctuations in flux for detectors at z_1 and z_2	A^2/Hz
$\Psi_{\alpha; z_1 z_2}(\omega)$	CPSD of fluctuations in void fraction at positions z_1 and z_2	Hz^{-1}
$\omega=2\pi f$	Frequency	radians/s
$\omega_n = \frac{n\pi}{\tau_d}$	Null frequency	"
$\omega_o = \frac{1}{\tau_\mu}$	Corner frequency	"

I. INTRODUCTION

In a boiling water reactor, the steam void content and its fluctuations play an important role in the dynamic behavior of local and global thermodynamic properties of the reactor, and hence the respective neutronic properties of the system.

Investigation of fluctuations in neutron flux at various positions in the reactor can thus yield useful information on localized and combined thermohydraulic conditions of the reactor. This information is very useful in the routine operation of the reactor, and can be used to identify any deviations from normal operating conditions of the system.

In recent neutron noise studies in large boiling water reactors the trend has been to distinguish between a global noise source caused primarily by the reactivity fluctuations of the whole reactor system, and a local noise source caused by fluctuations in void fraction in the vicinity of the neutron detector. The spectral density of the fluctuations in the detector current has been accordingly assumed to be the sum of the spectral densities of the detector current fluctuations caused by the global and local perturbations in neutron flux.

The spectral density of detector current fluctuations due to the global noise source in an at-power reactor has

been determined in a recent theoretical study to be proportional to the product of the square magnitude of the reactor transfer function and the spectral density of reactivity fluctuations of the whole reactor.

The spectral density of detector current fluctuations, due to local perturbations in void fraction, has been exhibited in recent theoretical investigations to be proportional to the spectral density of void fraction fluctuations (which is assumed to be white) modified by a local transfer function. The local transfer function takes into account a finite volume of sensitivity for the effect of void fluctuations on the fluctuations of local neutron flux, and the effect of a detector of finite size.

Experimental measurements in some boiling water reactors have revealed that when the local spectral density exceeds the global spectral density significantly, the void speed in a coolant channel can be inferred from the phase lag between the signals of two axially displaced neutron detectors in the channel. It has also been pointed out by some investigators that the phase lag between the detectors has characteristic effects on the magnitude of the cross-spectral density and the coherence functions of the detector signals, from which the void speed may be inferred.

To study neutron noise spectra in the presence of

fluctuating voids, under controlled experimental conditions, an experimental coolant channel placed in the thermal column of the Ames Laboratory Research Reactor is used. The design of the channel allows controlled introduction of voids in the form of air and steam bubbles, which can be studied with two independently moveable neutron detectors.

The objectives of the present study are to unify the theories of several authors for the global and local noise sources in a boiling water reactor coolant channel, and to describe the observed spectral properties of neutron noise signals obtained from measurements in the experimental coolant channel under various experimental conditions.

II. LITERATURE REVIEW

Historically there has been considerable interest in the detection of boiling in light water nuclear power reactors (LWR's).

Saxe [24, 25] argued that the ability to detect the onset of boiling in some water moderated reactors would be of value in that it would make it possible for these reactors to be operated at a higher power than would otherwise be considered because of the danger of boiling burnout. He pointed out that boiling may be detectable due to fluctuations in void fraction and bubble volume which in turn cause fluctuations in neutron flux. He expected the effect of boiling to be a general increase of neutron noise over a wide frequency range, due to irregular bubble size and location of formation with time.

Initially many boiling detection experiments were performed in research reactors. Boyd [6] was one of the very first investigators to claim detection of nucleate boiling by an ion chamber. He used electrically heated ribbons wrapped around an ion chamber inside a research reactor to produce boiling. He observed increased fluctuations on the ion chamber signal as the result of boiling.

Colomb and Binford [8] used an electrical heater to produce boiling in a research reactor. They were able to

produce detectable effects on the acoustic characteristics but the results of neutron noise measurements were inconclusive.

Rajagopal [22] made neutron noise measurements in the Saxton pressurized water reactor (PWR). He observed a resonance peak in the auto-power spectral densities (APSD's) of in-core and out-of-core ion chamber current fluctuations between 10 to 20 Hz. He attributed the peak to the onset of boiling in the reactor.

Binford [3] used neutron noise methods to detect boiling in an orificed fuel element in the Oak Ridge research reactor. He found that the onset of boiling gave rise to violent oscillations of the neutron flux at a frequency of around 2 Hz.

Jordan [12] used a special fuel assembly which was orificed to reduce coolant flow to cause boiling of the coolant. The APSD curve of the neutron detector current fluctuations exhibited a multiple peak structure over the frequency range of 0.2 to 2.5 Hz, suggesting that the disturbance consisted of a set of pulses of fixed frequency width and amplitude.

Nomura [19] presented a theoretical model describing neutron fluctuations in a boiling water reactor (BWR). His model postulated the existence of "shot noise" associated

with the process of heat transfer to the coolant, where a "shot" is the formation of a bubble due to the transfer of a quantity of heat from the fuel element to the coolant. He concluded that the predominant neutron noise source in a BWR is steam generation and the associated fluctuation of void fraction due to the discrete nature of the steam bubbles discharging into the coolant.

Thie [31] in reporting the results of noise measurements at the Pathfinder Nuclear Power Plant pointed out that at frequencies higher than 0.5 Hz an ion chamber placed high in the core detected more noise than a lower one because of increased local steam void fluctuations in its environment.

Mogil'ner [18] developed a theory describing neutron noise due to bubble circulation in a nuclear reactor, and concluded that the fluctuations of neutron flux should increase both with increasing concentration of bubbles and increasing bubble size. He also concluded that the spectral composition of the neutron noise should be a sensitive characteristic of the velocity of bubbles in the reactor.

Albrecht [1] used a water channel inserted in a research reactor to introduce air bubbles. He observed that the coherence function between the signals of two neutron detectors, which were placed outside the core on the

opposite sides of the source increased proportionally with air flow rate.

Seifritz [28] made neutron noise measurements on the Lingen BWR. He observed that the shape of the APSD functions changed from a low pass filter characteristic in the lower part of the reactor (nonboiling zone) to a band pass filter characteristic in the middle and upper parts of the reactor (bulk boiling zone). In addition the relative root mean square noise intensity of the total flux fluctuations increased for the higher detector position over that for the lower position.

Seifritz and Cioli [29] were the first investigators to report void speed measurements in a BWR. They observed linear change of the phase of the cross-power spectral density (CPSD) function as a function of frequency for two neutron detectors separated from each other in elevation. This observation indicated a constant time lag between the two detector signals from which void speed could be calculated. They also observed that the APSD's of the detector current fluctuations normalized by the mean detector current (NAPSD's) increased at the higher frequency ($1 < f < 10$ Hz) end in the upper part of the core due to enhanced boiling. They also observed that the coherence function between the detector signals decreased with increasing frequency and

with increasing distance between detectors.

Stegemann et al. [30] suggested using neutron noise measurements in BWR's to gain information about the mode of boiling and flow rate in a reactor coolant channel. They argued that fluctuations in neutron density, as observed by a detector inside a BWR, are caused in part by fluctuations in void content in the vicinity of the detector. The detected fluctuations should thus give a measure of the steam void fraction and boiling intensity in the respective core regions. They also pointed out that a characteristic quantity proportional to noise amplitude is the normalized root mean square (NRMS) of the detector signal. They also argued that the average steam void velocity in the reactor can be estimated from the phase of the CPSD function.

Rothman [23] developed a theoretical model to show that bubble noise should dominate in most BWR's, and be clearly detectable. He considered bubble noise to be a local phenomenon with each neutron detector responding mainly to local neutron fluctuations stemming from local voidage variations. He also argued that the effect of a finite detector size on the measured fluctuations is that of reduced observed noise due to averaging out of local void fluctuations over the volume of the detector. He also pointed out that the fluctuations in the flux should diminish exponentially with distance from the source of fluctua-

tions.

Wach and Kosaly [33] observed that phase angle measurements in the Lingen BWR showed characteristic deviations from a simple linear variation with frequency. They developed a simple space dependent model and introduced the concept of local and global driving sources of the neutron noise in a large BWR, and investigated their joint effect on detector signals. They suggested that the local noise component results from disturbances in the vicinity of the detector while the global component is driven by the at-power reactor as a whole. With these assumptions, they observed that the gain of the transfer function or the coherence function between the signals of two axially neighboring incore ion chambers shows characteristic dips at equal frequency intervals, the positions of which are governed by the time interval for the steam bubbles to travel between the two detectors. They also observed that the degree of deviation of the phase angle from a linear behavior with respect to frequency is dependent on the ratio of the local and the global APSD components.

Kosaly et al. [15] developed a phenomenological model for the local component of fluctuations in the neutron field by assuming that it is caused primarily by fluctuations in the local steam-void content. The model was

further developed by showing that the fluctuations in the local steam-void content are white, i.e., frequency independent. The APSD of local fluctuations was then found to be directly proportional to local void fraction and mean bubble volume, and inversely proportional to the speed of bubbles at the point of observation. Their model was also used to predict the behavior of the NRMS value of detector current fluctuations measured along a boiling channel. They found fair agreement between their model and the experimental results from the Lingen BWR.

Kosaly [13] attempted to put the model for the local component of BWR noise source on a stronger theoretical footing by application of two-group diffusion theory. He solved the diffusion equations by considering propagating disturbances of moderator density. The main thrust of his work was to show that the noise produced by fluctuations in the steam void content is localized, or in other words, there is a finite volume of sensitivity beyond which the effect of the disturbances will be very small. He found the relaxation length associated with this finite volume to be of the order of the thermal neutron diffusion length in the medium.

Kosaly and Mesko [14] studied the effect of finite detector size on observed spectra in conjunction with a

finite volume of sensitivity consideration. They developed a theoretical representation of observable spectra by assuming a relaxation length for the effect of local perturbations, and integration of the fluctuations in neutron flux over the length of the detector.

Lu et al. [17], in an experiment based on the transmission of a thermal neutron beam through a water channel containing air or steam voids, found that the response of a fission chamber in the beam was dependent on the bubble size and flow conditions in the channel. In particular, they could verify that:

1. The fluctuations of air voids in the water channel were comparable to those of steam voids.
2. The void fluctuations were time- and space-dependent.
3. The void generation rate and size were the major factors in the void fluctuation characteristics.
4. The APSD functions were quite sensitive to the two-phase flow regime in the channel.

The objectives of the present study are to extend the work of Lu et al. [17] by employing an experimental reactor channel model which can be inserted in the Ames Laboratory Research Reactor (ALRR) to obtain a more uniform neutron field environment. In addition it is expected that the provision for two moveable detectors in the experimental

channel will allow cross-spectrum and phase angle measurements which can be used to test the validity of the basic theoretical representation to be developed.

III. THEORY

A. Multiple Reactivity Input and Multiple Feedback System

1. Spectral density of neutron fluctuations

A linear delayed critical reactor system, including feedback mechanisms, responding to extraneous reactivity inputs $\rho_k(t)$ and a noise equivalent reactivity source $\rho_u(t)$ is considered. A block diagram of this system which was suggested by Seifritz [27] is shown in Fig. 1.

The components of the reactivity vector, $\rho_k(t)$, are assumed to be K stationary stochastic reactivity driving forces (in $\delta k/k$ units) with zero mathematical expectation, i.e.:

$$\overline{\rho_k(t)} = 0, \quad k = 1, 2, \dots, K.$$

It is further assumed that these components are correlated among one another, i.e.:

$$\rho_i \rho_j^* (\omega) \neq 0, \quad i, j = 1, 2, \dots, K.$$

where '*' denotes complex conjugation.

The noise equivalent reactivity source, $\rho_u(t)$, accounts for the reactivity fluctuations due to branching processes within the neutron chains.

The reactor system is assumed to possess a zero power

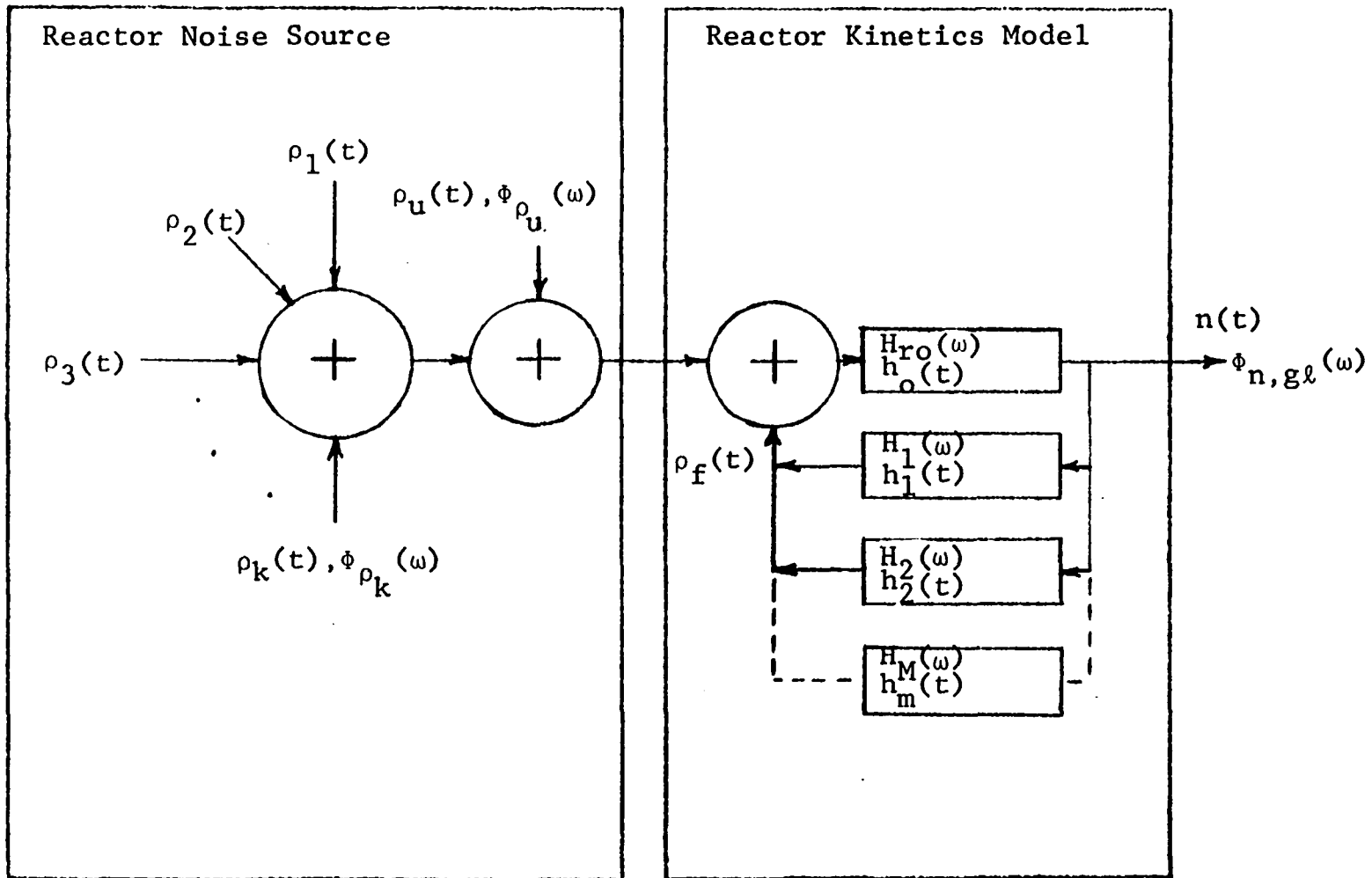


Figure 1. Reactor noise source and reactor kinetic model

transfer function, $H_{r0}(\omega)$, and M parallel feedback paths, $H_1(\omega), H_2(\omega), \dots, H_M(\omega)$.

The power spectral density of the fluctuations in the neutron density of the reactor system of Fig. 1 is shown in Appendix A to be

$$\phi_{n,gl}(\omega) = |H_r(\omega)|^2 [\phi_{\rho}(\omega) + \phi_{\rho_u}(\omega)], \quad (1)$$

where $H_r(\omega)$ is the reactivity transfer function of the reactor system, $\phi_{\rho}(\omega)$ is the spectral density of reactivity fluctuations, and $\phi_{\rho_u}(\omega)$ is the spectral density of the noise equivalent reactivity [7], given by

$$\phi_{\rho_u}(\omega) = \frac{\ell \bar{v} D}{N_0}, \quad (2)$$

where N_0 is the steady state neutron density, ℓ is the prompt neutron lifetime, \bar{v} is the average number of neutrons released per fission, and D is the Diven factor defined as

$$D = \frac{\bar{v}^2 - \bar{v}}{\bar{v}^2} \quad (3)$$

2. Spectral density of detector current fluctuations

The spectral density of the fluctuations in the current output of a fission chamber placed in the reactor is given by Cohn [7] as

$$\phi_{i,gl}(\omega) = \frac{\bar{q}^2 W N_0}{\ell \bar{v}} + \frac{W^2 \bar{q}^2}{\bar{v}^2 \ell^2} \phi_{n,gl}(\omega), \quad (4)$$

where \bar{q} is the average charge produced in the detector per neutron absorbed and W is the detector efficiency with units of detections per fission.

With the application of Eqs. 1 and 2, Eq. 4 can be written as

$$\begin{aligned} \phi_{i,gl}(\omega) = & \bar{q}^2 WF + \frac{W^2 \bar{q}^2}{\ell^2} F^2 |H_S(\omega)|^2 \phi_\rho(\omega) \\ & + \frac{W^2 \bar{q}^2 D}{\ell} F |H_S(\omega)|^2, \end{aligned} \quad (5)$$

where

$$F = \frac{N_0}{\bar{v}\ell} \quad (6)$$

is the fission rate in the reactor, and $H_S(\omega) = (\ell/N_0)H_Y(\omega)$ is the source transfer function.

The first term in Eq. 5 accounts for the statistics of detection process, the second term accounts for the reactivity fluctuations in the system, and the third term accounts for pile noise fluctuations due to the fission branching processes.

In Eq. 5 the first and the third terms are proportional to the fission rate while the second term is proportional to the square of fission rate, and hence reactor power. Thus for an at-power reactor Eq. 5 can be approximated as

$$\phi_{i,gl}(\omega) \approx \frac{\bar{I}^2}{\ell^2} |H_S(\omega)|^2 \phi_\rho(\omega), \quad (7)$$

where

$$\bar{I} = W\bar{q}F$$

is the mean detector current, and where the terms proportional to the first power of the fission rate have been neglected.

The implication of Eq. 7 is that for an at-power reactor the spectral density of detector current fluctuations is proportional to the square magnitude of the at-power reactor transfer function with its implied feedback loops, and the spectral density of reactivity fluctuations in the reactor. Specifically, the zero-power characteristics of the reactor should not be observable.

B. Local Perturbations and their Effect on Observed Spectra

In this section a model for the fluctuations in the void fraction in a boiling channel of a reactor is presented. The fluctuations in void fraction are then linked to the fluctuations in the neutron flux in their immediate vicinity. Finally the detection of fluctuations in the neutron flux by a finite-size neutron detector is considered.

1. Fluctuations in void fraction in a boiling channel and its auto- and cross-spectra

The fluctuations in void fraction at a position z_2 along the boiling channel is shown in Appendix B to be given by

$$\alpha(z_2, t) = \frac{V(z_1)}{V(z_2)} \alpha(z_1, t - \tau_{z_1, z_2}) + \alpha'(z_1, z_2, t) \quad (8)$$

where $V(z_1)$ and $V(z_2)$ are bubble speeds at positions z_1 and z_2 ($z_2 > z_1$) respectively, $\alpha(z_1, t - \tau_{z_1, z_2})$ is the fluctuating component of void fraction at z_1 , τ_{z_1, z_2} is the bubble travel time between z_1 and z_2 , and $\alpha'(z_1, z_2, t)$ represents the fluctuations in void fraction produced between positions z_1 and z_2 .

The implication of Eq. 8 is that any fluctuations in void fraction at a position z_1 along the boiling channel will be observable at a higher position z_2 , with a time delay τ_{z_1, z_2} , along with extraneous fluctuations in void fraction produced between the two points.

A shortcoming of Eq. 8 is that it does not explicitly account for any bubble volume variation along the channel.

The auto-spectral density of void fraction fluctuations at any position along the voided channel is shown in Appendix B to be given by the simple expression

$$\phi_{\alpha}(z, \omega) = C \frac{\alpha(z) \overline{v(z)}}{\overline{V(z)}} \quad (9)$$

where $\alpha(z)$ is the steady state void fraction, $\overline{v(z)}$ is the mean bubble volume at the point of observation and C is a constant.

The major consequence of Eq. 9 is that the spectral density of void fraction fluctuations is frequency independent, and thus white. Furthermore the spectral density of void fraction fluctuation is directly proportional to steady state void fraction, and inversely proportional to bubble speed at the point of observation. The term $\overline{v(z)}$ may be assumed to be a constant if the mean bubble volume at a fixed position z along the channel is constant. However as the void fraction increases in the channel, bubbles can coalesce to form bubbles of larger volume, so that $\overline{v(z)}$ may increase with increasing void fraction. Thus, the auto-spectral density of void fraction fluctuations may increase in a nonlinear manner with increasing void fraction in a channel which has a geometry that allows formation of large bubbles.

The cross-spectral density function of void fraction fluctuations at two axial positions z_1 and z_2 ($z_2 > z_1$) is shown in Appendix B to be given by

$$\psi_{\alpha; z_1, z_2}(\omega) = C \frac{\alpha(z_1) \overline{v(z_1)}}{\overline{V(z_2)}} e^{-i\omega\tau_{z_1, z_2}} \quad (10)$$

The implication of Eq. 10 is that the amplitude of the cross-spectral density function of void fraction fluctuations at positions z_1 and z_2 is equal to the auto-spectral density of void fraction fluctuations at z_1 .

More importantly the phase of the cross-spectral density function is a linear function of frequency with a slope equal to the bubble travel time between the two observation points.

2. Fluctuations in flux, and finite volume of sensitivity

To formulate an expression for the localized fluctuations in neutron flux caused by fluctuations in void fraction, the time-dependent diffusion equation for thermal neutrons in a medium without any neutron sources [16] is used as

$$\bar{D}\nabla^2\phi(z,t) - \bar{\Sigma}_a(z,t)\phi(z,t) = \frac{1}{v_n} \frac{\partial\phi(z,t)}{\partial t} \quad (11)$$

In Eq. 11, \bar{D} is the diffusion coefficient, ϕ is the neutron flux, $\bar{\Sigma}_a$ is the macroscopic absorption cross section, v_n is neutron speed, z is the position along the coolant channel and t stands for time.

It is shown in Appendix C that the fluctuations in flux in frequency domain as a function of fluctuations in void fraction can be found by solving Eq. 11, and is given by

$$\delta\phi(z, \omega) = \frac{C_1\phi_z}{2\mu\bar{D}} \int_{-\infty}^z e^{-\mu(z-x)} \alpha(x, \omega) dx + \frac{C_1\phi_z}{2\mu\bar{D}} \int_z^{\infty} e^{-\mu(x-z)} \alpha(x, \omega) dx, \quad (12)$$

where ϕ_z is a constant flux and \bar{D} a constant diffusion coefficient over the volume of sensitivity at z , $\mu = 1/L$ where L is the diffusion length of neutrons, and C_1 is a constant.

An important implication of Eq. 12 is that depending on the value of μ ($\mu \sim 25 \text{ m}^{-1}$ for water) the fluctuations in flux are only sensitive to the fluctuations in void fraction near the point of observation. Thus, a so-called volume of sensitivity around the point of observation can be envisioned beyond which the fluctuations in void fraction will not significantly affect the fluctuations of flux at the point of observation.

3. Fluctuations in detector current, and effect of finite detector size

To arrive at the fluctuations in detector current which are caused by fluctuations in neutron flux due to fluctuations in void fraction, a neutron flux detector of length d which is placed in the coolant channel is considered.

For a detector centered at position z along the channel the fluctuations in output current can be written as

$$i(z, t) = C \int_{z-\frac{d}{2}}^{z+\frac{d}{2}} \delta\phi(z', t) dz', \quad (13)$$

where C is a constant of proportionality.

If Eq. 13 is transformed to the frequency domain, and Eq. 12 is used for fluctuations in flux, the result is

$$i(z, \omega) = C\phi_z \int_{z-\frac{d}{2}}^{z+\frac{d}{2}} \left\{ \int_{-\infty}^{z'} e^{-\mu(z'-x)} \alpha(x, \omega) dx + \int_{z'}^{\infty} e^{-\mu(x-z')} \alpha(x, \omega) dx \right\} dz'. \quad (14)$$

The normalized auto-power spectral density of detector current fluctuations can be evaluated from Eq. 14, as shown in Appendix D, and is given by

$$\bar{\Phi}_{i, \ell}(z, \omega) = C \frac{\alpha(z) \overline{V(z)}}{V(z)} H_{\mu}(\omega) H_d(\omega), \quad (15)$$

where

$$H_{\mu}(\omega) = \frac{1}{(1 + \omega^2 \tau_n^2)^2}, \quad (16)$$

and

$$H_d(\omega) = \frac{\sin^2(\omega \tau_d)}{(\omega \tau_d)^2}, \quad (17)$$

where

$$\tau_{\mu} = \frac{1}{\mu V}, \quad (18)$$

and

$$\tau_d = \frac{d}{2\bar{V}} \quad (19)$$

are time constants associated with the volume of sensitivity and detector length respectively, in which \bar{V} is a mean bubble speed along the channel.

The normalized cross-spectral density function of current fluctuations of two detectors placed at positions z_1 and z_2 along the channel is shown in Appendix D to be given by

$$\bar{\psi}_{i,\ell;z_1,z_2}(\omega) = C \frac{\alpha(z_1)\overline{v(z_1)}}{V(z_2)} H_\mu(\omega)H_d(\omega)e^{-i\omega T_{12}}. \quad (20)$$

In Eq. 20 the quantity

$$T_{12} = \frac{z_2 - z_1}{\bar{V}_{12}}, \quad z_2 > z_1 \quad (21)$$

is the bubble travel time between positions z_1 and z_2 , where \bar{V}_{12} is the mean bubble speed between z_1 and z_2 .

To study the behavior of the auto- and cross-spectral density functions of detector current fluctuations, as defined by Eqs. 15 and 20, the behavior of Eqs. 16 and 17 need to be studied.

The term $H_\mu(\omega)$ has a corner frequency of $\omega_0 = \frac{1}{\tau_\mu}$, at which the amplitude is approximately 12 decibels (dB) below the low frequency asymptote. For frequencies $\omega > \omega_0$, $H_\mu(\omega)$ approaches an asymptote which decreases at the rate of

80 dB per decade increase in frequency.

The behavior of $H_d(\omega)$ is dictated by the time constant τ_d . For small values of τ_d and low frequencies $H_d(\omega)$ does not deviate much from unity. However as frequency increases the numerator of $H_d(\omega)$ becomes zero at null frequencies

$$\omega_n = \frac{n\pi}{\tau_d}, \quad n = 0, 1, 2, \dots, \quad (22)$$

the position of which are dictated by the value of τ_d .

To obtain a graphic view of the effect of $H_\mu(\omega)$ and $H_d(\omega)$ a local transfer function is defined as

$$H_\rho(\omega) = H_\mu(\omega)H_d(\omega), \quad (23)$$

which is shown in Figs. 2 and 3 for two representative sets of parameter values.

For the plot of Fig. 2 the parametric values used are

$$d = 0.1524 \text{ m},$$

$$\mu = \frac{1}{L} = 25 \text{ m}^{-1},$$

and

$$V = 0.24 \text{ m/s}.$$

To study the effect of change in detector size and diffusion length on $H_\rho(\omega)$ the following parametric values are used for the plot of Fig. 3:

$$d = 0.0762 \text{ m},$$

$$\mu = \frac{1}{L} = 12.5 \text{ m}^{-1}$$

and

$$V = 0.24 \text{ m/s}.$$

A frequency step of 0.025 Hz is used in both plots.

The plots show the gross behavior of $H_{\mu}(\omega)$, which has a low-pass filter property, on which the behavior of $H_d(\omega)$ is superimposed.

A comparison of Figs. 2 and 3 shows that as the detector length is reduced by a factor of 2 the position of the first null value of $H_{\lambda}(\omega)$ is moved to a frequency higher by a factor of 2. The same effect can be obtained by increasing the bubble speed V by a factor of 2. Thus if small-sized detectors are used and bubble speed is increased significantly the null values of $H_{\lambda}(\omega)$ may fall beyond the range of observed frequencies.

Further comparison of Figs. 2 and 3 shows that an increase in diffusion length by a factor of 2 moves the break frequency of $H_{\lambda}(\omega)$ back by a factor of 2 in frequency. However, an increase in bubble speed will move the break frequency of $H_{\lambda}(\omega)$ to higher frequencies. Since the neutron diffusion length increases with void fraction it can be concluded that as the void fraction is increased the break frequency of $H_{\lambda}(\omega)$ will move to lower frequencies.

It can be seen from Figs. 2 and 3 that the null values of $H_{\ell}(\omega)$ occur over a very narrow frequency band. Thus a measurement system with a high frequency resolution is needed to resolve the null values of $H_{\ell}(\omega)$. Furthermore, due to rapid roll-off of $H_{\ell}(\omega)$ after the break frequency a system with a very high dynamic range will be needed to resolve null values of $H_{\ell}(\omega)$ over background noise.

C. Single Detector Measurement System

If a single neutron detector is placed in a boiling channel of a nuclear reactor, it will respond to both the global reactivity fluctuations of the whole reactor system, and local fluctuations in void fraction.

The spectral density of the detector current fluctuations for this case can be written as

$$\Phi_i(z, \omega) = \Phi_{i,gl}(\omega) + \Phi_{i,\ell}(z, \omega) \quad . \quad (24)$$

In Eq. 24, $\Phi_{i,gl}(\omega)$ is the spectral density of detector current fluctuations caused mainly by the reactivity fluctuations of the whole reactor system, and $\Phi_{i,\ell}(z, \omega)$ is the spectral density of detector current fluctuations, caused by fluctuations in local void fraction.

With the application of Eqs. 7 and 15, $\Phi_i(z, \omega)$ normalized with the square of mean detector current can be written as

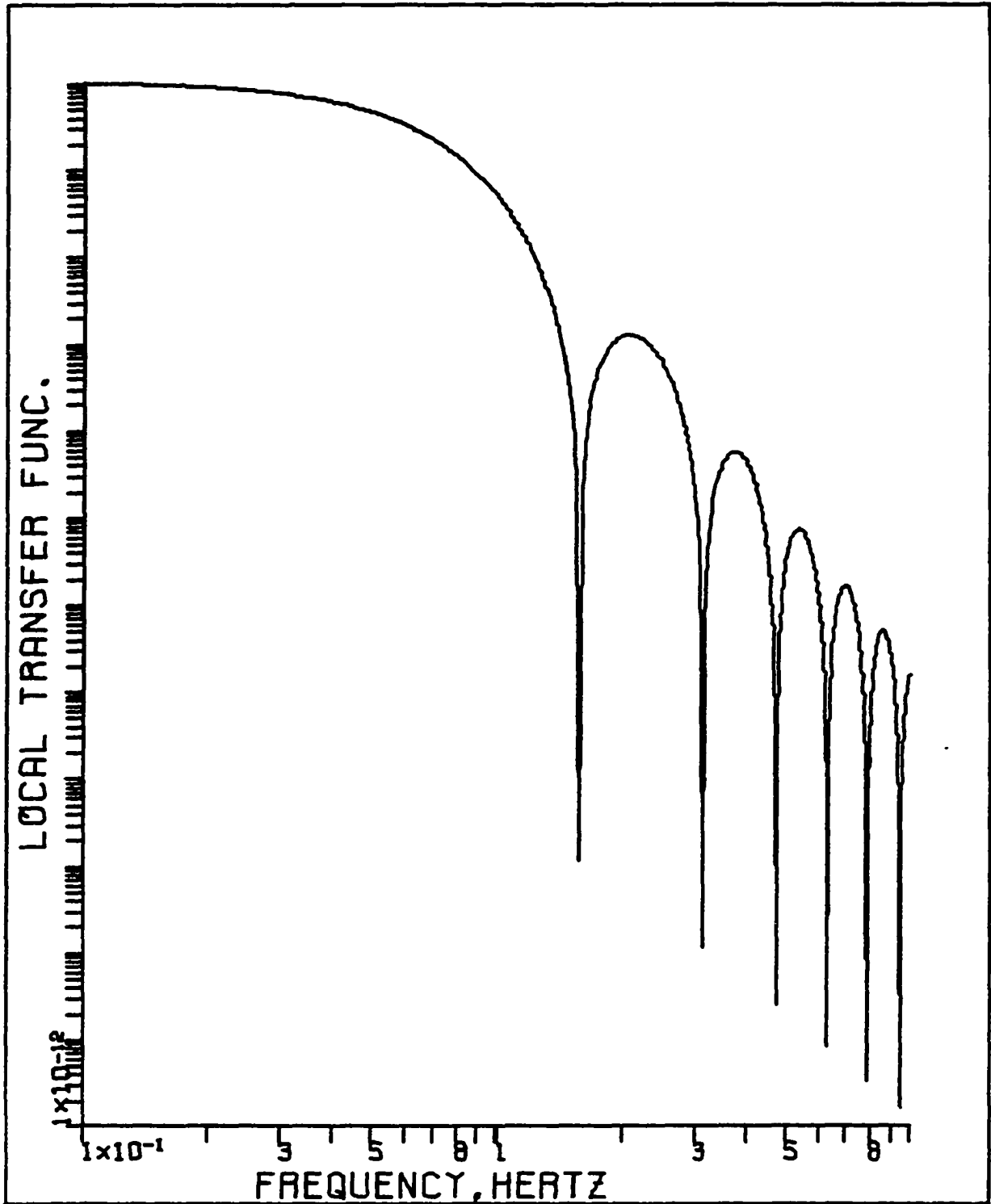


Figure 2. The local transfer function for $d = 0.1524$ m, $\mu = 25 \text{ m}^{-1}$, and $V = 0.24$ m/s

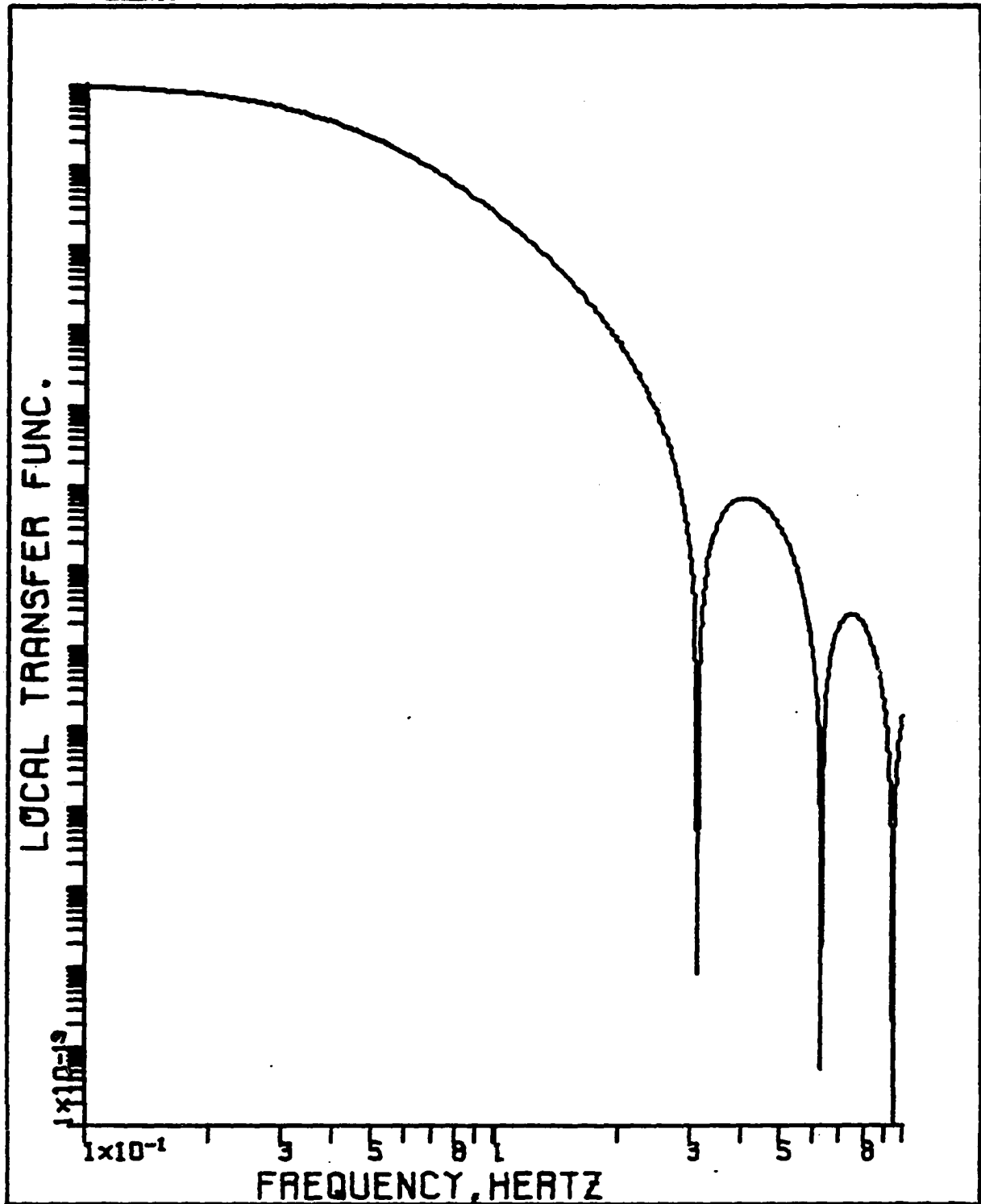


Figure 3. The local transfer function for $d = 0.0762$ m, $\mu = 12.5$ m⁻¹, and $V = 0.24$ m/s

$$\bar{\Phi}_i(z, \omega) = \frac{1}{2} |H_s(\omega)|^2 \Phi_\rho(\omega) + C \frac{\alpha(z) \overline{v(z)}}{V(z)} H_\ell(\omega), \quad (25)$$

where Eq. 23 has been used.

According to Eq. 25 the normalized auto-power spectral density (NAPSD) of detector current fluctuations is equal to the sum of global and local NAPSD's. The actual behavior of $\bar{\Phi}_i(z, \omega)$ is dictated by the relative magnitude of global and local contributions to the fluctuations in flux observed by the detector. In particular if the void fraction in the vicinity of the detector is increased to the point that the second term in Eq. 25 becomes dominant over the first term, then the spectral characteristic of $\bar{\Phi}_i(z, \omega)$ will be determined by the function $H_\ell(\omega)$. On the other hand if no voids are introduced in the channel the spectral characteristics of the reactor noise defined by the first term in Eq. 25 can be studied.

To study the behavior of $\bar{\Phi}_i(z, \omega)$ as a function of void fraction, the mean-square value of detector current fluctuations is used. The mean square value is proportional to the area under the APSD curve [2, 9].

The normalized mean-square value of detector current fluctuations can be written as

$$\text{NMSV}(z) = \frac{\overline{i^2(z,t)}}{\overline{I^2(z)}} = \frac{1}{2\pi} \int_{-\infty}^{\infty} \overline{\phi}_i(z,\omega) d\omega. \quad (26)$$

With the application of Eq. 25, Eq. 26 can be written as

$$\text{NMSV}(z) = C_1 \frac{\alpha(z)\overline{V(z)}}{V(z)} + C_2, \quad (27)$$

where

$$C_1 = \frac{C}{2\pi} \int_{-\infty}^{\infty} H_\ell(\omega) d\omega,$$

and

$$C_2 = \frac{1}{2\pi\ell^2} \int_{-\infty}^{\infty} |H_s(\omega)|^2 \phi_\rho(\omega) d\omega$$

are assumed to be constants,

The void fraction at any position in the channel can be written as

$$\alpha(z) = \frac{Q(z)}{A(z)V(z)}, \quad (28)$$

where $Q(z)$ is void flow rate, and $A(z)$ is the cross sectional area of the channel.

At any fixed position along the channel $A(z)$ and $V(z)$ are constant, so that Eq. 28 can be written as

$$\alpha(z_0) = C_3 Q(z_0), \quad (29)$$

which when inserted in Eq. 27 yields

$$\text{NMSV}(z_0) = C_4 Q(z_0) \overline{v(z_0)} + C_2 . \quad (30)$$

Eq. 30 implies that the NMSV at any fixed position z_0 along the channel is directly proportional to void flow rate at z_0 . The term $\overline{v(z_0)}$ may be assumed to be a constant for a fixed position z_0 along the channel.

However, when the flow rate increases in the channel, small bubbles can coalesce to form bubbles of larger volume, so that $\overline{v(z_0)}$ may increase with increasing void flow rate. Thus $\text{NMSV}(z_0)$ may increase in a nonlinear manner with increasing void flow rate, provided the channel geometry allows formation of large bubbles.

D. Two Detector Measurement System

1. The cross-spectral density function

If two neutron detectors are placed in a boiling channel of a nuclear reactor, and the signals from them are cross-correlated, the cross-spectral density function of the two signals can be written as

$$\Psi_{i; z_1, z_2}(\omega) = \phi_{i, gl}(\omega) + \Psi_{i, l; z_1, z_2}(\omega). \quad (31)$$

In Eq. 31 $\phi_{i, gl}(\omega)$ is the spectral density of detector current fluctuations, caused mainly by the reactivity

fluctuations of the whole reactor system, as given by Eq. 7, and is common to both detectors.

The term $\Psi_{i,\ell; z_1, z_2}(\omega)$ in Eq. 31 is the cross-spectral density function of detector current fluctuations due to fluctuations in local void fraction for two detectors centered at positions z_1 and z_2 along the coolant channel and is defined by Eq. 20.

With the application of Eq. 20 the normalized cross-spectral density (NCPD) function can be deduced from Eq. 31 as

$$\bar{\Psi}_{i, z_1, z_2}(\omega) = \bar{\Phi}_{i, g\ell}(\omega) + C \frac{\alpha(z_1)\overline{v(z_1)}}{V(z_2)} H_\ell(\omega) e^{-i\omega T_{12}}. \quad (32)$$

The NCPD function of Eq. 32 has a phase value given by

$$\theta(\omega) = \tan^{-1} \left[- \frac{\sin \omega T_{12}}{\frac{1}{K_{12}(\omega)} + \cos \omega T_{12}} \right], \quad (33)$$

where

$$K_{12}(\omega) = \frac{C \frac{\alpha(z_1)\overline{v(z_1)}}{V(z_2)} H_\ell(\omega)}{\bar{\Phi}_{i, g\ell}(\omega)} \quad (34)$$

is the ratio of local and global spectra.

If the local void fraction is large so that the local spectrum is much greater in magnitude than the global

spectrum, i.e., $K_{12}(\omega) \gg 1$, Eq. 33 can be approximated as

$$\theta(\omega) \approx -\omega T_{12}. \quad (35)$$

The implication of Eq. 35 is that the void travel time between detector positions z_1 and z_2 can be found from the slope of the plot of the phase angle of NCPSD function vs. frequency. If the distance between the detectors is known, then the mean void speed between the detectors is given by

$$\bar{V}_{12} = \frac{z_2 - z_1}{T_{12}}. \quad (36)$$

If the condition $K_{12}(\omega) \gg 1$ is not met, then the behavior of the phase function is described by Eq. 33. For $K_{12}(\omega) > 1$ the phase function will oscillate around a line described by Eq. 35. For $K_{12}(\omega) \leq 1$ the phase function will oscillate around the line $\theta = 0$. The behavior of the phase function can be more erratic due to the fact that $K_{12}(\omega)$ is a frequency dependent function.

In the absence of any local voids the NCPSD function of Eq. 32 best describes the spectral characteristics of the reactor noise since all the uncorrelated noise signals will be eliminated. In the more general case when local voids are present the properties of the amplitude of the NCPSD function can be better described by the introduction of a so-called input-output transfer function.

2. The transfer function

A transfer function can be defined for the two detector system by the following formula

$$H_{12}(\omega) = \frac{\bar{\Psi}_{i, z_1, z_2}(\omega)}{\bar{\Phi}_i(z_1, \omega)}. \quad (37)$$

With the use of Eqs. 25 and 32 the transfer function can be written as

$$H_{12}(\omega) = \frac{\bar{\Phi}_{i, g\ell}(\omega) + C \frac{\alpha(z_1) \overline{v(z_1)}}{V(z_2)} H_\ell(\omega) e^{-i\omega T_{12}}}{\bar{\Phi}_{i, g\ell}(\omega) + C \frac{\alpha(z_1) \overline{v(z_1)}}{V(z_1)} H_\ell(\omega)}, \quad (38)$$

which can be written as

$$H_{12}(\omega) = \frac{1 + K_{12}(\omega) e^{-i\omega T_{12}}}{1 + K_1(\omega)}, \quad (39)$$

where $K_{12}(\omega)$ is defined by Eq. 34 and $K_1(\omega)$ is given by

$$K_1(\omega) = \frac{C \frac{\alpha(z_1) \overline{v(z_1)}}{V(z_1)} H_\ell(\omega)}{\bar{\Phi}_{i, g\ell}(\omega)}. \quad (40)$$

The square magnitude of the transfer function can be seen from Eq. 39 to be given by

$$|H_{12}(\omega)|^2 = \frac{[1+K_{12}(\omega)\cos \omega T_{12}]^2 + K_{12}^2(\omega)\sin^2 \omega T_{12}}{[1+K_1(\omega)]^2},$$

which can be written in the form

$$|H_{12}(\omega)|^2 = \frac{[1+K_{12}(\omega)]^2 - 2K_{12}(\omega)(1-\cos \omega T_{12})}{[1+K_1(\omega)]^2}. \quad (41)$$

For $\cos \omega T_{12} = 1$, $|H_{12}(\omega)|^2$ has the maxima

$$|H_{12}(\omega)|_{\max}^2 = \frac{[1+K_{12}(\omega)]^2}{[1+K_1(\omega)]^2},$$

at frequencies

$$\omega_{\max} = \frac{2n\pi}{T_{12}}, \quad n = 0, 1, 2, \dots \quad (42)$$

For $\cos \omega T_{12} = -1$, $|H_{12}(\omega)|^2$ has the minima

$$|H_{12}(\omega)|_{\min}^2 = \frac{[1-K_{12}(\omega)]^2}{[1+K_1(\omega)]^2},$$

at frequencies

$$\omega_{\min} = \frac{(2n+1)\pi}{T_{12}}, \quad n = 0, 1, 2, \dots \quad (43)$$

In section B.3 it was noted that $H_{\rho}(\omega)$ becomes zero at null frequencies

$$\omega_n = \frac{n\pi}{\tau_d}, \quad n = 0, 1, 2, \dots$$

For these null frequencies both K_1 and K_{12} become zero, and it can be seen from Eq. 39 that

$$H_{12}(\omega) = 1, \quad \omega = \frac{n\pi}{\tau_d}, \quad n = 0, 1, 2, \dots \quad (44)$$

It may be possible to deduce the void travel time T_{12} between the two detectors and hence the mean bubble speed at axial position between the detectors from the location of maxima and minima of the transfer functions and use of Eqs. 42 and 43.

But it should be noted that in addition to the extrema at frequencies defined by Eqs. 42, and 43, the transfer function will have maxima at frequencies defined by Eq. 44. Furthermore, there will be fluctuations caused by the statistical variability of the measured transfer function.

It thus may not be possible to separate the desired maxima and minima from the profusion of fluctuations that may be present in a measured transfer function.

3. The coherence function

The coherence function for the two detector system is given by

$$\gamma_{12}^2(\omega) = \frac{|\bar{\Psi}_{i; z_1, z_2}(\omega)|^2}{\bar{\Phi}_i(z_1, \omega) \cdot \bar{\Phi}_i(z_2, \omega)}, \quad (45)$$

which with the use of Eqs. 25 and 32 can be written as

$$\gamma_{12}^2(\omega) = \frac{[1+K_{12}(\omega)]^2 - 2K_{12}(\omega)(1-\cos \omega T_{12})}{[1+K_1(\omega)][1+K_2(\omega)]}, \quad (46)$$

where K_{12} and K_1 are as defined by Eqs. 34 and 40, and K_2 is given by

$$K_2(\omega) = \frac{C \frac{\alpha(z_2) \overline{v(z_2)}}{V(z_2)} H_\ell(\omega)}{\bar{\Phi}_{i, g\ell}(\omega)}. \quad (47)$$

The coherence function has properties similar to those for the transfer function. Specifically the coherence function has the maxima

$$\gamma_{12, \max}^2(\omega) = \frac{[1+K_{12}(\omega)]^2}{[1+K_1(\omega)][1+K_2(\omega)]},$$

at frequencies

$$\omega_{\max} = \frac{2n\pi}{T_{12}}, \quad n = 0, 1, 2, \dots,$$

and the minima

$$\gamma_{12}^2(\omega) = \frac{[1 - K_{12}(\omega)]^2}{[1 + K_1(\omega)][1 + K_2(\omega)]},$$

at frequencies

$$\omega_{\min} = \frac{(2n+1)\pi}{T_{12}}, \quad n = 0, 1, 2, \dots$$

Also similar to the transfer function, for $H_\ell(\omega) = 0$, K_1 , K_2 , and K_{12} will be zero so that

$$\gamma_{12}^2(\omega) = 1$$

at frequencies

$$\omega_n = \frac{n\pi}{\tau_d}, \quad n = 0, 1, 2, \dots$$

To study the behavior of the magnitude of the transfer function and/or the coherence function a plot of Eqs. 41 and/or 46 for the case of $K_1 = K_2 = K_{12} = K$ is given in Fig. 4. A simplified model for K is used as

$$K = C_0 \frac{H_\ell(\omega)}{\frac{1}{\omega^2}},$$

where the global spectrum is assumed to have a $1/\omega^2$ behavior

and the constant C_0 is chosen such that $K = 100$ at 1 Hz.

Eq. 41 is then plotted using the following parametric values

$$d = 0.0762 \text{ m},$$

$$\mu = 12.5 \text{ m}^{-1},$$

$$V = 0.24 \text{ m/s},$$

and

$$T_{12} = \frac{0.3048 \text{ m}}{0.24 \text{ m/s}} = 1.27 \text{ s}.$$

The position of the maxima and minima in Fig. 4 do not exactly match the theoretical values given by Eqs. 42, 43, and 44. This discrepancy occurs due to the fact that the function K has not been assumed to be a constant independent of frequency.

Thus, the task of predicting T_{12} from the position of the extrema of the transfer or coherence function may not produce correct results if K is a strong function of frequency.

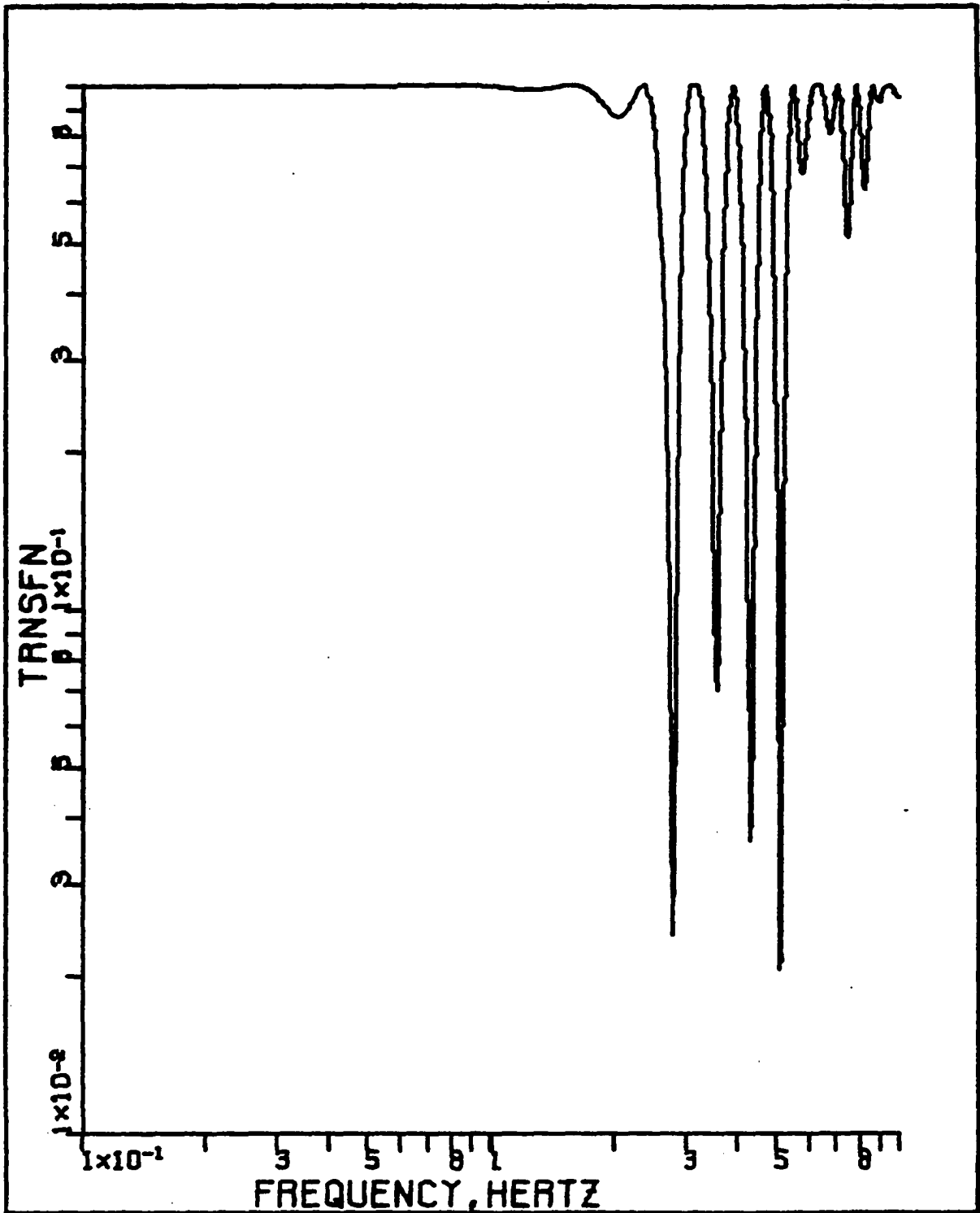


Figure 4. Theoretical transfer function or coherence function

IV. EXPERIMENTAL APPARATUS

A. The Reactor System

The experiments were carried out at the Ames Laboratory Research Reactor (ALRR). The ALRR is a 5 MW uranium fueled (enriched in U-235) D₂O moderated research reactor. The position of the experimental channel in the reactor is indicated in Fig. 5. This particular location at the end of the thermal column was chosen in accordance to space requirements, and due to the fact that the neutron flux at the end of thermal column is almost totally thermalized (cadmium ratio = 2300).

B. The Experimental Channel

The experimental channel was designed to simulate a detector channel and its surrounding voided environment.

A section of the experimental channel is shown schematically in Fig. 6. The channel contains two dry tubes in which two neutron detectors can freely move along the length of the channel. The neutron detectors are fission chambers (Westinghouse 6376) with a sensitive length of approximately 6 inches and a thermal neutron sensitivity of approximately 1.4×10^{-13} amperes/neutron/cm²/s. The detector tubes are surrounded by an annular water channel.

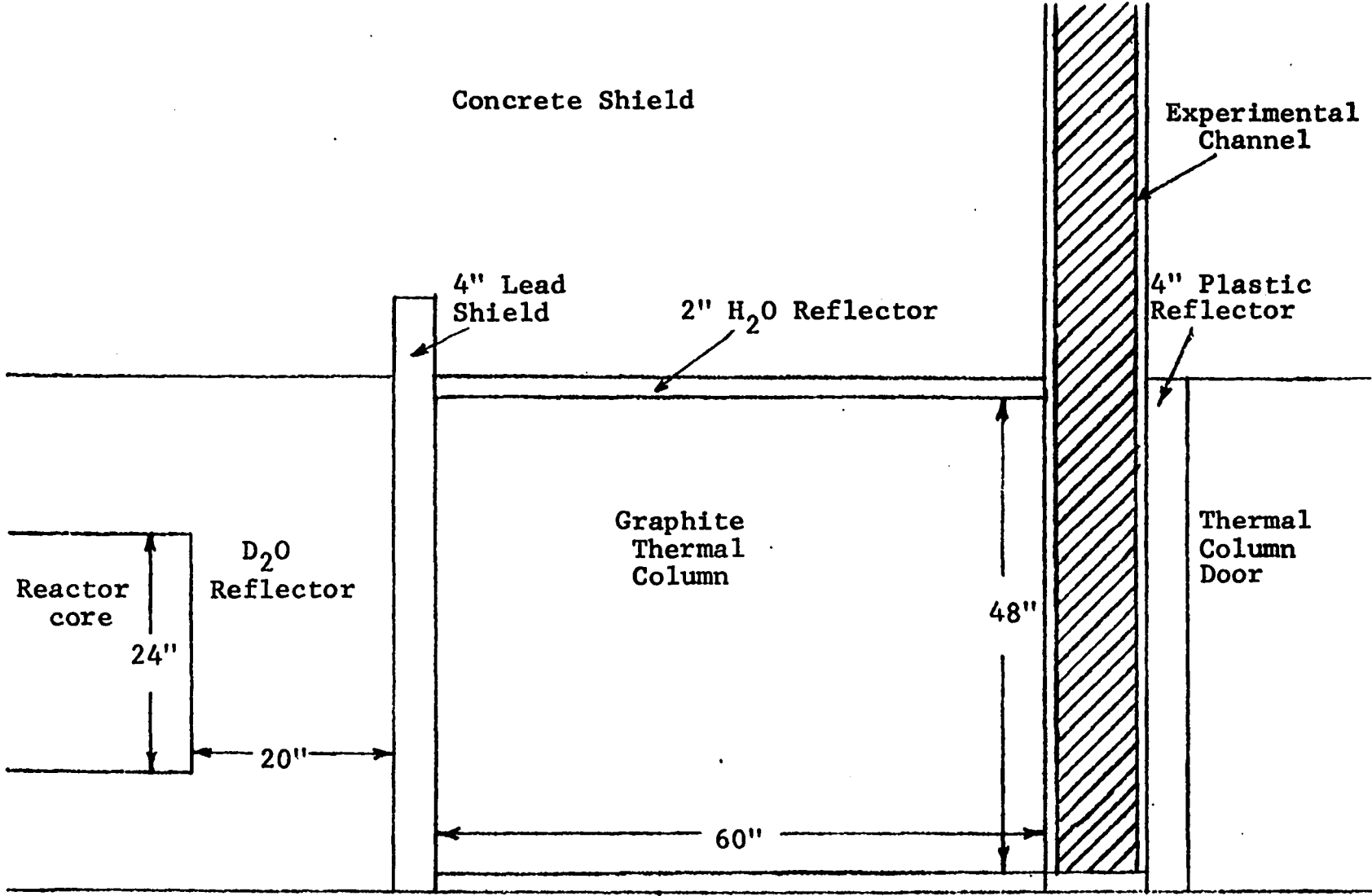


Figure 5. The position of the experimental channel in the ALRR reactor

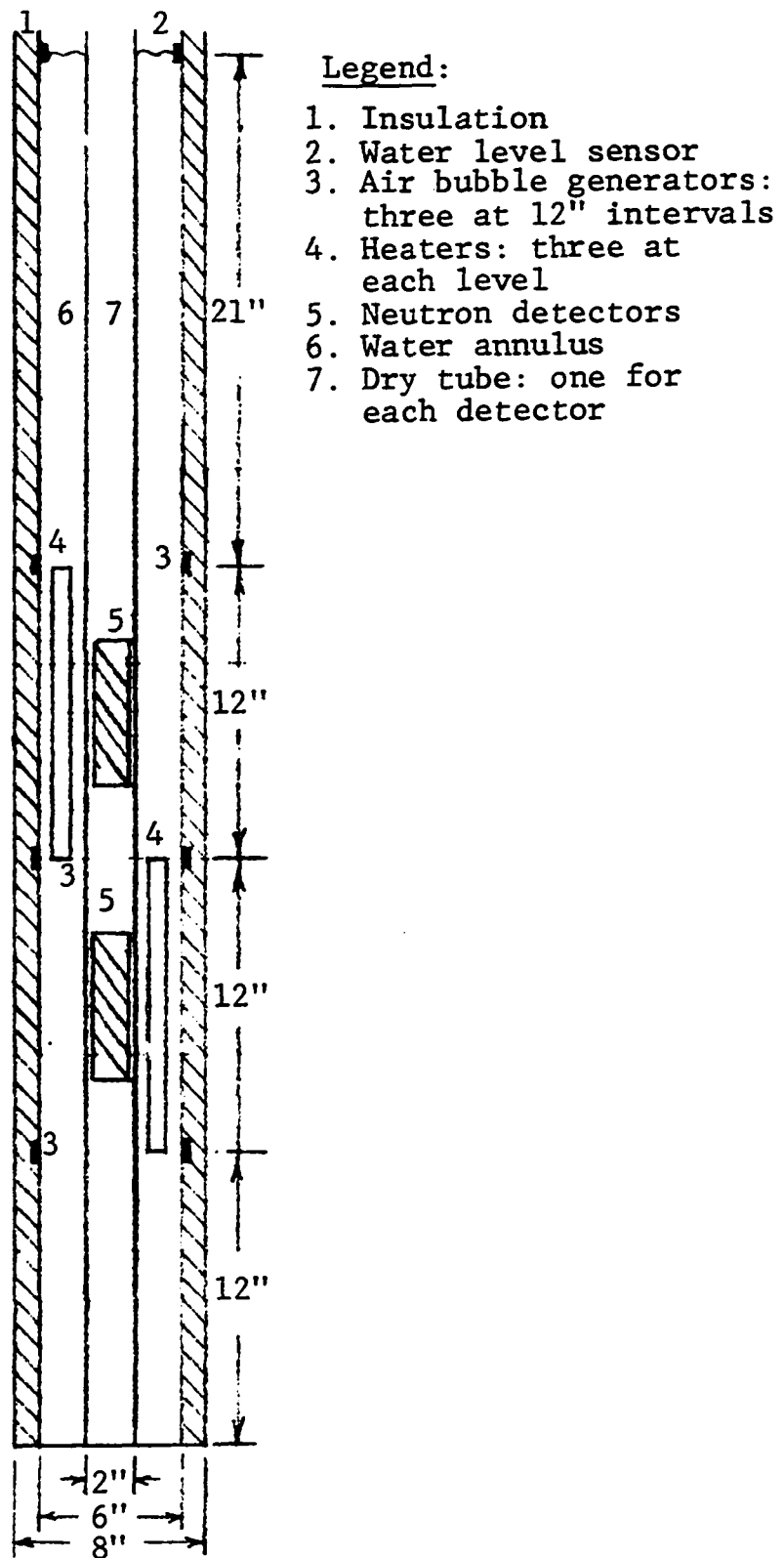


Figure 6. Schematic diagram of the boiling channel

Air bubbles can be introduced from three bubble generators separated 12 inches from each other, with each generator having four holes (#54 drill) 90° apart, with each set of holes rotated by 30° from the other two sets. The air flow rate to each bubble generator can be controlled by a flow meter, a pressure sensor, and a pressure regulator. There is provision to pulse the air flow rate to any of the bubble generators with a solenoid valve operable at a constant open-close rate. Steam voids can be introduced at two levels with a set of three 12 inch high electrical heaters at each level. The heaters in each set are 120° apart from each other, and are rotated by 60° with respect to the other set. The electrical power to each heater can be controlled by individual variacs with a minimum of 1000 W to each heater.

The level of water in the channel can be monitored by sensors placed at two levels to ensure safety and constant experimental conditions.

The temperature along the channel can be monitored by thermocouples placed at five positions along the channel.

C. The Signal Processing System

The signal processing system is shown in Fig. 7. The fission chamber current signals are fed to two pre-amplifiers which convert the signals to voltage and amplify them. The outputs of the pre-amplifiers are taken to filtering stages where the D.C. voltage is removed and the fluctuations in the signals are amplified and filtered for anti-aliasing purposes. The conditioned signals are then multiplexed into an analog to digital converter, and the information from each channel is stored in a buffer memory. The information in the buffer memories is then transmitted to the on-line PDP-15 computer at ALRR for further conditioning, application of fast Fourier transform (FFT) routine, and calculation of spectral densities. The computation is controlled by a teletype on-line with the PDP-15 computer.

D. System for Equipment Transfer Function Measurement

To measure the transfer function of the signal conditioning equipment a set-up as shown in Figure 8 is used.

As shown in the figure, the output of one channel serves as the input to the second channel. In this manner an input-output transfer function for the anti-aliasing

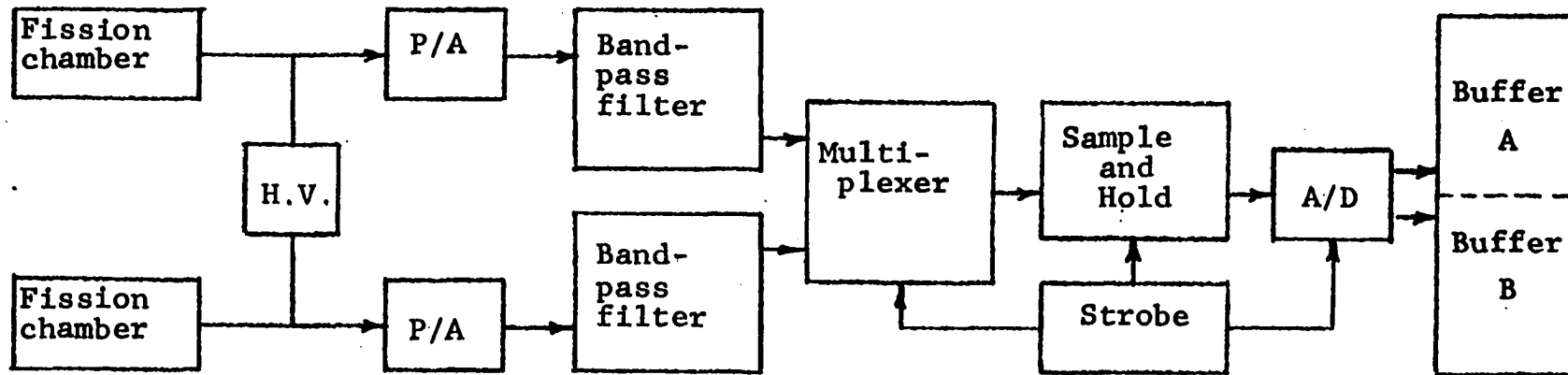


Figure 7. Signal processing system

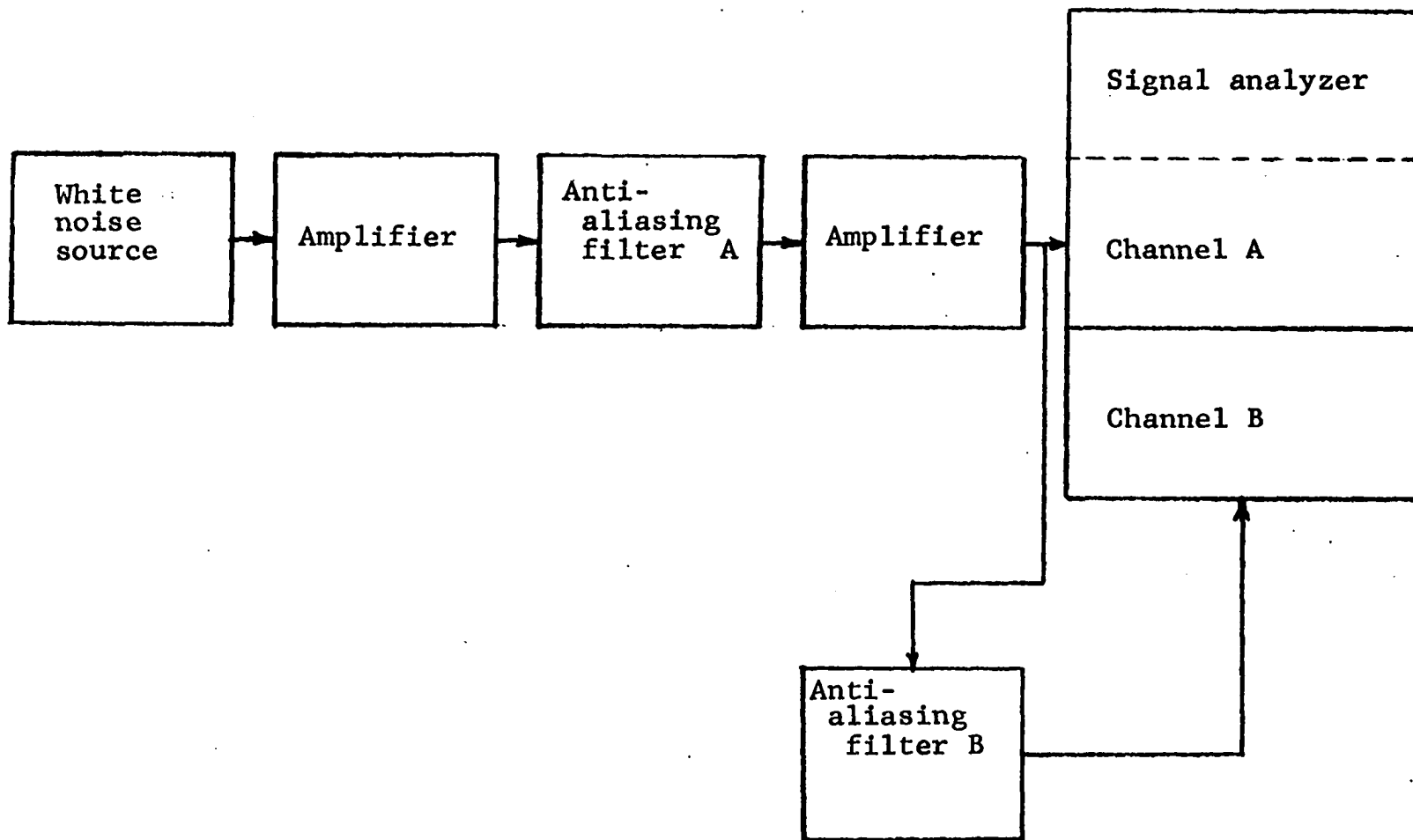


Figure 8. Block diagram of the system for transfer function measurement

filter can be measured.

This measurement is necessary to ensure that the break frequency, roll off rate, and phase lag properties of the filters agree with those specified by the manufacturer.

V. EXPERIMENTAL PROCEDURES

A. Modes of Operation

The experimental equipment was operated in four distinct modes as described below.

The first mode of operation involved checking of electronic equipment and computer routines by feeding known signals to the system. Single frequency signals from a signal generator were used to check the frequency response of the entire system. White noise signals were used to confirm the properties of the anti-aliasing filters by using the system of Fig. 8.

In the second mode of operation the neutron detector signals were analyzed without any artificially introduced perturbations. The purpose of this mode of operation was to find out the spectral properties of the reactor system in the absence of any perturbations.

In the third mode of operation, perturbations were introduced into the test channel in the form of air bubbles. Measurements were carried out with the detectors side by side or a few inches apart. The purpose of this mode of operation was to learn how well air bubbles can be used to simulate boiling, to what extent air bubbles affect the neutron spectra, and if air bubble speed can be deduced from phase measurements of the signals of two axially separated

detectors.

Boiling with electrical heaters was introduced in the test channel in the fourth mode of operation. Boiling was done by either a single or a set of three heaters, with the rest of the heaters used to keep the water at the boiling temperature. Spectrum and phase measurements were repeated for this case.

B. Signal Conditioning

The output of the fission chambers are in the form of D.C. currents with small fluctuations added to them. The current signals were converted to voltage signals by preamplifiers. Before any further amplification of the signals the D.C. components were removed by either high pass filtering or application of an adjustable bias voltage. The fluctuating signals were then amplified and passed through low pass anti-aliasing filters. The signals were, at this point, ready for digitization. The sample rate of the analog to digital converter is dictated by the cut-off frequency of the anti-aliasing filters. During preliminary tests it was found that a cut off frequency of 10 Hz could be used for the anti-aliasing filters as the measured spectra decayed to noise background below 10 Hz. A digitization rate of 25.6 samples per second was chosen accordingly to satisfy the Nyquist criterion [2, 20].

To ensure that uninterrupted data strings were collected, two buffer memories of 1024 (2^{10}) word capacity each were employed with each word having a range of ± 2048 (2^{12}) which yields a dynamic range of about 80 dB [2].

After the buffers were filled the information was transmitted to the ALRR on-line PDP-15 computer for the application of the FFT routine.

C. Calculation of Spectra

To arrive at desired spectral functions a fast Fourier transform routine is applied to the time series data stored in the memory buffers. The details of data conditioning before and after application of the FFT algorithm are covered extensively in textbooks by Bendat and Piersol [2], and Otnes and Enochson [20]. The complete algorithm used in the present work is outlined in Appendix E.

VI. EXPERIMENTAL RESULTS

A. Flux Measurements

Neutron flux measurements were carried out inside the experimental channel before the detectors were inserted into the channel. The results of these measurements were needed to find out how thermalized the neutron flux at the position of the detectors is, and if the thermal flux is high enough for the fission chambers to be operated in the current mode. It was also desired to know the shape of flux along the length of the channel.

The method of gold foil irradiation was used with bare and cadmium covered foils. The results of thermal neutron flux measurements are given in Table 1 at 6" intervals along the length of the channel measured from the bottom of the channel. These flux values are high enough to allow operation of the fission chambers in current mode. A cadmium ratio of approximately 2300 was calculated which indicates that the neutron flux inside the experimental channel is extremely thermalized. The measurements were carried out at the usual ALRR operating power of 5 MW.

Thus, due to highly thermalized nature of the neutron flux at the position of the experimental channel no thermalization effect due to variations of void fraction in the channel can be expected. Any observable spectral

Table 1. Results of neutron flux measurements inside the experimental channel

Position of the gold foils (inches from the bottom of the channel)	Thermal neutron flux (n/cm ² -sec)
6	8.614×10^8
12	1.305×10^9
18	1.767×10^9
24	2.153×10^9
30	2.167×10^9
36	2.159×10^9
42	1.579×10^9
48	8.246×10^8
54	3.557×10^8
60	1.622×10^8

characteristics should be primarily due to variations in the absorption and scattering cross sections in the channel caused by fluctuations in void fraction.

From the measured neutron flux values and known reactor power and fission chamber properties an approximate upper limit estimate of detector efficiency can be made. The detector efficiency in terms of detections per fission in the reactor can be written as

$$W \sim \frac{N\sigma_f\phi}{\text{fission rate in the reactor}},$$

where N is the number of U-235 atoms in the chamber, σ_f is the microscopic fission cross section of U-235, and ϕ is the thermal neutron flux at the position of the chamber. An approximate upper limit for detector efficiency is thus found to be $W \approx 10^{-8}$ detections/fission.

This is a very low value for detector efficiency which, when used in Eq. 5 along with an estimated fission rate of $F = 1.6 \times 10^{17}$ and estimated prompt neutron lifetime of $\ell = 5 \times 10^{-4}$, indicates that the second term in Eq. 5 is larger than the other two terms by many orders of magnitude.

Thus the assumption of an at-power reactor is quite valid and Eq. 7 should describe the global APSD term.

B. System Checks

1. Single frequency signals

To confirm the frequency resolution and the dynamic range of the signal analysis system a series of measurements were made with single frequency sine waves of known frequency and amplitude as inputs.

The APSD plot for a set of input frequencies from 1 to 10 Hz, in 1 Hz steps, is given in Fig. 9. All the expected peaks are seen to fall at the expected frequencies. It can also be seen from the plot that a dynamic range (or

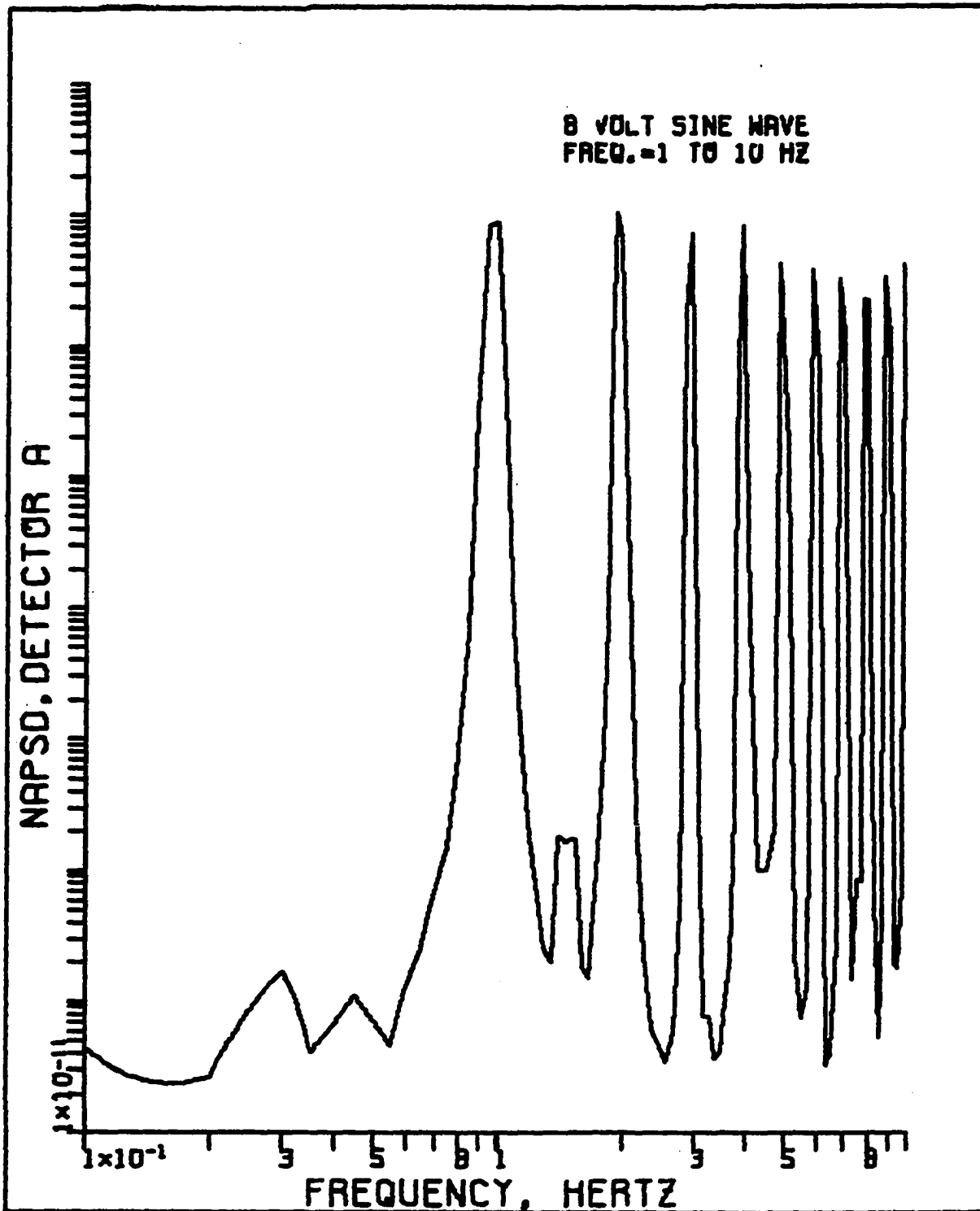


Figure 9. APSD plot for a set of input frequencies from 1 to 10 Hz, in 1 Hz steps.

signal to noise ratio) of better than 4 decades is realized, which agrees with the design value for dynamic range of 80 dB.

2. White noise signals

To confirm the properties of the anti-aliasing filters, and further check the signal analysis system a series of measurements were made with wide-band white noise signals as inputs.

The APSD plot for wide-band white noise as input signal and anti-aliasing filter set at 10 Hz is given in Fig. 10. The spectrum can be seen to be flat as is expected for white noise with some roll-off at the higher frequency end caused by the filter.

The system of Fig. 8 was used to measure the transfer function of the anti-aliasing filters. With white noise as input signal, cut-off frequency of filter A set at 10 Hz, and cut-off frequency of filter B set at 1 Hz the transfer function of filter B is measured as shown in Fig. 11. It is seen from the plot that the transfer function is flat below the break frequency at 1 Hz and rolls off at the expected rate of 24 dB per octave (or 80 dB per decade) beyond the break frequency.

The phase of the filter transfer function is shown in Fig. 9 along with manufacturers specification. The measured

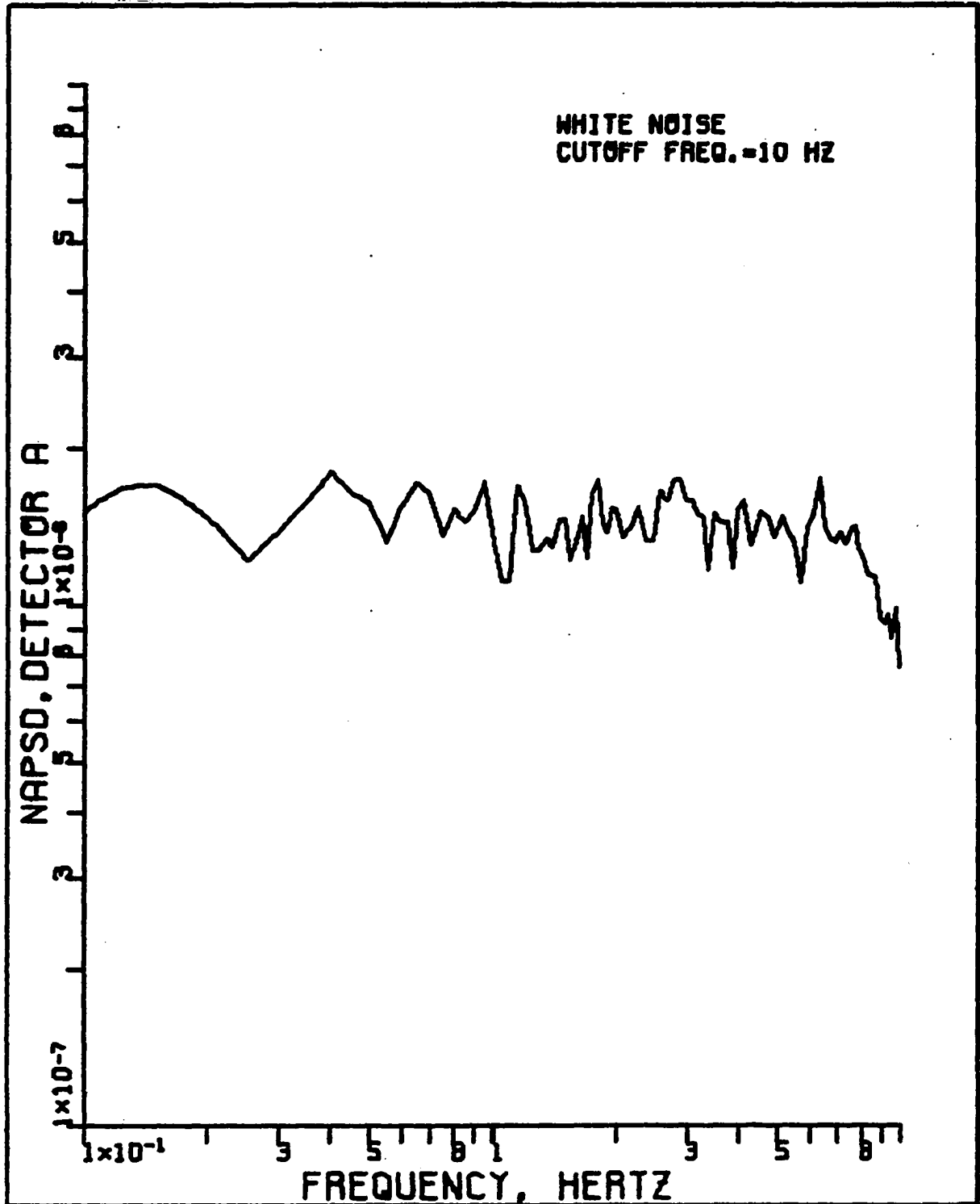


Figure 10. APSD plot for wide-band white noise as input signal and anti-aliasing filter set at 10 Hz

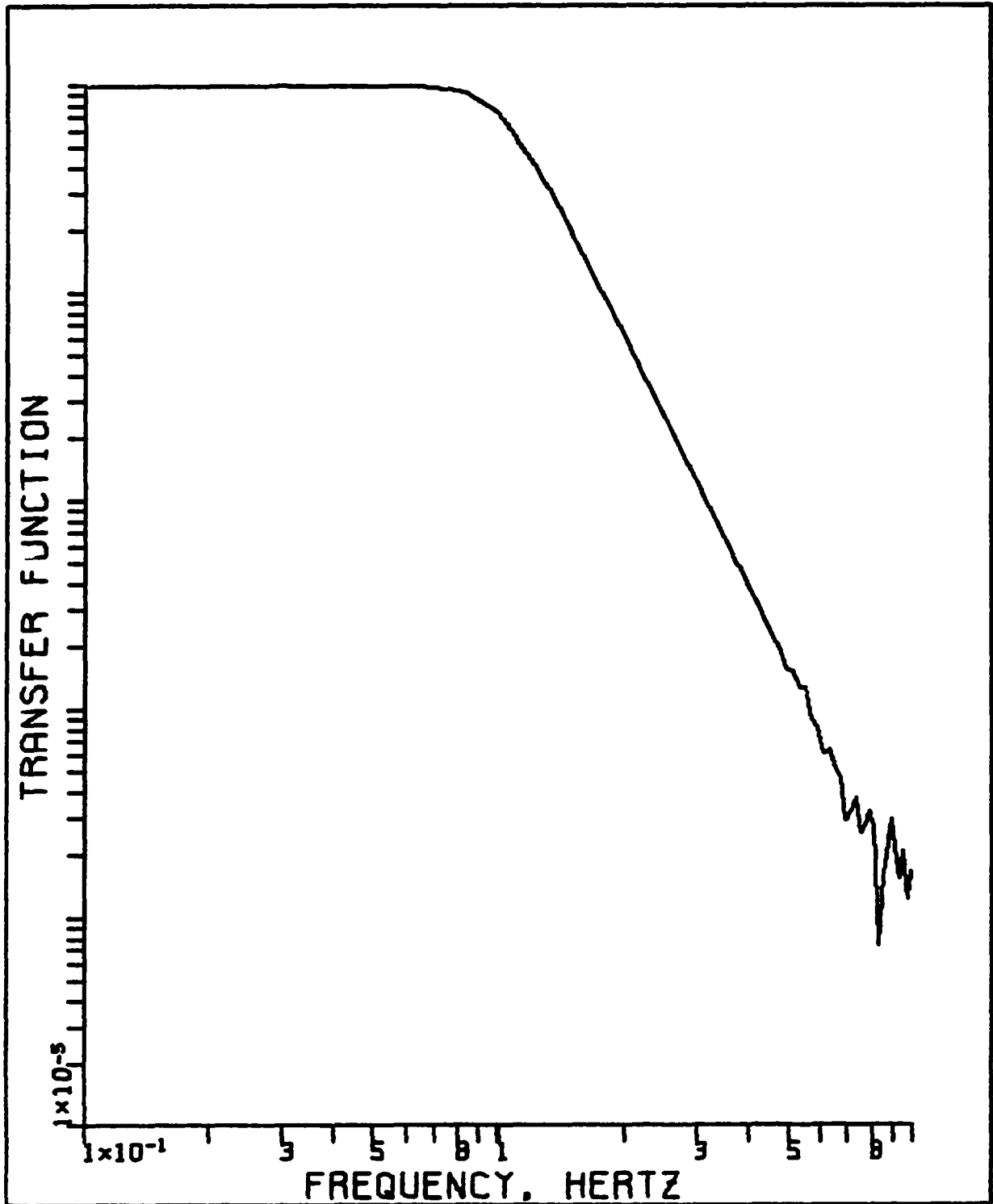


Figure 11. Magnitude of the transfer function of the anti-aliasing filter B with cut-off frequency set at 1 Hz

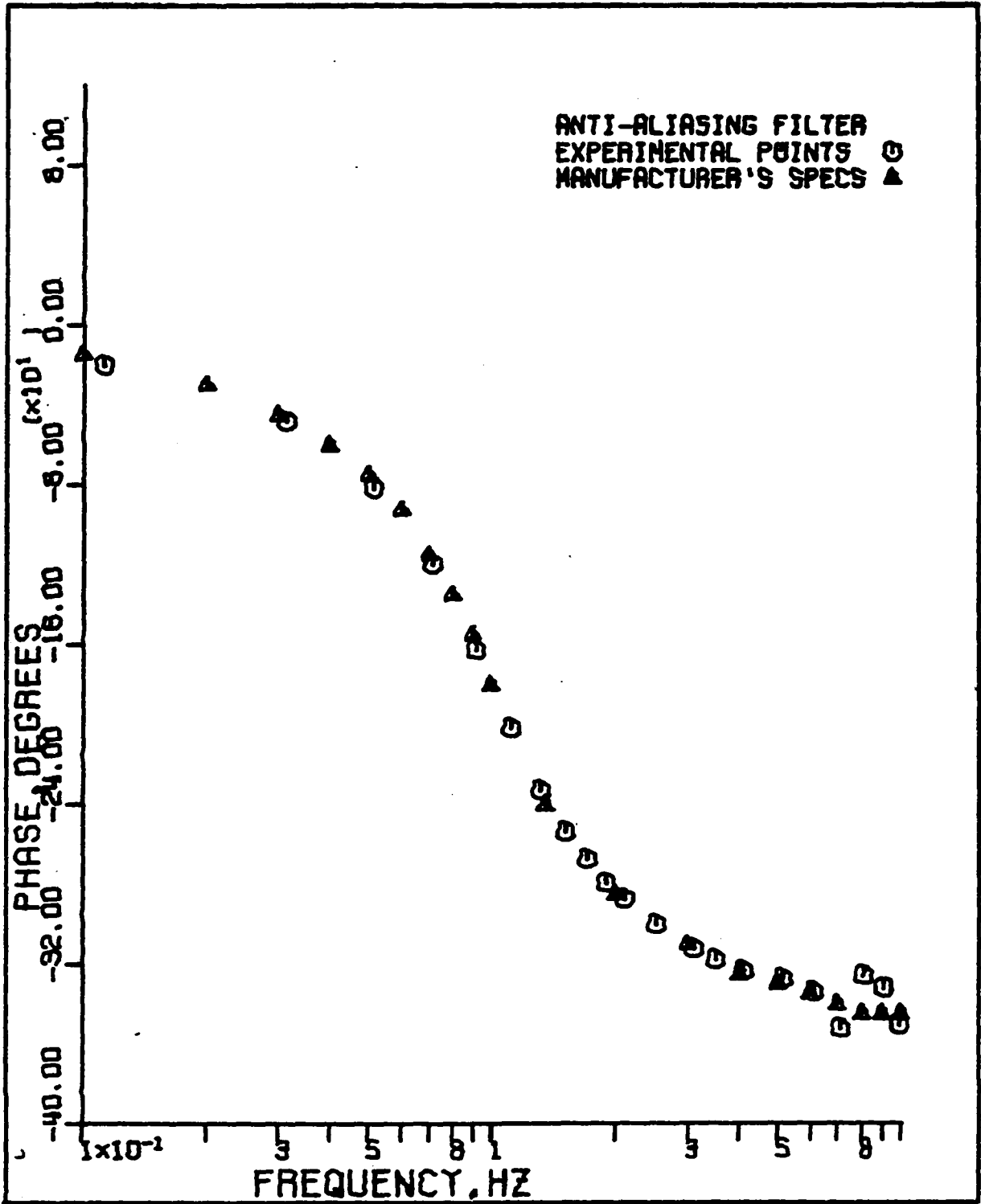


Figure 12. Comparison of measured phase of anti-aliasing filter with manufacturer's specifications

phase values agree with the manufacturers specifications within $\pm 5^\circ$ over most of the frequency range. At the higher frequency end the agreement is within $\pm 20^\circ$ because of loss of information due to filtering.

C. Neutron Noise Measurements in Absence of any Artificially Introduced Perturbation

A series of neutron noise measurements were made without any artificially introduced perturbation in order to study the characteristics of the reactor noise at the position of the experimental channel. The results of these measurements were essential in understanding of results when perturbations were introduced in the channel.

1. Test of stationarity of reactor noise signals

The stationarity of noise signals is a necessary condition for the applicability of the noise analysis methods being used. To establish the stationarity of the time series data the method of mean square value measurement was used.

Specifically, normalized mean square value (NMSV) of the noise signals were calculated by integrating normalized auto-power spectral density (NAPSD) measured over a period of time.

The results of NMSV measurements for the unperturbed case is shown in Fig. 13. Since all NMSV points fall within

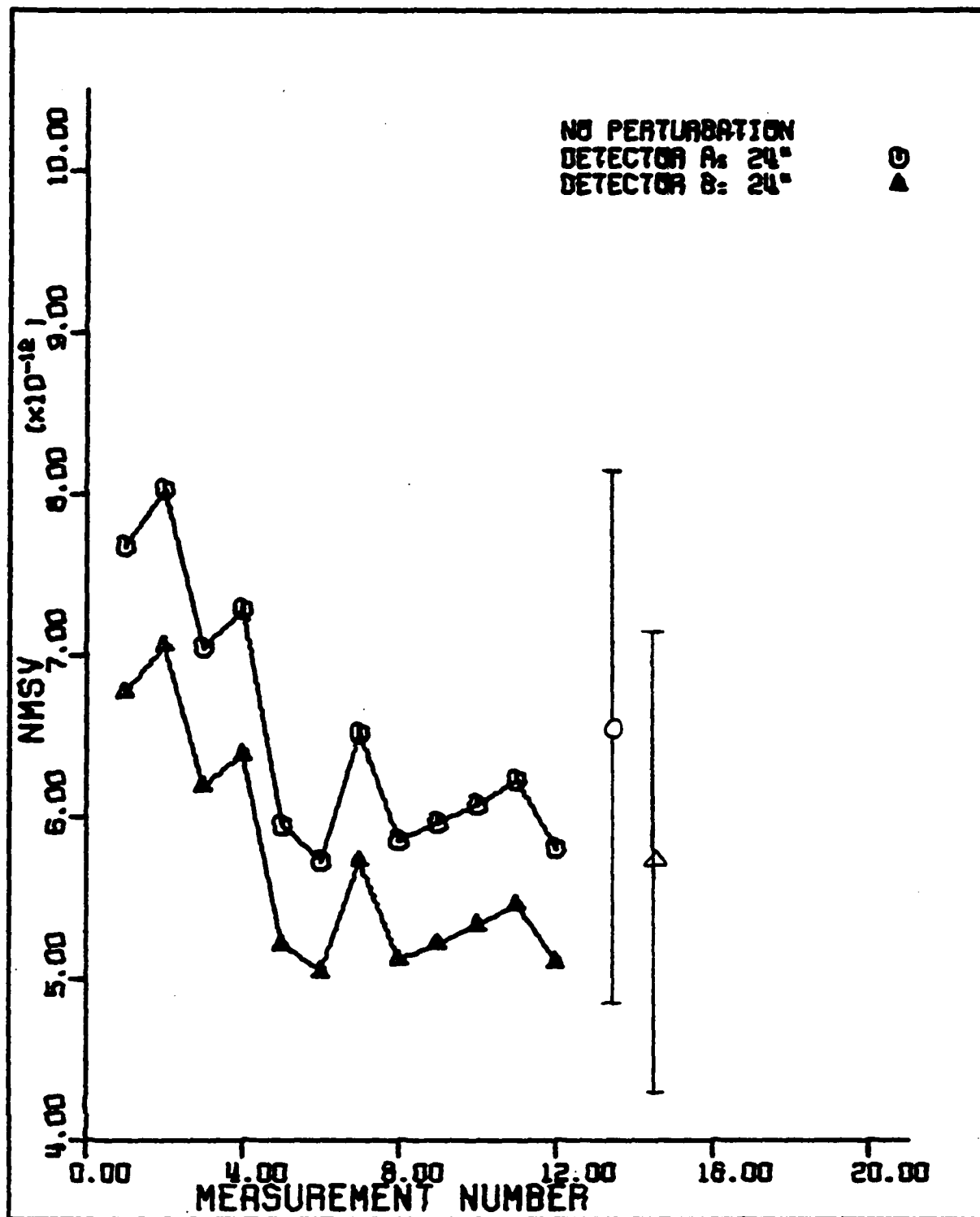


Figure 13. Test of stationarity of neutron noise signals in the unperturbed case

two standard deviation from the median NMSV the noise data can be assumed to be stationary in the wide sense.

2. Reactor noise spectra

Reactor noise spectra in absence of any artificially induced perturbations are presented in Figures 14 through 19. For these spectra the detectors were placed side by side at 24 inches from the bottom of channel (mid-elevation).

The NAPSD's of detectors A and B given in Figures 14 and 15 are seen to be very similar to each other. This similarity is expected since both detectors observe the same reactor noise. The APSD's show a roll-off of approximately 40 dB per decade, which flattens out at the higher frequency end as the spectra decay into the detection noise background. The peak at ~ 8.8 Hz is probably due to aliasing. The aliased frequency which has caused this peak can be found [2] from the relation

$$f_e = 4f_c + f .$$

For $f_c = 12.8$ and $f = 8.8$ the aliased frequency is calculated to be $f_e = 60$ Hz.

According to the results of Figs. 14 and 15 the global APSD given by Eq. 7 can be represented by a C/ω^2 function as a rough approximation.

The NCPSD plot given in Fig. 16 shows essentially the

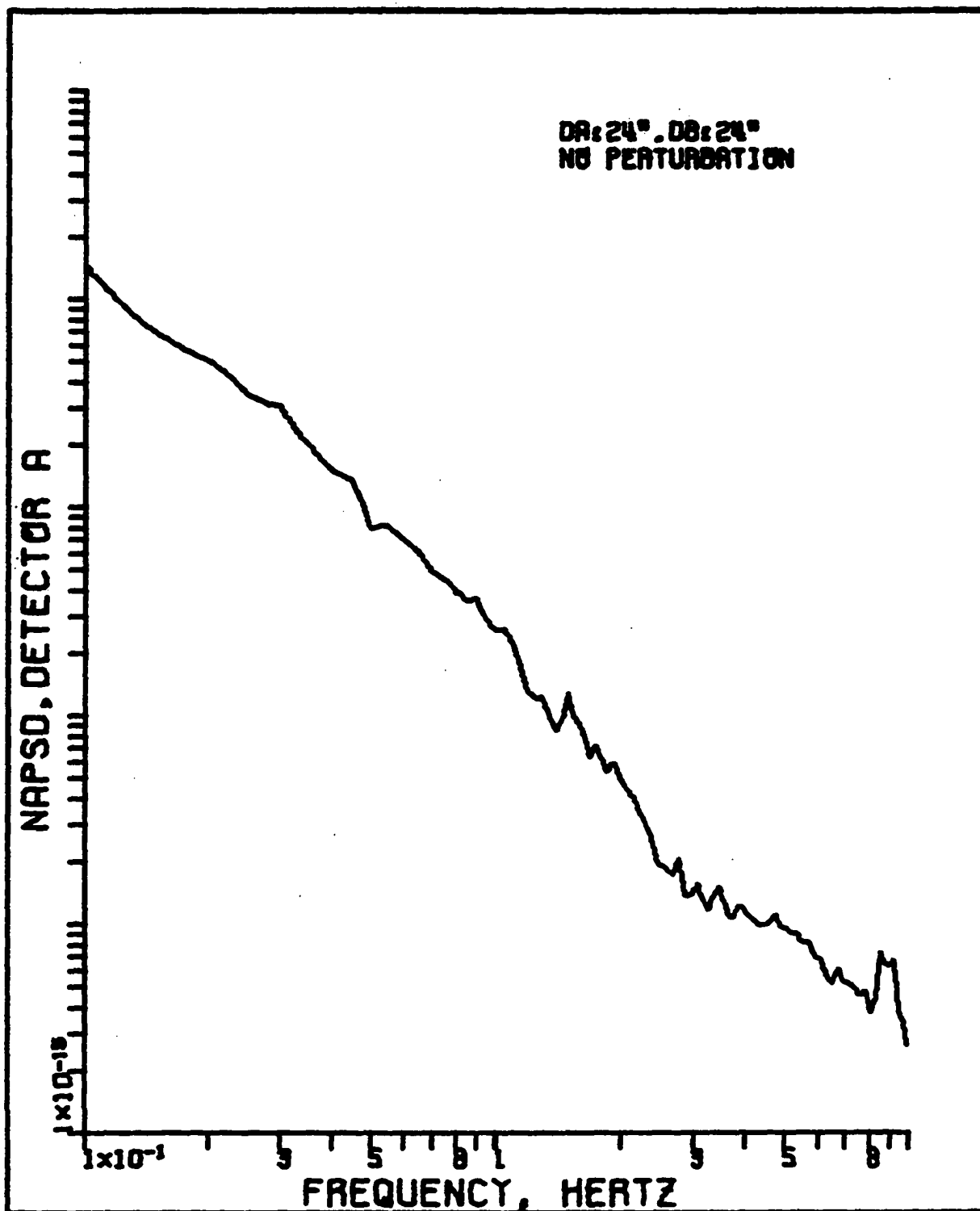


Figure 14. The NAPSD of the fluctuations in the signal of detector A in the unperturbed case

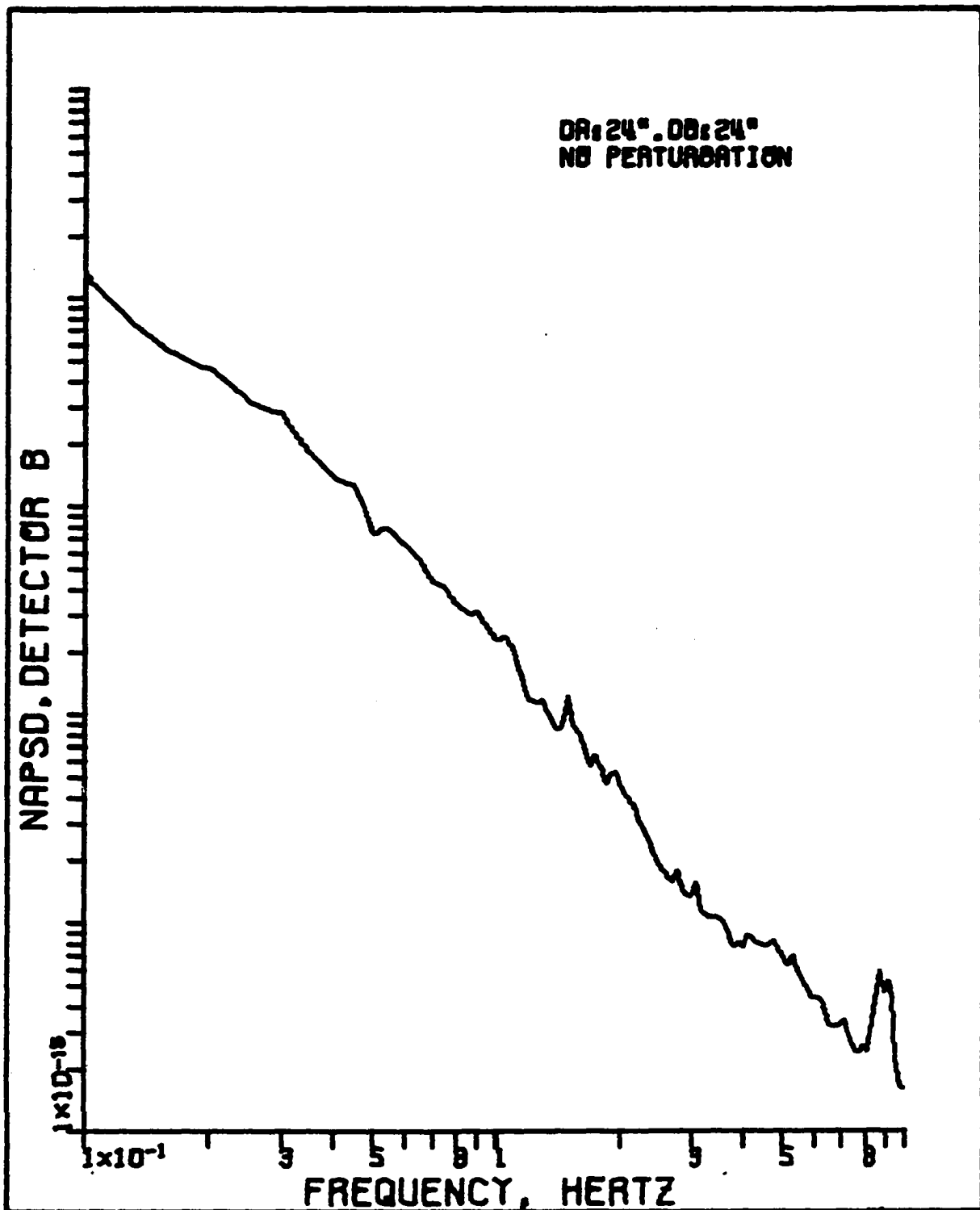


Figure 15. The NAPSD of the fluctuations in the signal of detector B in the unperturbed case

same behavior as the NAPSD plots with the exception that the aliased peak is more pronounced as should be expected. The behavior of the NCPSD plot agrees with the prediction of Eq. 32 that in the absence of any perturbations the measured NCPSD function should yield the global NAPSD function of Eq. 7.

Figure 17 shows a plot of phase difference of the two detector signals as a function of frequency. The phase is seen to stay near zero at the low frequency end but shows strong fluctuations at high frequency end where the spectra have decayed to detection noise background.

Figures 18 and 19 give plots of the transfer function and the coherence function for this case. The coherence function is seen to stay near unity up to about 1 Hz, indicating strong correlation between the detected signals up to this frequency. The coherence function is seen to decrease beyond 1 Hz indicating decreasing correlation between detected signals as frequency increases. The aliased peak is specially pronounced in the coherence function plot indicating the special property of the coherence function which makes possible the detection of low-amplitude correlated signals.

Figure 20 shows a plot of the coherence function when the detectors are separated by 12 inches and in absence of

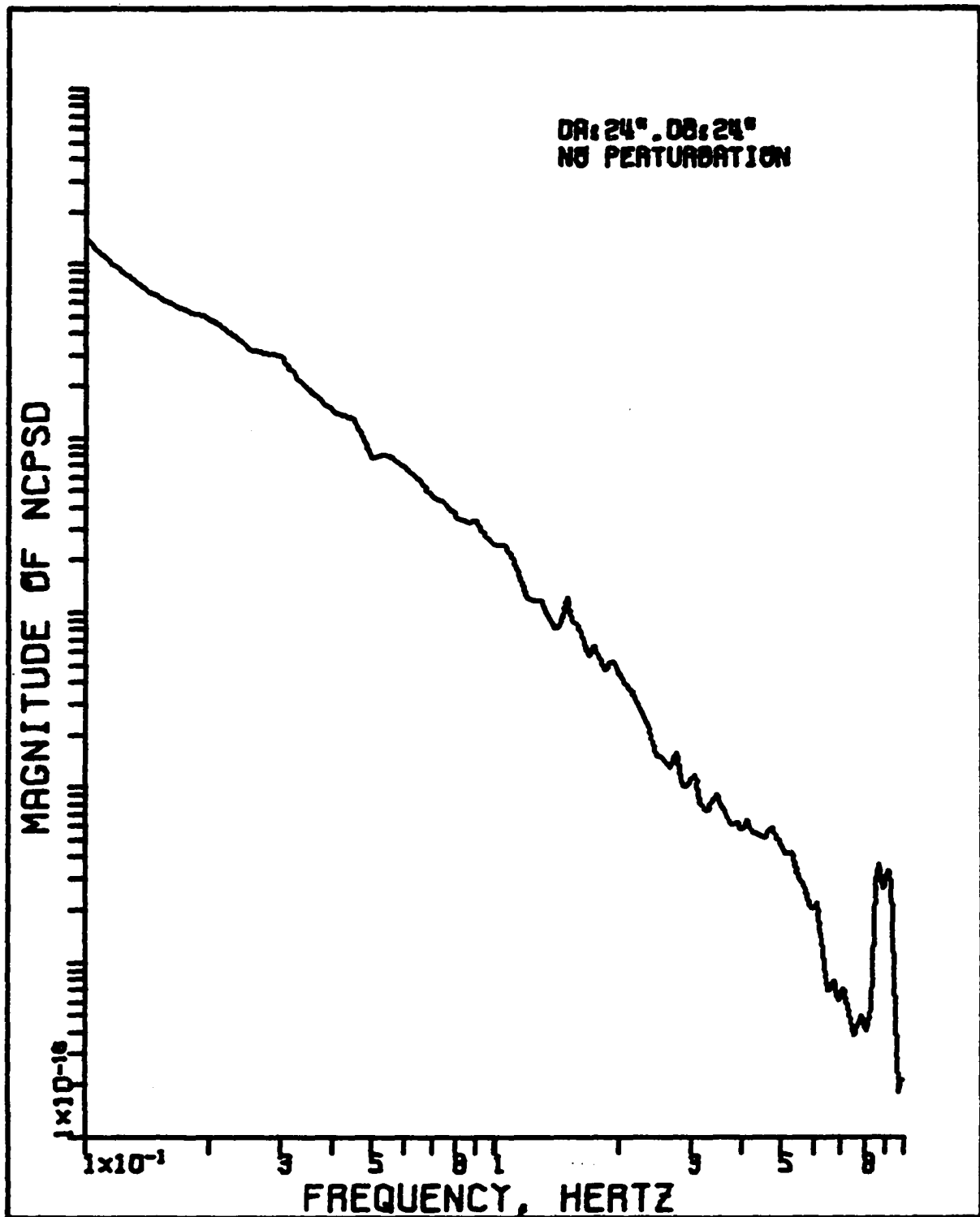


Figure 16. The NCPD of the fluctuations in the signals of detectors A and B in the unperturbed case

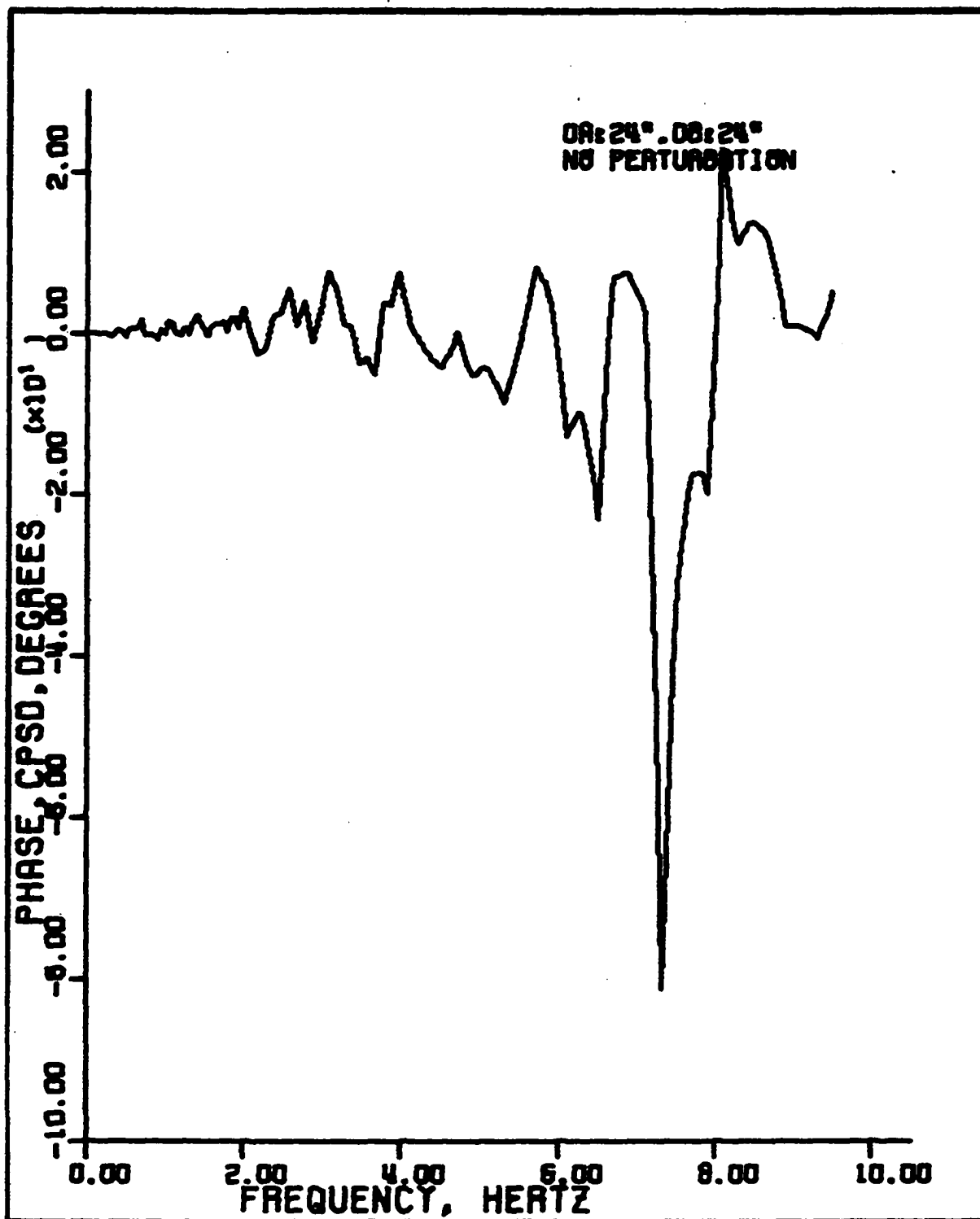


Figure 17. The phase difference of the detector signals in the unperturbed case

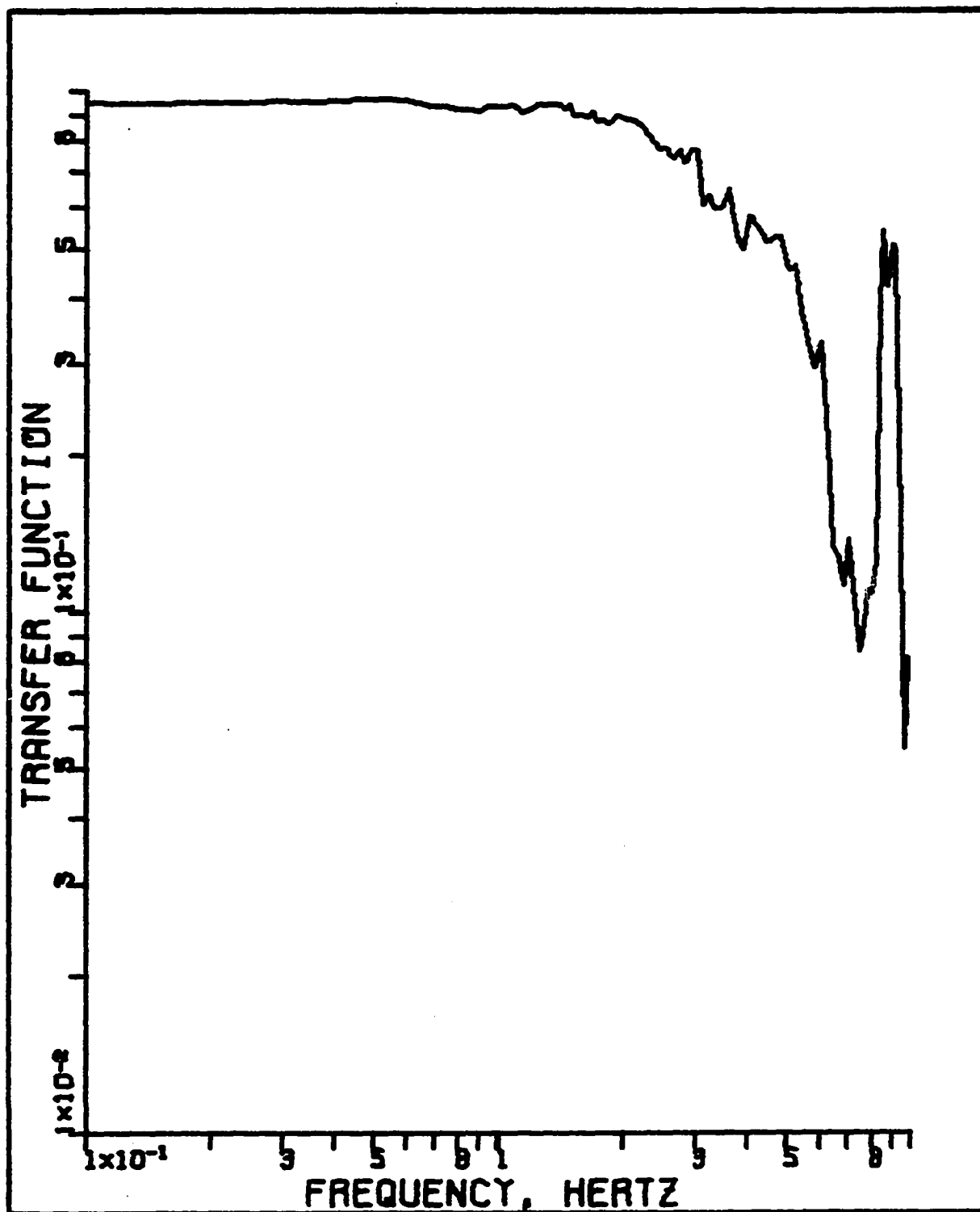


Figure 18. The transfer function in the unperturbed case

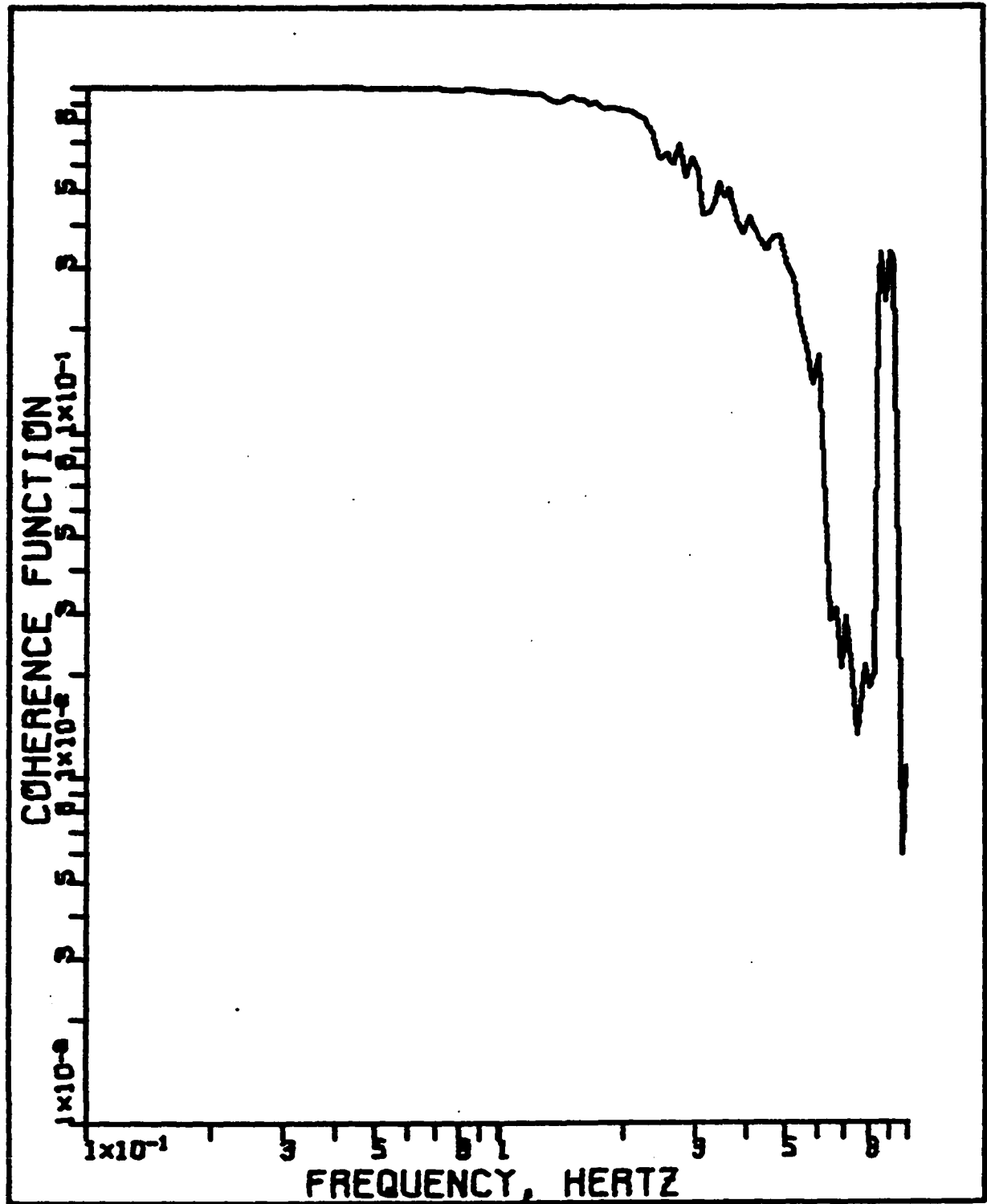


Figure 19. The coherence function in the unperturbed case with the detectors at the same level

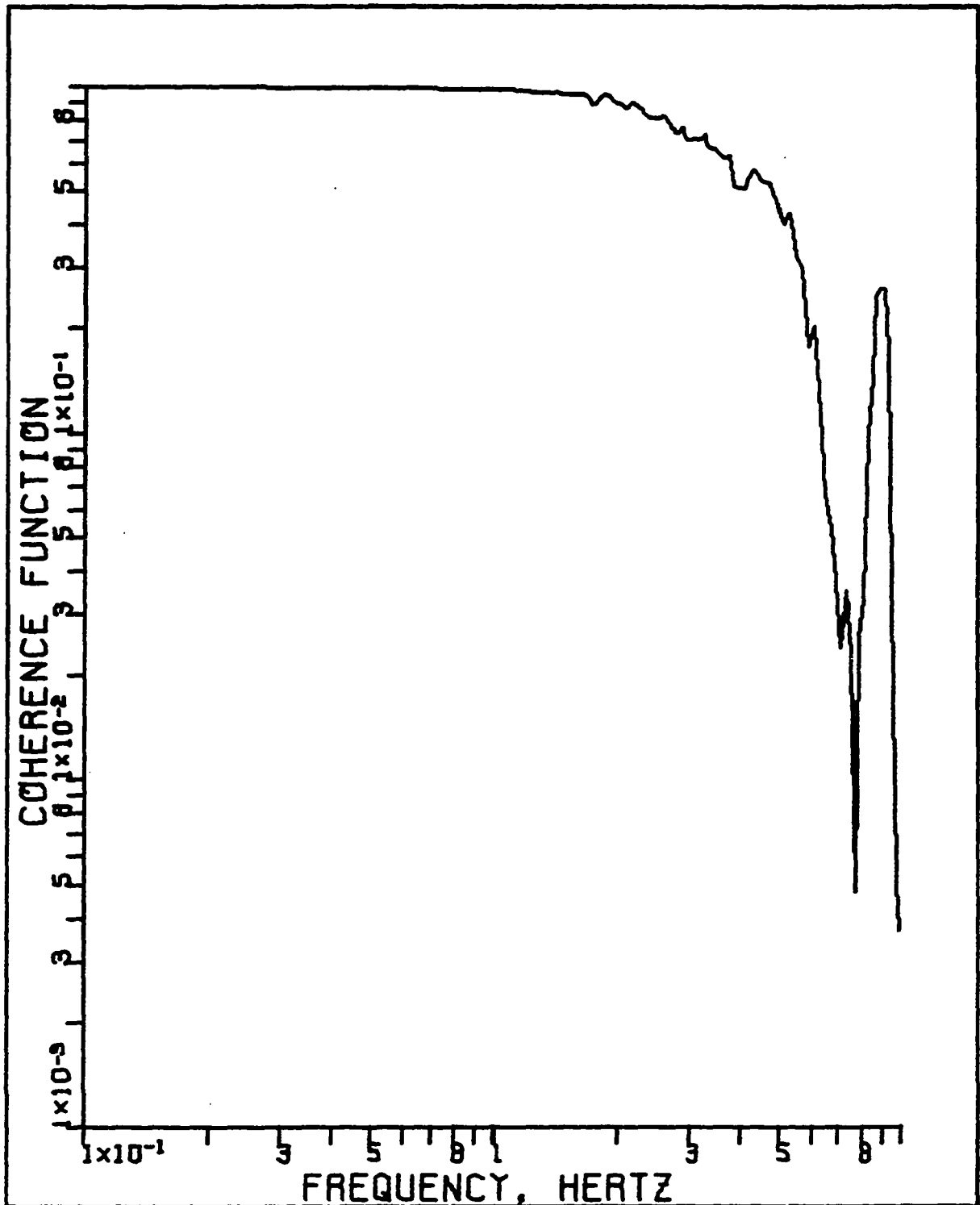


Figure 20. The coherence function in the unperturbed case with the detectors separated by 12 inches

any perturbations. It can be seen from the plot that high coherence value persists, indicating that the correlated signal is produced by the reactor and not by some local phenomena in the unperturbed channel.

To better understand the nature of reactor noise being observed here, it should be noted that the detector efficiency is very low ($W \approx 10^{-8}$) at the position of the experimental channel with respect to the reactor core. The near unity value of the coherence function being observed here implies very high detector efficiency if the reactor noise is assumed to be caused by the chain noise. From these observations it is concluded that the observed reactor noise is comprised mainly of power noise caused by reactivity fluctuations of the at-power reactor.

This result corroborates the same conclusion arrived at in Section VI.A, based on neutron flux measurement and fission rate in the reactor.

D. Measurements with Air Bubbles as the Source of Induced Perturbations

A large series of neutron noise measurements were carried out with air bubbles as the source of induced perturbation. Measurements were made with varying air flow rate and different positioning of the detectors with respect to each other. Measurements were also made with a pulsating air

column.

1. Test of stationarity of neutron noise signals

To establish the stationarity of the neutron noise signals in the presence of induced air bubble perturbations the method of NMSV measurement was used.

With detector A at 24 inches and detector B at 36 inches from the bottom of the channel, APSD measurements were performed with 0.0659 cubic feet per minute of constant air flow introduced at 12 inches from the bottom of the channel.

The results of NMSV calculations are shown in Figure 21. Since most of NMSV points fall within two standard deviations from the median NMSV the neutron noise data can be assumed to be stationary in the wide sense.

The NMSV points for detector B are larger than those for detector A due to the fact that detector B observes a larger void fraction as a result of bubble volume expansion along the channel. Parallel variation of NMSV's of the two detectors is probably caused by variations in reactor power which were not removed by normalization.

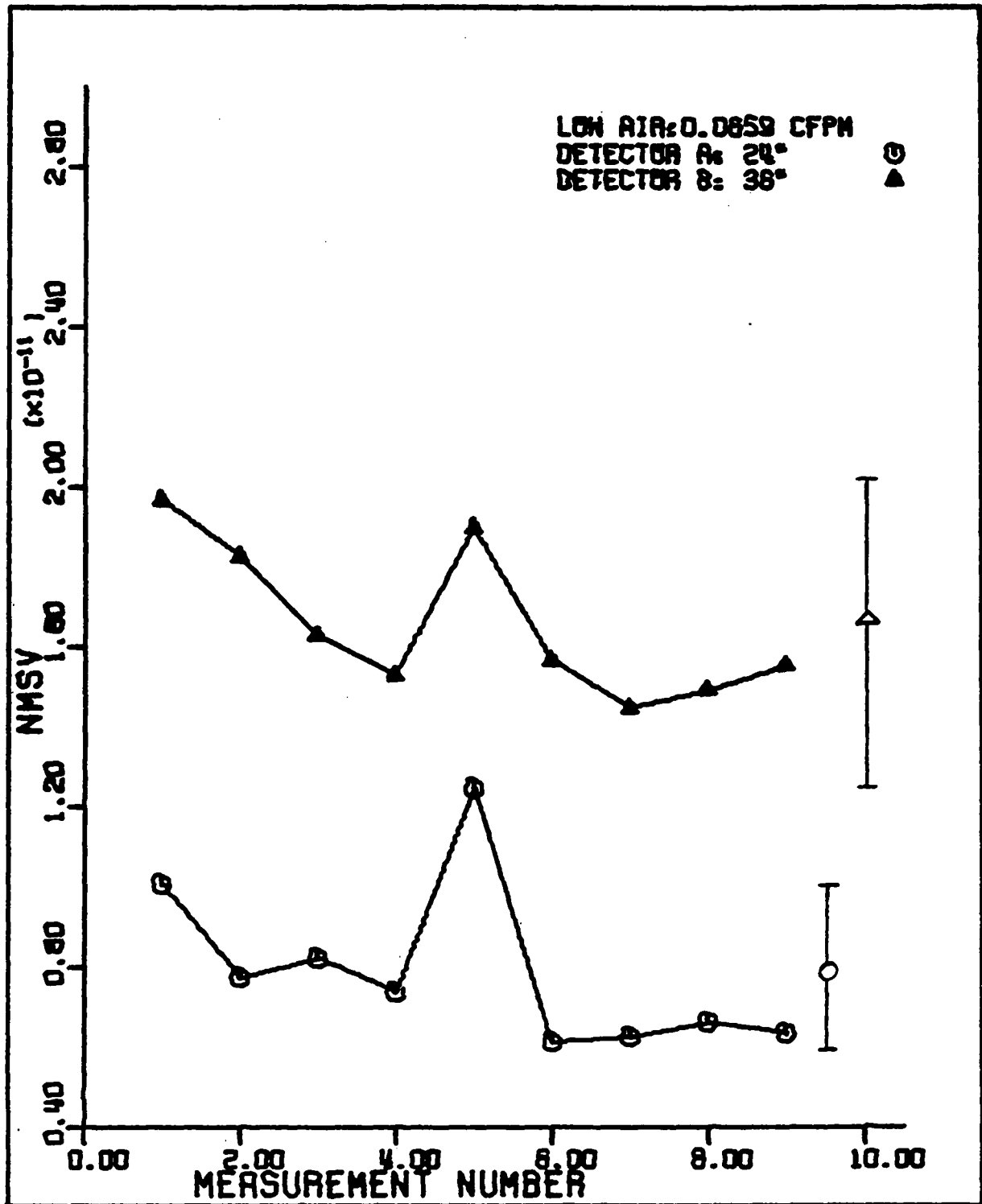


Figure 21. Test of stationarity of neutron noise signals in the presence of air bubbles

2. Effect of air flow rate on the neutron noise spectra

To study the effect of air flow rate on the observed neutron noise spectra a series of measurements were performed with changing air flow rates introduced into the channel.

With detector A at 24" and detector B at 30" a series of spectral measurements were done with zero to 0.34 cfpm of air introduced at the 12" inlet.

The results of these measurements are presented in Fig. 22 in the form of NMSV plots as a function of air flow rate. The NMSV vs. air flow rate curves show an exponential behavior, which agrees with the discussion of the limitations of Eq. 30.

Thus, the results of NMSV measurements indicate that mean bubble volume at any position in the channel increases with void flow rate due to coalescing of small bubbles into larger bubbles.

The NMSV's for detector B are larger than those for detector A due to bubble expansion along the channel.

To study the effect of varying air flow rates on NAPSD functions several NAPSD plots of detector A signals for air flow rates ranging from zero to 0.34 cfpm are given in Fig. 23.

An examination of the spectra shows that the NAPSD

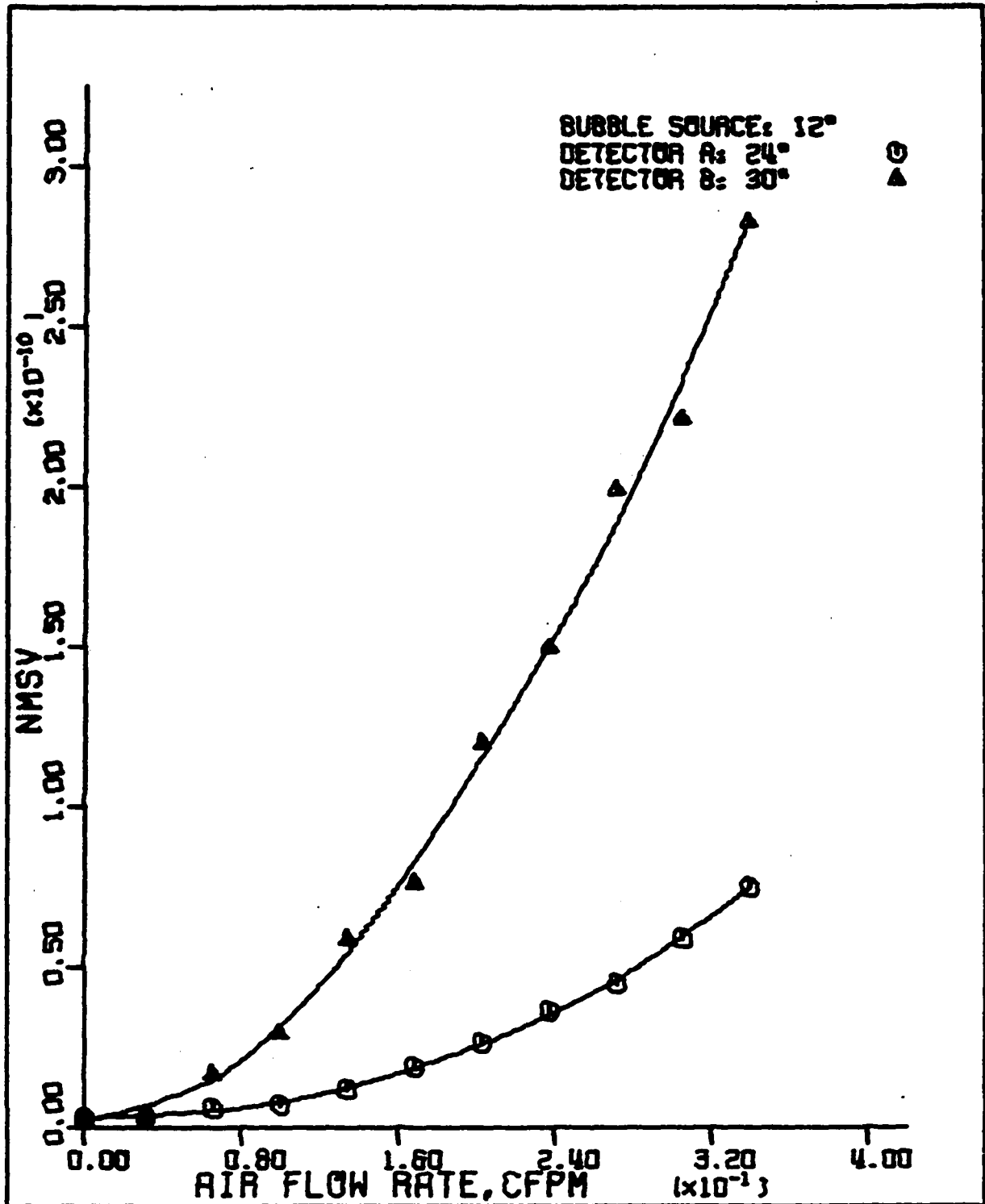


Figure 22. NMSV as a function of air flow rate

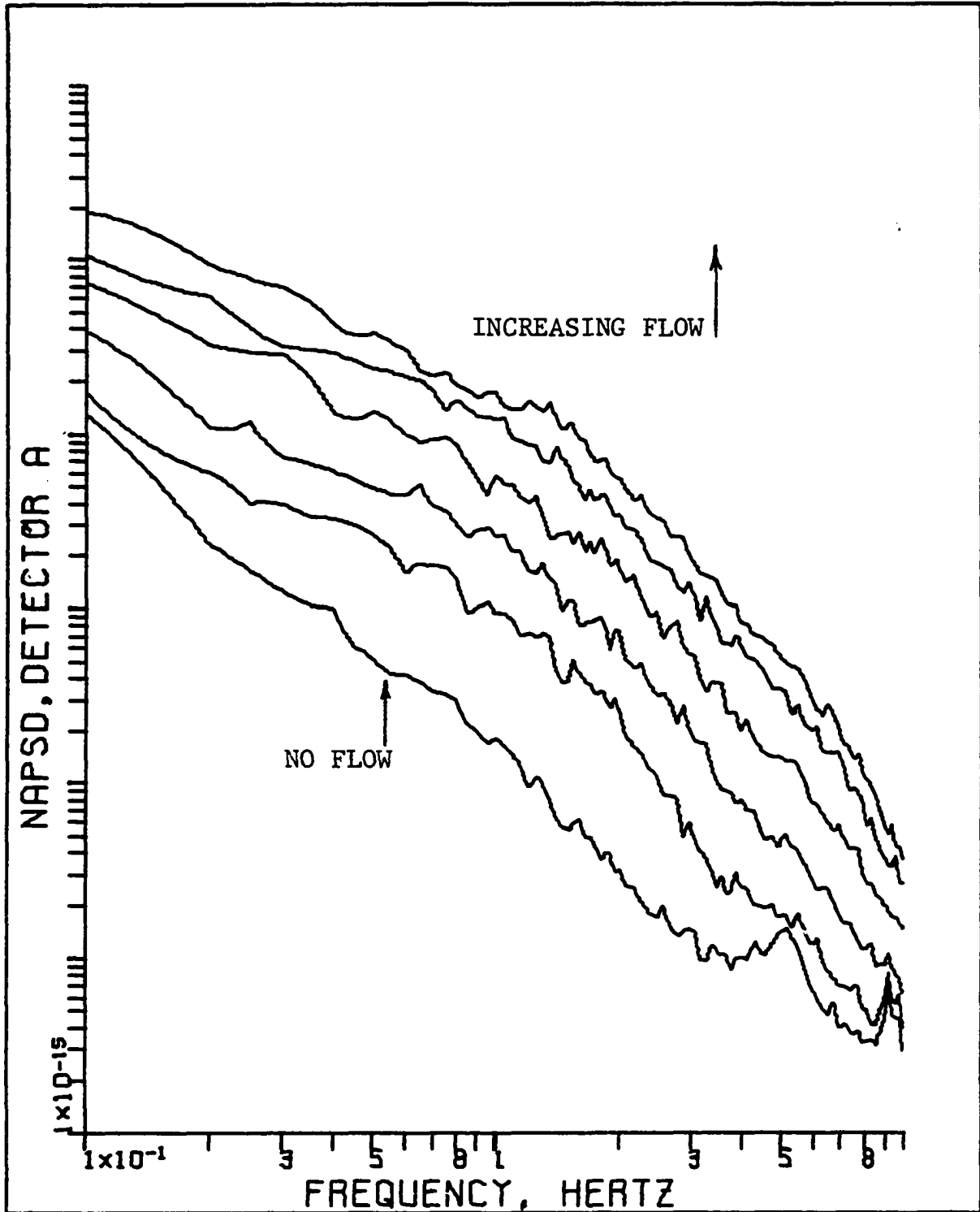


Figure 23. Multiple NAPSD plot showing the variation of NAPSD with air flow rate

for 0.34 cfpm of air is about an order of magnitude larger than the NAPSD for the unperturbed case at the two ends of the spectrum, while a difference of about two orders of magnitude exists at around 1 Hz.

Thus, contrary to the prediction of Eq. 9 the spectral density of void fraction fluctuations is found to be frequency dependent with fluctuations centered around a frequency of about 1 Hz. The source of this spectral characteristic may be fluctuations in the air column passing the detector due to bunching of bubbles [17].

To study the effect of local perturbations on the spectra more closely, the NAPSD for no air flow was subtracted from the NAPSD for 0.34 cfpm air flow with the result shown in Fig. 24.

The spectrum of Fig. 24 can be compared to the theoretical prediction of Eqs. 15, 16 and 17. Close examination of Fig. 24 shows that there is a change of slope of the NAPSD curve starting at around 1.5 Hz. However, this change of slope does not seem to be described by Eq. 16 which predicts a roll-off rate of 80 dB per decade. The observed slope is more like 60 dB per decade. The behavior of the spectrum below the apparent break frequency does not agree with the prediction of Eq. 15 that the spectrum should be frequency independent over the lower frequency range.

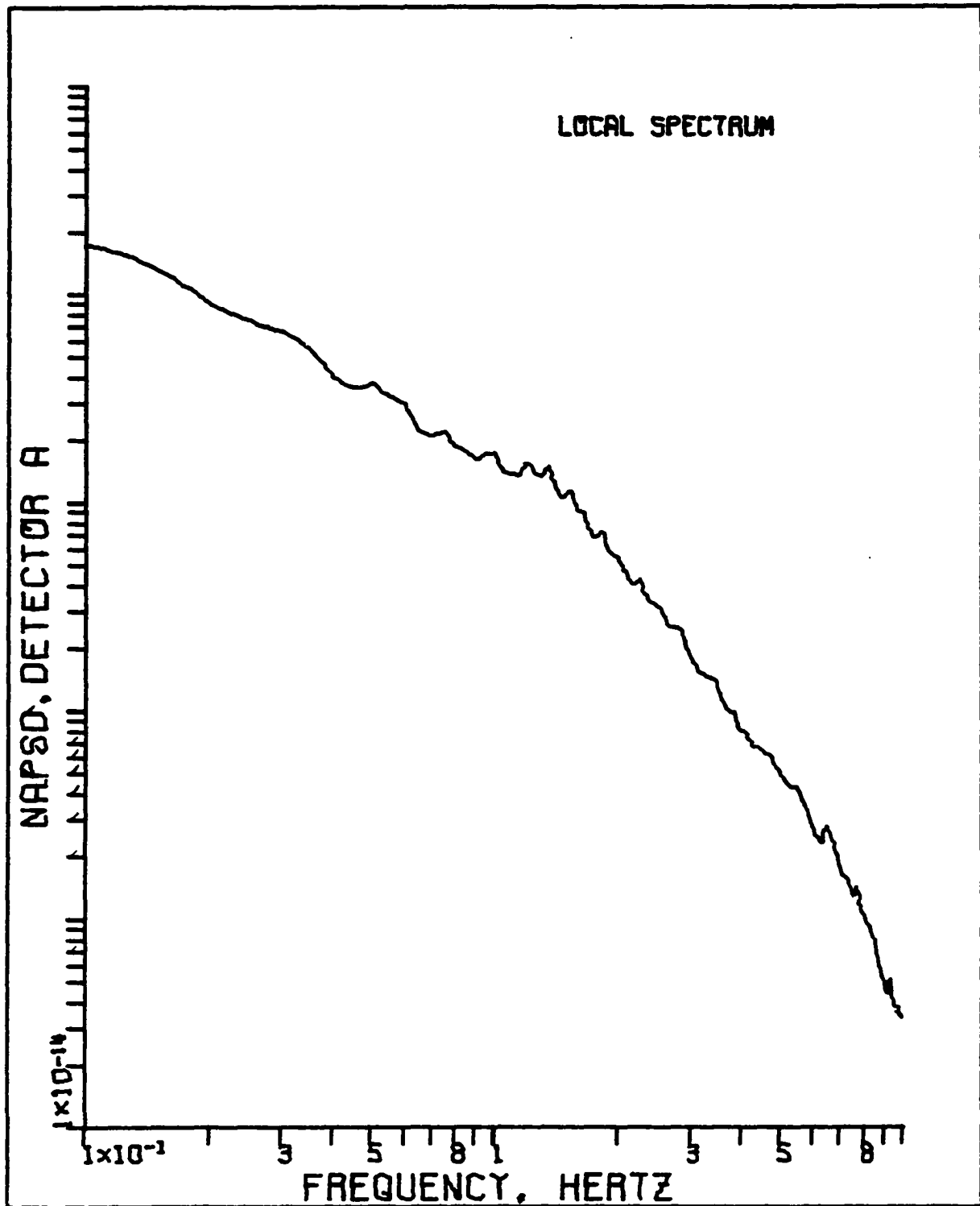


Figure 24. The local NAPSD for the case of 0.34 cfpm of air flow

The effect of finite detector size described by Eq. 17 and Figs. 2 and 3 cannot be seen in Fig. 24, as there are no easily identifiable null frequencies observable as predicted by theory.

The lack of success in observing the null frequencies of Eq. 17 may be due to smearing of spectral values over the resolution bandwidths defined in Table E-1.

3. Finite volume of sensitivity study

To study the theoretical prediction of Eq. 12 that the fluctuations in flux, and hence in detector current, are only sensitive to the fluctuations in void fraction near the point of observation, a series of spectral measurements were made with changing detector positions with respect to one of the air bubble generators.

More specifically, a constant air flow of 0.34 cfpm of air was introduced at the 24" air bubble generator and the detector positions were changed with respect to this air bubble generator.

NMSV's were calculated for each detector at each position and results are given in Fig. 25. To better understand the results it should be emphasized that the indicated detector positions are the position of the centerline of the detectors in the channel, and that each detector has approximately 6 inches of sensitive length.

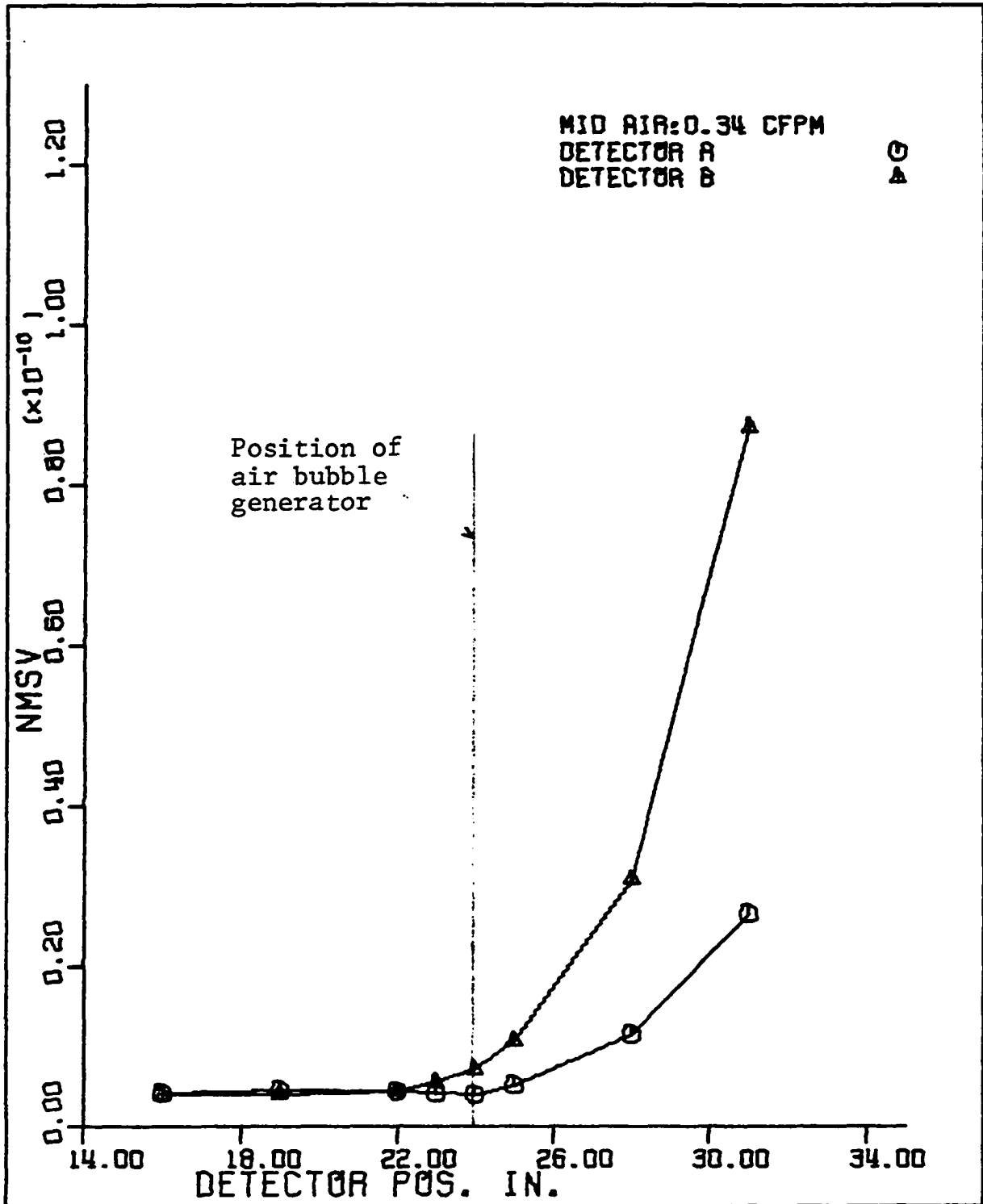


Figure 25. NMSV's of detector current fluctuations as a function of detector center-line position

It can be seen from Fig. 25 that the detectors are not affected by the void fluctuations until the sensitive portion of the detectors coincide with the bubble generator. Thus, the volume of sensitivity is indeed small, and a small neutron diffusion length should exist in the channel. This condition is necessary in order that phase change between two displaced detectors can be measured.

The reason for higher NMSV's for detector B may be due to higher void flow rate observed by detector B due to dissymmetry in void generation rate of the air bubble generator holes.

4. Pulsating air flow measurements

To establish the theoretical assumption of Eq. 14 that the spectral structure of voids passing the detectors is transferred to the detector current fluctuations a series of measurements were made with pulsating air flow rate.

A valve was placed in the air flow line and it was opened and closed at a constant rate in order to introduce a fixed frequency into the bubble flow pattern.

The results for an air flow rate of 0.15 cfm introduced at 12" input and detector A positioned at 24" is shown in Fig. 26 for a valve frequency of 0.72 Hz. It can be seen from the APSD plot that the fundamental valve frequency appears as a sharp peak proving that

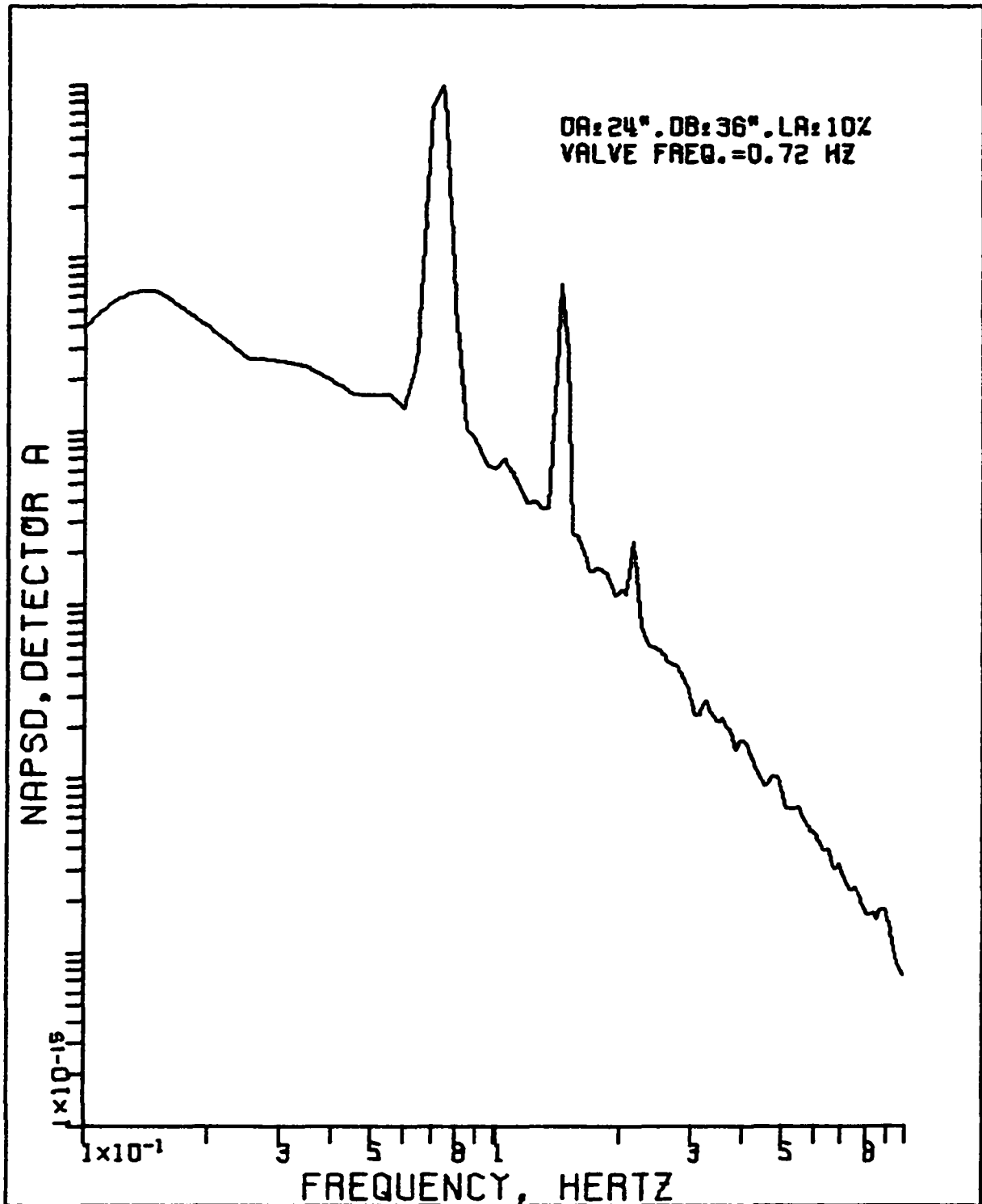


Figure 26. The NAPSD for an air pulsing frequency of 0.72 Hz

detector current fluctuations follow the fluctuations in void fraction. In addition to the fundamental frequency higher harmonics at 1.45 and 2.2 Hz appear quite strongly in the plot.

A second APSD plot is shown in Fig. 27 for a valve frequency of 1.89 Hz. It can be seen from this plot that in addition to the main peak due to the fundamental frequency there are three "lower harmonic" peaks at 0.47, 0.945 and 1.42 Hz. These so called "lower harmonics" are probably caused by standing waves and reversed flow patterns inside the channel.

These results make a strong case for the linearity of the system as is required for the application of linear system analysis methods.

5. Phase angle measurements

It was pointed out in section III.D.1 that if the local spectrum is much greater in magnitude than the global spectrum then a linear variation of phase angle as a function of frequency can be expected.

It was shown in Fig. 23 that a rather high air flow rate is required to raise the APSD curve substantially over the unperturbed APSD curve. It is necessary to know if the two detector signals do stay correlated over a significant frequency range for phase measurement to be

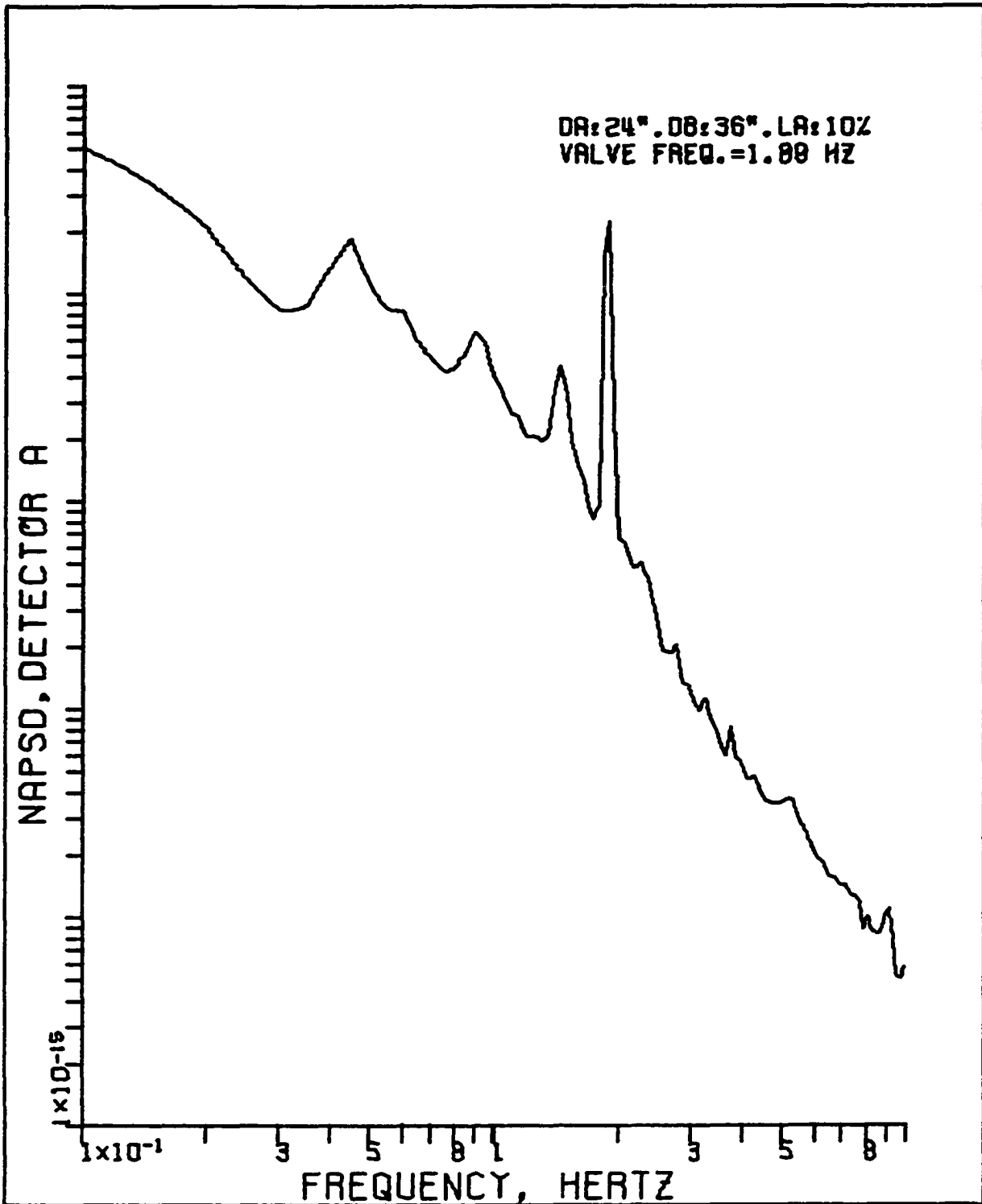


Figure 27. The NAPSD for an air pulsing frequency of 1.89 Hz

possible with the increased air flow rate.

Figure 28 shows a coherence function plot for the case of detector A at 24", detector B at 36" and 0.34 cfpm of air introduced at the 12" inlet. A comparison of Fig. 28 with Fig. 19 for the unperturbed coherence function shows that for a rather large air flow rate the coherence function of the detector signals is substantially reduced compared to the unperturbed case. The implication of this result is that the condition of strong local correlated spectrum for phase measurement cannot be met and some intermediate air flow rate should be used for phase measurements.

It was found experimentally that the smallest air flow rate that gives rise to measurable phase change between the two detectors when they are displaced from each other is about 0.06 cfpm.

Three plots of phase angle as a function of frequency are given in Fig. 29 for detector separations of 6, 9, and 12 inches and an air flow rate of 0.0659 cfpm. It can be seen from Fig. 29 that the slopes of the phase angle plots increase for increasing detector separation. This observation agrees with the basic premise of Eq. 35 but it should be pointed out that the slopes of the observed phase curves do not agree with expected values.

The slopes of the three curves of Fig. 29 can be found

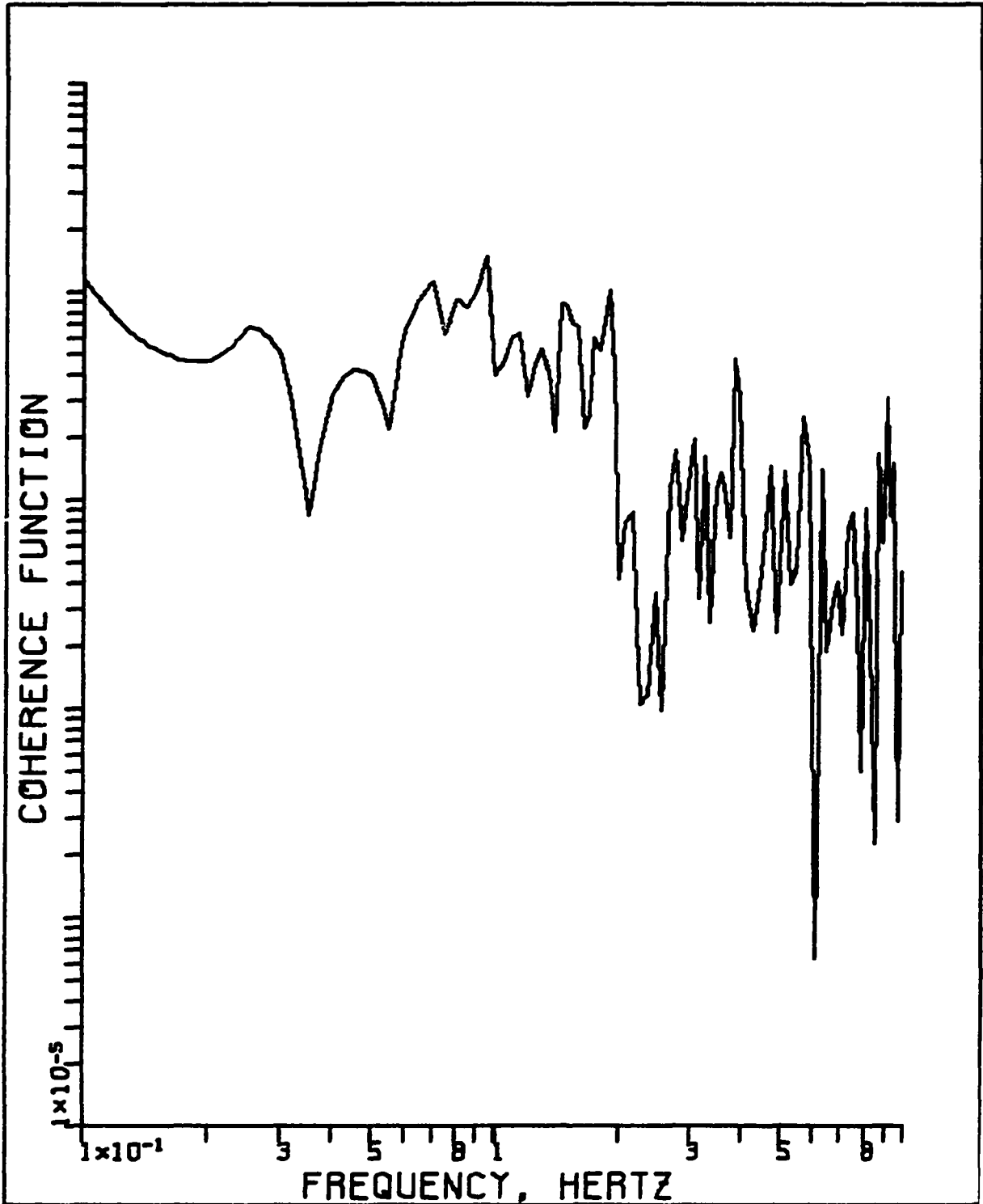


Figure 28. The coherence function for detector separation of 12 inches and air flow rate of 0.34 cfpm

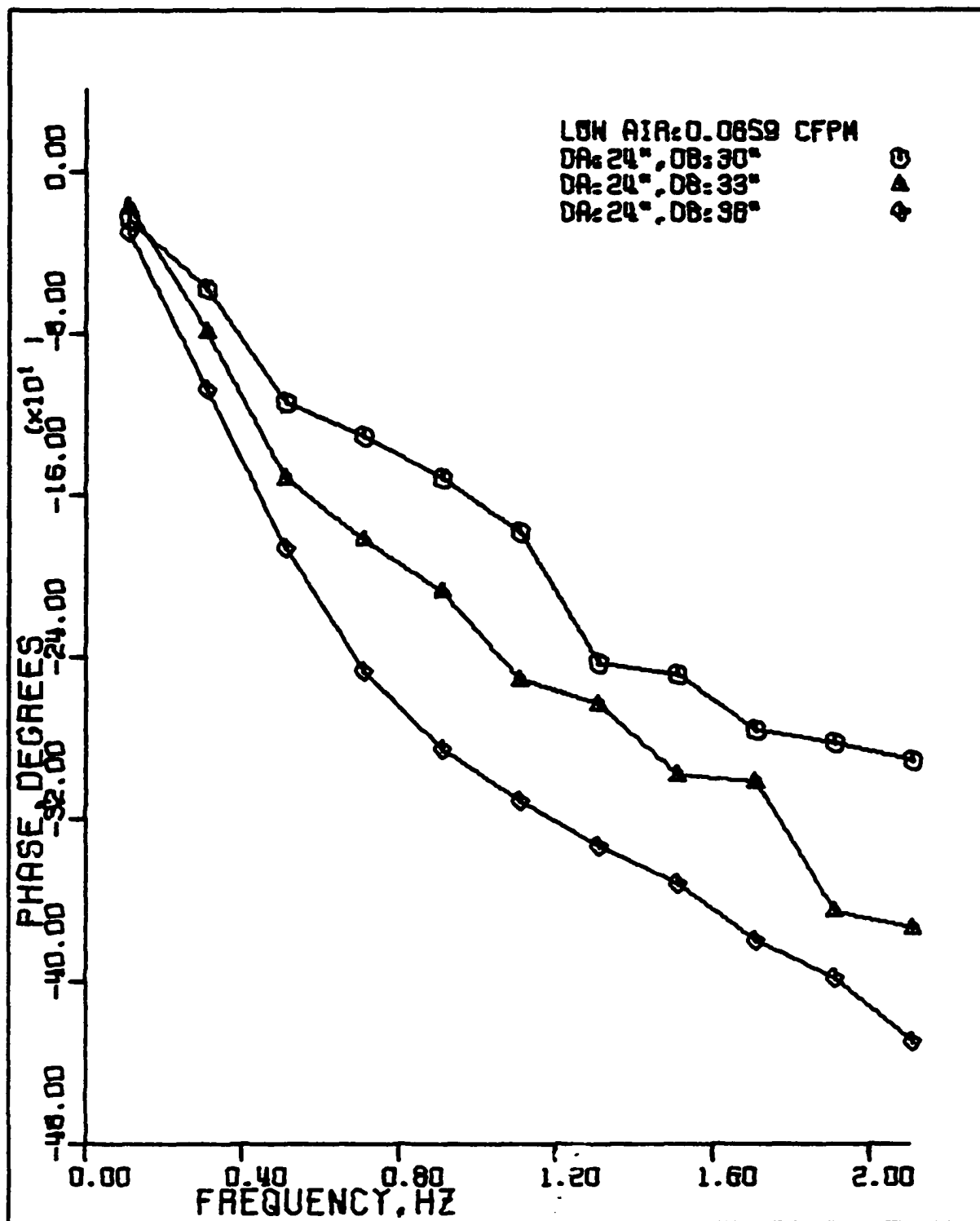


Figure 29. Phase angle versus frequency for three detector separation distances

by the method of linear regression and when used in conjunction with Eq. 35 yield bubble speeds of 0.40, 0.49, and 0.60 m/s for the three detector separation values of 6, 9 and 12 inches respectively. In addition to wide variation among each other, these bubble speed values deviate significantly from a bubble speed of 0.24 m/s measured in a transparent test channel.

It may thus be assumed that the phase curves are probably following the more exact description of Eq. 33, rather than the approximation of Eq. 35, due to low air flow rate used to produce them, and hence small value of $K_{12}(\omega)$.

6. The coherence function

It was shown in Section III.D, that when the two detectors are separated from each other while voids are introduced into the channel, the phase change between the detectors will manifest itself in the form of maxima and minima in the transfer and coherence function plots. It seems possible that the void travel time between the detectors may be estimated from the position of the maxima and minima in the transfer or coherence function plots.

Fig. 30 gives the coherence function plot for the case of detector A at 24", detector B at 36", and 0.0659 cfm of air introduced at 12". Figure 28 gives the coherence function for the same detector positions but with

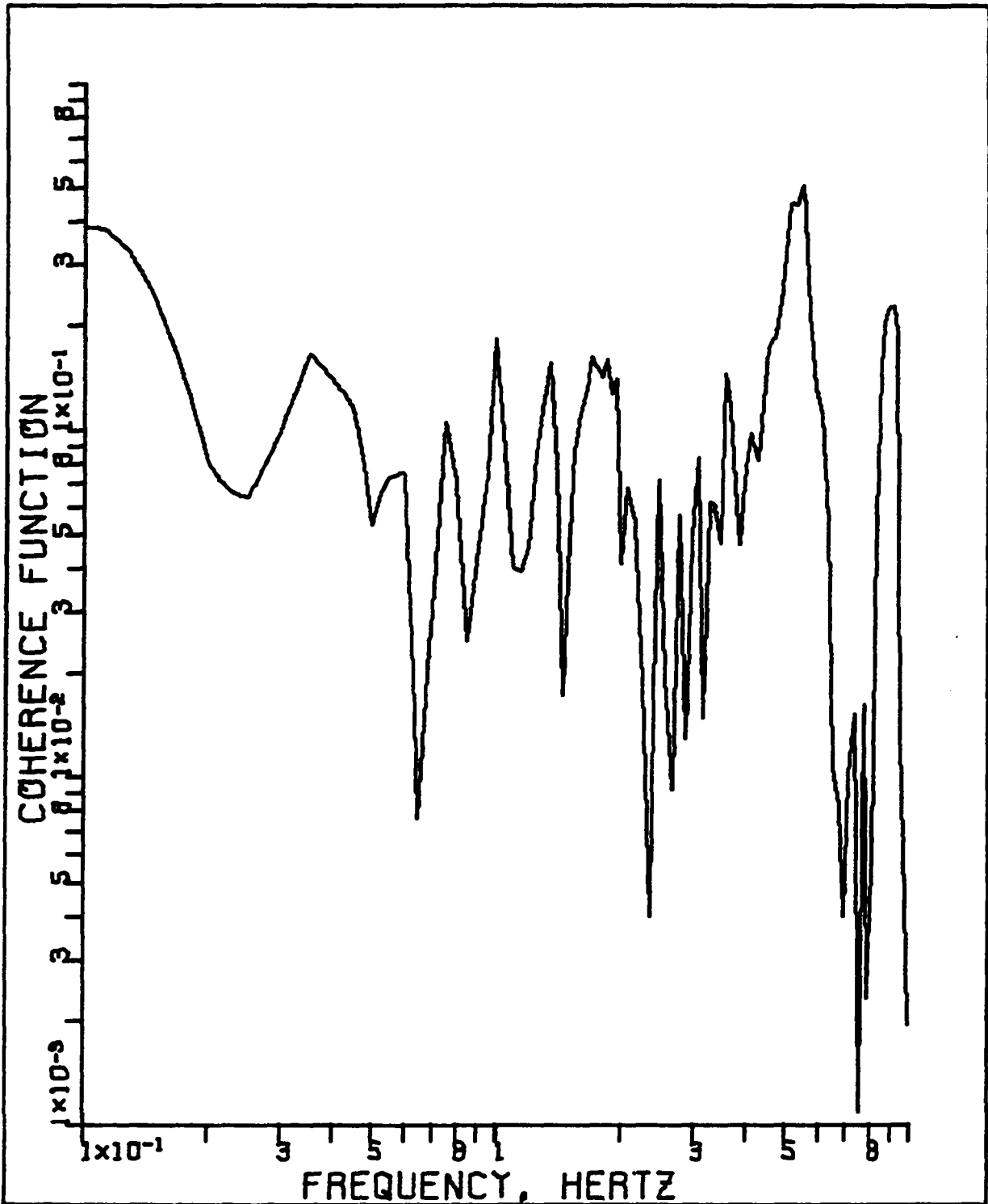


Figure 30. The coherence function for detector separation of 12 inches and air flow rate of 0.0659 cfm

an air flow rate of 0.34 cfpm.

These figures in addition to many other coherence function plots for other experimental conditions were examined to find out if bubble travel time between the two detectors can be found from the position of maxima and minima in them.

It can be seen from Figs. 28 and 30 that the coherence function plots contain a multitude of maxima and minima which are probably caused by statistical fluctuations as well as by phase difference between the detector signals.

It was found that in practice it is very difficult to estimate bubble transit time by looking for characteristic maxima and minima in the plots since they will be buried in a profusion of fluctuations in the plots.

E. Measurements with Boiling as the Source of Induced Perturbation

The results of measurements with air bubbles as the source of induced perturbation indicated that due to special design of air bubble generators, which are in the form of rings in the channel, with 4 holes to each ring, good correlation between detector signals was hard to obtain.

It was thus expected that with the use of a single heater a correlated source of perturbation could be obtained. To test this idea two series of measurements were carried out; one with a single heater and one with three heaters as

the source of induced perturbation.

1. Measurements with a single heater

Measurements with a single heater were carried out by operating one of the lower heaters at 1000 watts to generate steam bubbles with the other five heaters operated at a power 62.5 watts each to maintain operating temperature.

The results of the measurements indicated that a single heater, operated at the maximum power of 1000 watts, does not produce enough steam bubbles to afford phase angle measurements for two displaced detectors.

2. Measurements with three heaters

To increase the contribution of local perturbations so that phase measurement can be done, a series of measurements were made with the three lower heaters operated at 444 watts each and the three upper heaters operated at 62.5 watts each.

The NAPSD plots for detector A at 24" and detector B at 36" are given in Figs. 31 and 32 respectively. While the NAPSD of detector A seems to have a plateau region, the NAPSD of detector B lacks any such feature.

The plot of the coherence function for this case given in Fig. 33, indicates rather low correlation between the two detector signals.

A plot of the phase angle for this case given in Fig.

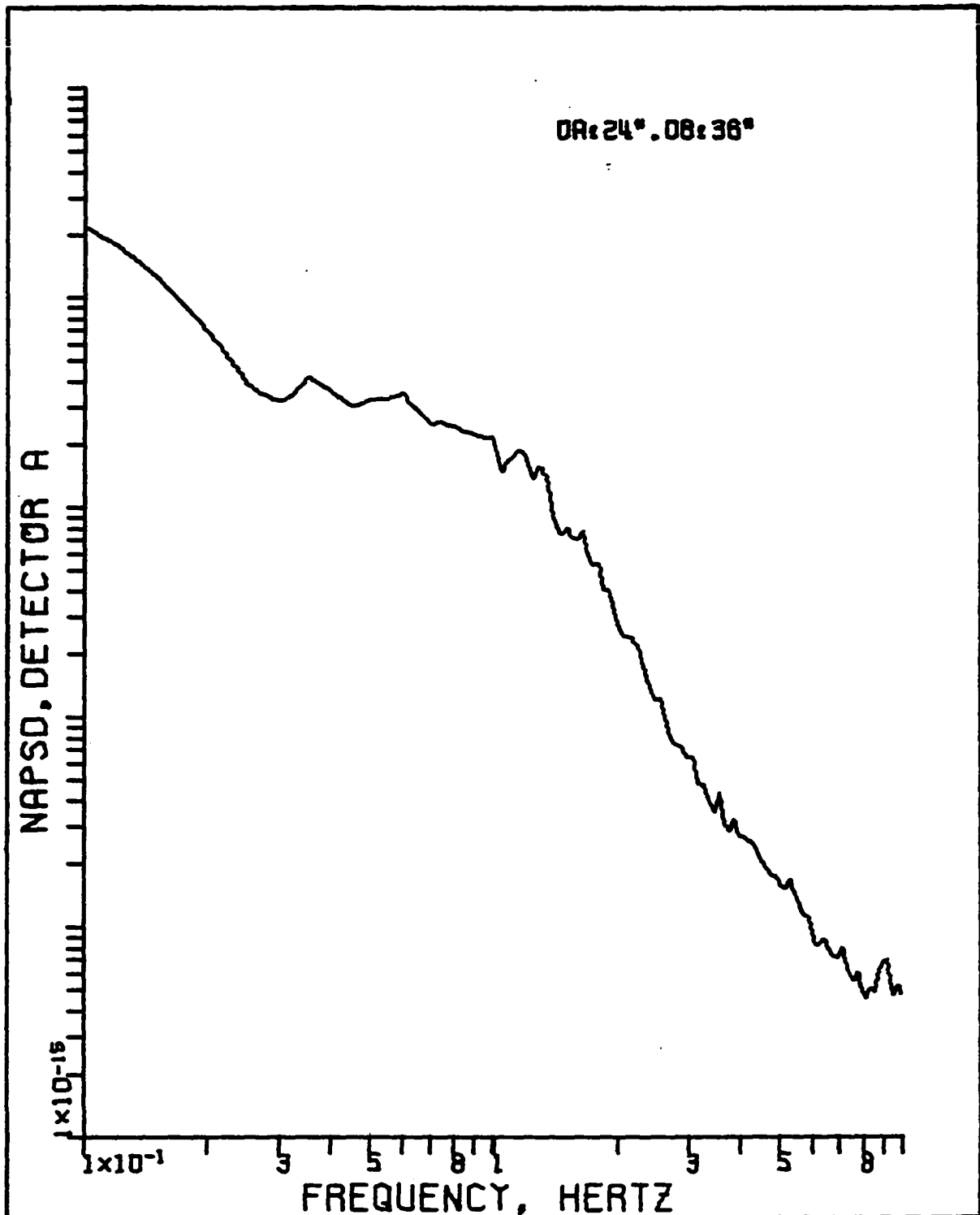


Figure 31. The NAPSD of detector A for the case of boiling with three heaters

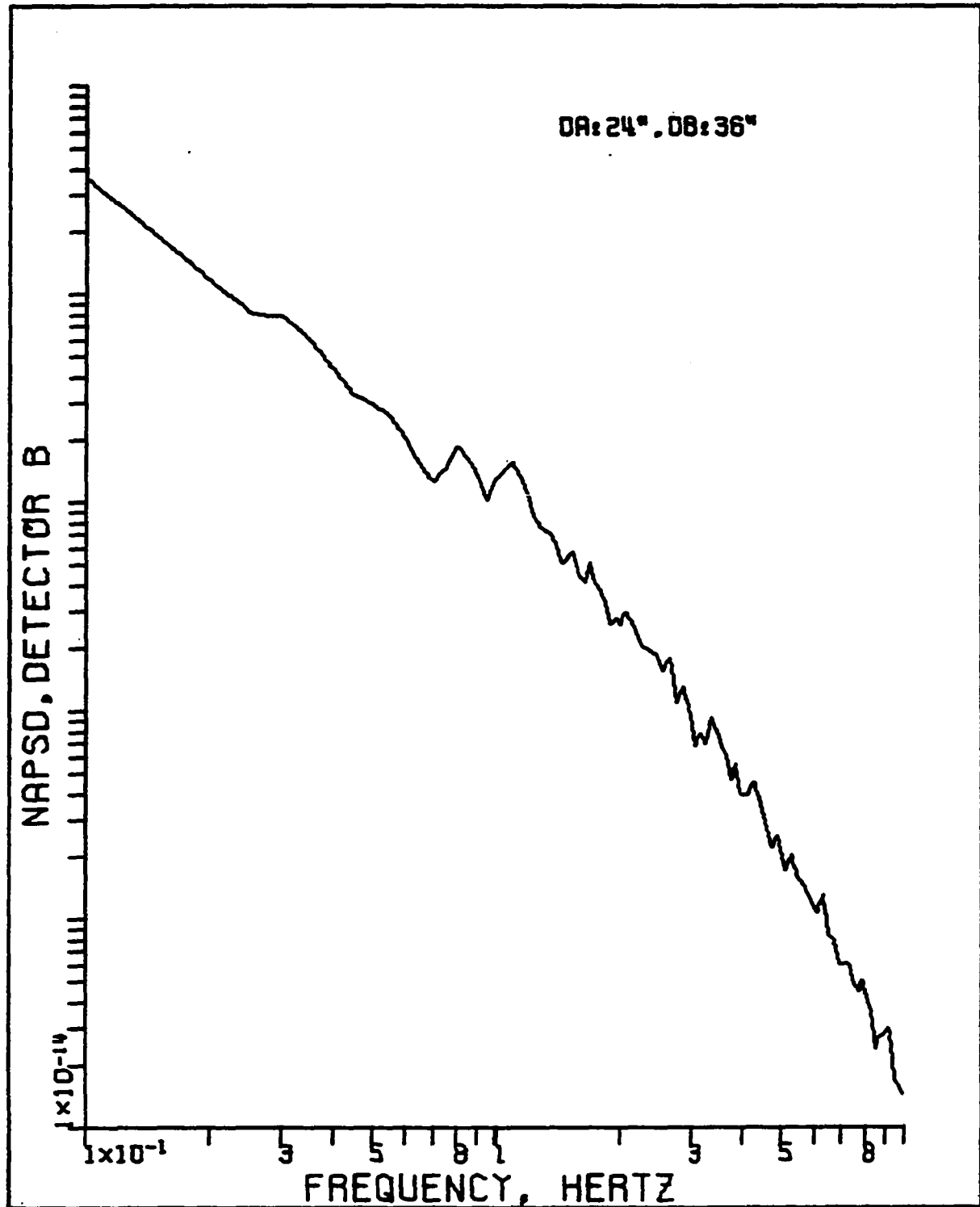


Figure 32. The NAPSD of detector B for the case of boiling with three heaters

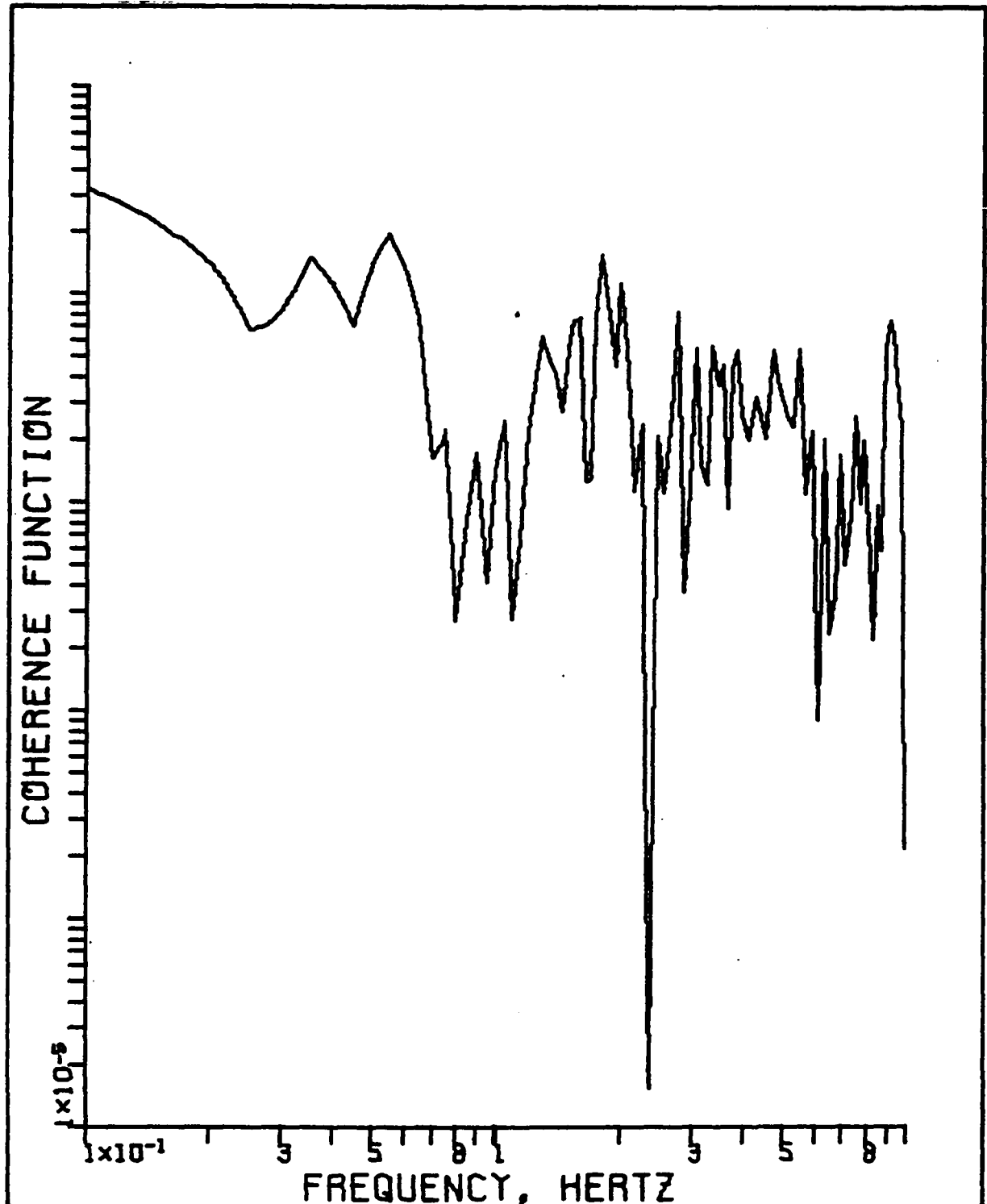


Figure 33. The coherence function for detector separation of 12 inches and boiling with three heaters

34 shows that, although some phase difference is measurable, no quantitative deduction can be made from the plot. Thus, even though the contribution of the local neutron noise component has been increased, it is still too low to allow phase angle measurements of interest.

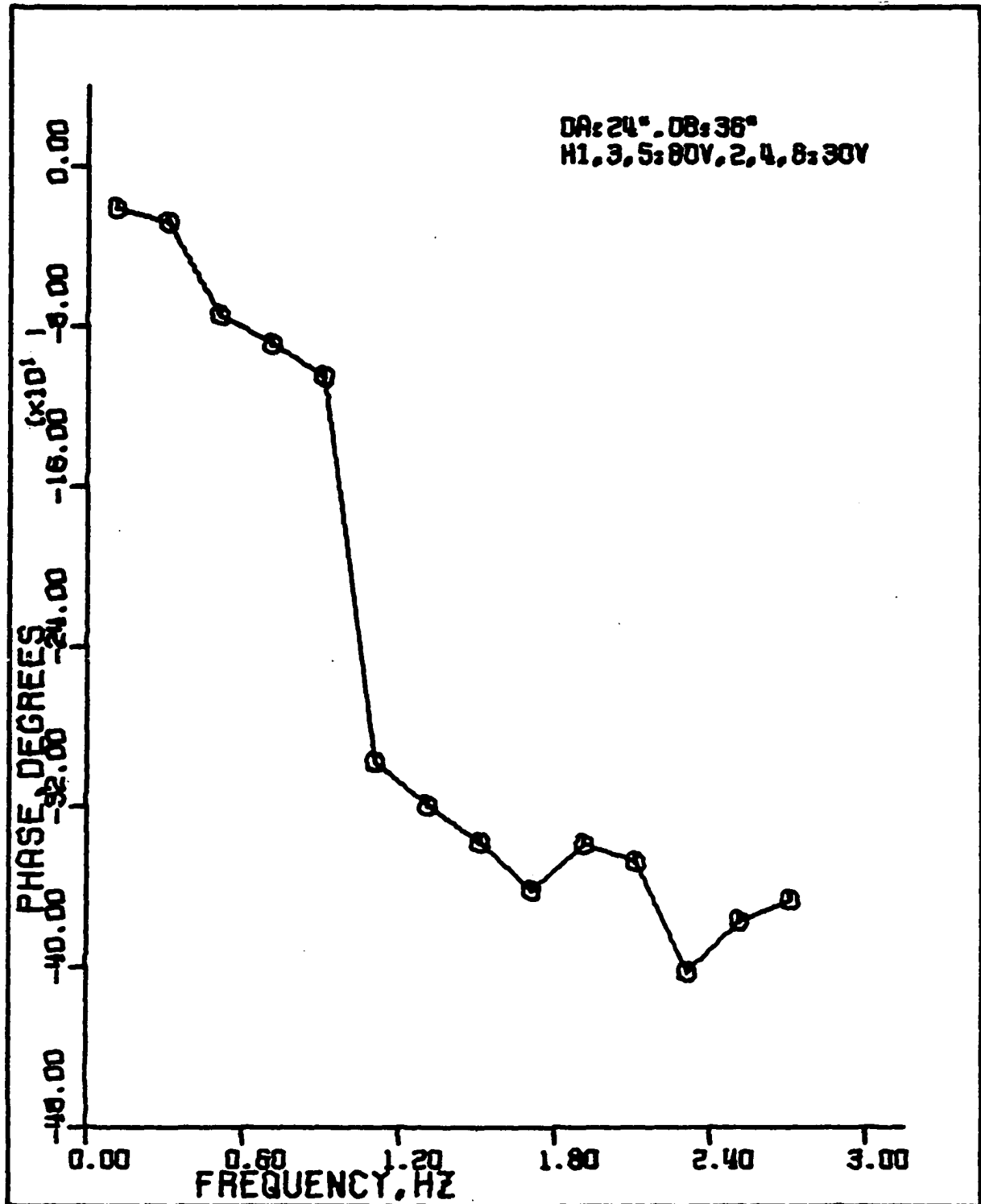


Figure 34. Phase angle vs. frequency for the case of boiling with three heaters

VII. DISCUSSION AND CONCLUSIONS

Based on the results of the experimental measurements the following conclusions can be stated:

1. The unperturbed reactor noise spectra were due to at-power reactor noise, which masked the zero-power reactor noise characteristics.

This conclusion is based on the experimental observation of near unity value of the coherence function, for frequencies lower than 1 Hz, as shown in Fig. 20, and estimated low detector efficiency.

2. As the void flow rate is increased in the channel small bubbles coalesce to form larger bubbles, thereby increasing the mean bubble volume in the channel.

This observation is based on the measurements of the NMSV of detector current fluctuations as a function of void flow rate as given in Fig. 22. The exponential behavior of the NMSV curves suggest that the mean bubble volume increases as the void flow rate increases in the channel.

3. The amplitudes of the NAPSD functions over the range of air flow rates investigated, showed strong dependence on air flow rate as is shown in Fig. 23. The effect of void fluctuations was more pronounced around 1 Hz demonstrating that the spectrum of void fluctuations is not white. The source of this spectral characteristic may be

void fraction fluctuations in the air column passing the detector due to bunching of bubbles.

4. The frequency spectrum of local air bubble perturbations, as shown in Fig. 24, did not show any recognizable characteristics due to the finite detector size effect. This negative result may have been caused by the finite frequency resolution of the spectrum, resulting in averaging of neighboring spectral values.

5. Experimental measurements given in Fig. 25 proved that a small volume of sensitivity associated with the void fluctuations exists in the channel as was predicted by the theory.

6. A necessary condition for linear system analysis, used in this work, was satisfied according to the results of measurements with pulsating air flow rates as shown in Figs. 26 and 27. These results pointed out that a fixed frequency component in void flow rate was followed exactly by the detector current fluctuations.

7. Phase lag measurements between two displaced detectors, in the presence of air voids, showed that at the high air flow rates, required to produce a strong local perturbation the coherence function of the detector signals is decreased (Fig. 28), making the task of void speed measurement impossible. On the other hand, low air flow rates, which preserved high coherence, did not produce

strong enough local perturbations to produce measurable phase lags. Measurements with intermediate values of air flow rate, showed consistent results, producing an increased phase lag with increasing detector separation (Fig. 29). The phase angle plots, however, showed pronounced deviations from a linear variation with frequency signifying that the linear phase lag approximation does not hold in this case.

8. Identification of the characteristic maxima and minima in the transfer function and coherence function plots, caused by the time lag of bubble movement between the detectors, was found to be impractical due to a profusion of peaks and valleys in the observed spectra caused by statistical variability of the results.

9. No pronounced difference was observed between the NAPSD functions measured with steam bubbles as the source of perturbation (Figs. 31 and 32) and those recorded with air bubbles as the source of perturbation (Fig. 23).

10. The amount of steam bubbles produced with a single heater operated at full power proved inadequate to produce a strong, coherent local perturbation to allow phase lag measurements.

Operation with three heaters produced results similar to the high air flow rate measurements. A decrease in the value of the coherence function was observed for two dis-

placed detectors as shown in Fig. 30. The phase angle measurement showed strong deviations from a linear variation with frequency as is shown in Fig. 34.

VIII. SUGGESTIONS FOR FUTURE WORK

The experimental channel at the ALRR can be used for at least two potentially important additional investigations in its present form. They are:

1. A probability distribution study of the detector signals under different void flow conditions in the channel.
2. A pattern recognition study on the APSD functions of the detector signals in the unperturbed case to study variations in the reactor noise source and their possible link to reactor mechanical malfunctions.

As a further improvement on the present system, a new experimental channel, with the following capabilities can be constructed:

1. Induced coolant flow or recirculation.
2. Induced pressure variations.
3. Improved heat exchanger to allow more intense boiling in the channel.
4. Improved local perturbation measurement by the use of smaller neutron detectors.
5. Neutron thermalization studies by positioning the experimental channel inside the reactor core.

6. Use of other detectors, like acoustic detectors and short response time thermocouples.

IX. LITERATURE CITED

1. Albrecht, R. W. 1972. The use of signal coherence for anomaly detection in nuclear reactors. Nuc. Technol. 14:208-217.
2. Bendat, J. S., and A. G. Piersol. 1971. Random data: Analysis and measurement procedures. John Wiley and Sons, Inc., New York, N.Y.
3. Binford, F. T. 1965. Boiling Detection Experiment. Pages 30-34 in Oak Ridge Research Reactor Quarterly Report, April, May, June 1965. ORNL-TM-1290. (Oak Ridge National Laboratory, Oak Ridge, Tenn.)
4. Blomberg, P. E., and F. Akerhielm. 1975. A contribution to the experience of noise measurements and analysis in BWR power plants. Annals of Nuclear Energy 2:323-331.
5. Boyce, W. E., and R. C. DiPrima, 1969. Elementary differential equations and boundary value problems. 2nd ed. John Wiley and Sons, Inc., New York, N.Y. 124 pp.
6. Boyd, L. R. 1956. Detection of nucleate boiling by flux variation measurement. USAEC Report KAPL-M-LRB-3, (Knolls Atomic Power Laboratory, Schnectady, N.Y.)
7. Cohn, C. E. 1960. A simplified theory of pile noise. Nucl. Sci. Eng. 7:472-475.
8. Colomb, A. L., and F. T. Binford, 1962. The detection of boiling in a water-cooled reactor. ORNL-TM-274. (Oak Ridge National Laboratory, Oak Ridge, Tenn.)
9. Cooper, G. R., and C. D. McGillen. 1971. Probabilistic methods of signal and system analysis. Holt, Rinehart and Winston, Inc., New York, N.Y. 142 pp.
10. Dam, van H. 1976. Neutron noise in boiling water reactors. Atomkernenergie 27(1):8-14.

11. Hetrick, D. L. 1971. Dynamics of nuclear reactors. The University of Chicago Press, Chicago, Ill.
12. Jordan, E. L. 1966. Detection of in-core void formation by noise analysis. Am. Nuc. Soc., Trans. 9:317-318.
13. Kosaly, G. 1975. Investigation of the local component of power-reactor noise via diffusion theory. Central Research Institute for Physics Report KFKI-75-27. (Central Research Institute for Physics, Budapest, Hungary).
14. Kosaly, G. and L. Mesko. 1976. Theory of the auto-spectrum of the local component of power-reactor noise. Annals of Nuclear Energy 3(4):233-236.
15. Kosaly, G., L. Morati, and L. Mesko. 1975. A simple space dependent theory of the neutron noise in a boiling water reactor. Annals of Nuclear Energy 2: 315-321.
16. Lamarsh, J. R. 1966. Introduction to nuclear reactor theory. Addison-Wesley Publishing Company, Inc., Reading, Mass. 145 pp.
17. Lu, J. T., R. A. Danofsky, and R. Struss. 1975. Diagnostics of void fluctuations in a reactor coolant channel using neutron noise techniques. Pages 21-1-21-28 in T. W. Kerlin, ed. Proceedings of the Second Power Plant Dynamics, Control and Testing Symposium. University of Tennessee, Knoxville, Tennessee.
18. Mogil'ner, A. I. 1971. Noise associated with inhomogeneities in the heat carrier of a reactor. Soviet Atomic Energy 30:629-634.
19. Nomura, T. 1968. Noise analysis of boiling water reactor. Pages 197-210 in Proceedings of Japan-United States Seminar on Nuclear Reactor Noise Analysis, Tokyo and Kyoto, Japan.
20. Otnes, R. K., and L. Enochson. 1972. Digital time series analysis. John Wiley and Sons, Inc., New York, N.Y.

21. Pallagi, D., et al. 1975. Power Reactor Noise Measurements in Hungary. *Annals of Nuclear Energy* 2:333-335.
22. Rajagopal, V. 1963. Reactor noise measurements on Saxton reactor. Pages 427-448 in *Proceedings of AEC Symposium on Noise Analysis in Nuclear Systems*, Gainesville, Fla.
23. Rothman, P. 1973. Neutron noise in boiling reactors. *Atomkernenergie* 21(2):113-118.
24. Saxe, R. F. 1966. Detection of boiling in water-moderated nuclear reactors. *Nucl. Safety* 7(4):452-456.
25. Saxe, R. F. 1967. Survey of boiling detection methods in reactors. Pages 41-57 in *Proceedings of Conference on Incipient Failure Diagnosis for Assuring Safety and Availability of Nuclear Power Plants*, Gatlinburg, Tennessee.
26. Schultz, M. A. 1961. *Control of nuclear reactors and power plants*. 2nd ed. McGraw-Hill, New York, N.Y. 85 pp.
27. Seifritz, W. 1970. At power reactor noise induced by fluctuations in the coolant flow. *Atomkernenergie* 16(1):29-34.
28. Seifritz, W. 1972. An analysis of the space dependent neutron flux density fluctuations at the Lingen boiling water reactor (KWL) by methods of stochastic processes. *Atomkernenergie* 19(4):271-279.
29. Seifritz, W., and F. Cioli. 1973. On-load monitoring of local steam velocity in BWR cores by neutron noise analysis. *Am. Nuc. Soc., Trans.* 17:451-453.
30. Stegemann, D., et al. 1973. Operating characteristics of a boiling water reactor deduced from in-core measurements. Pages 15-1-15-17 in T. W. Kerlin, ed. *Power Plant Dynamics Control and Testing and Applications Symposium*. University of Tennessee, Knoxville, Tenn.

31. Thie, J. A. 1968. Noise in power reactor - a review of experiment, analysis, and theory. Reactor and Fuel Processing Technology 11(4):167-171.
32. Thie, J. A. 1975. Instrumentation integrity and response time testing utilizing system noise. Pages 10-1-10-18 in T. W. Kerlin ed. Proceedings of the Second Power Plant Dynamics, Control and Testing Symposium, University of Tennessee, Knoxville, Tennessee.
33. Wach, D., and G. Kosaly. 1974. Investigation of the joint effect of local and global driving sources in in-core neutron noise measurements. Atomkernenergie 23(4):244-250.

X. ACKNOWLEDGMENTS

The author is indebted to his major professors, Dr. R. A. Hendrickson and Dr. R. A. Danofsky for their continuous interest in the project from the design stage to the end, and their numerous helpful suggestions.

The services of the staff of the Ames Laboratory of ERDA were invaluable in making the project possible. The experimental channel was designed and fabricated by Mr. Roland Struss and his staff. The electronics equipment was designed and constructed by Mr. Harold Skank and his staff. The computer programming was done by Mr. Dennis Jensen.

Funds for the equipment were provided by an Iowa State University Research Foundation Grant which was awarded to Dr. R. A. Hendrickson and Dr. R. A. Danofsky.

XI. APPENDIX A: POWER SPECTRAL DENSITY OF THE
FLUCTUATIONS IN THE NEUTRON DENSITY OF THE
REACTOR SYSTEM OF FIG. 1

The differential equations in the time domain describing the reactor system of Fig. 1 are the point reactor kinetic equations [11, 26]:

$$\frac{dN(t)}{dt} = \frac{\rho_t(t) - \beta}{\Lambda} N(t) + \sum_i \lambda_i C_i(t) + U(t), \quad (A1)$$

and

$$\frac{dC_i(t)}{dt} = -\lambda_i C_i(t) + \frac{\beta_i}{\Lambda} N(t), \quad (A2)$$

where $N(t)$ is the neutron density, $C_i(t)$ is the delayed neutron precursor density of group i , λ_i is the decay constant of i th delayed neutron group, β_i is the i th delayed neutron group fraction, β is the total delayed neutron fraction given by $\beta = \sum_i \beta_i$, Λ is the prompt neutron generation time, $U(t)$ is a neutron source term, and $\rho_t(t)$ is the total reactivity of the system.

The relationship between the total reactivity, $\rho_t(t)$, the components of the multiple reactivity input vector, $\rho_k(t)$, and the feedback reactivity, $\rho_f(t)$, may be expressed for the delayed critical reactor ($\overline{\rho_t(t)} = 0$) as

$$\rho_t(t) = \sum_{k=1}^K \rho_k(t) + \rho_f(t) . \quad (A3)$$

The feedback reactivity term can be expressed [11] as

$$\rho_f(t) = \sum_{m=1}^M \int_0^{\infty} h_m(\tau) [N(t-\tau) - N_0] d\tau, \quad (A4)$$

where $h_m(\tau)$ denote the individual feedback kernels of the parallel feedback paths, and N_0 is the average neutron density in the system.

The neutron density $N(t)$, the precursor densities $C_i(t)$, and the source $U(t)$ are assumed to be stochastically varying due to the random nature of driving processes. They can be divided into a time averaged part and a small fluctuating part

$$N(t) = N_0 + n(t), \quad (A5)$$

$$C_i(t) = C_{i0} + c_i(t), \quad (A6)$$

and

$$U(t) = U_0 + u(t) . \quad (A7)$$

If Eqs. A3-A7 are substituted in Eqs. A1 and A2, the result is

$$\begin{aligned} \frac{dn(t)}{dt} = & \frac{1}{\Lambda} \left[\sum_{k=1}^K \rho_k(t) + \sum_{m=1}^M \int_0^{\infty} h_m(\tau) n(t-\tau) d\tau \right] [N_0 + n(t)] \\ & - \frac{\beta}{\Lambda} [N_0 + n(t)] + \sum_i \lambda_i [C_{i0} + c_i(t)] + U_0 + u(t) , \quad (A8) \end{aligned}$$

and

$$\frac{dc_i(t)}{dt} = -\lambda_i [C_{i0} + c_i(t)] + \frac{\beta_i}{\Lambda} [N_0 + n(t)]. \quad (\text{A9})$$

At steady state conditions, Eq. A9 reduces to

$$\lambda_i C_{i0} = \frac{\beta_i}{\Lambda} N_0, \quad (\text{A10})$$

which yields

$$\sum_i \lambda_i C_{i0} = \frac{N_0}{\Lambda} \beta. \quad (\text{A11})$$

If Eq. A8 is linearized by noting that $n(t) \ll N_0$, and it is assumed that no steady neutron source is present, i.e., $U_0 = 0$, and Eq. A11 is used, it is found that

$$\begin{aligned} \frac{dn(t)}{dt} = & \frac{N_0}{\Lambda} \left[\sum_{k=1}^K \rho_k(t) + \sum_{m=1}^M \int_0^{\infty} h_m(\tau) n(t-\tau) d\tau \right] \\ & - \frac{\beta}{\Lambda} n(t) + \sum_i \lambda_i c_i(t) + u(t). \end{aligned} \quad (\text{A12})$$

Substitution of Eq. A10 in Eq. A9 yields

$$\frac{dc_i(t)}{dt} = -\lambda_i c_i(t) + \frac{\beta_i}{\Lambda} n(t). \quad (\text{A13})$$

The Laplace transform of the coupled set of linear differential equations A12 and A13 is

$$\begin{aligned}
 sn(s) = & \frac{N_0}{\Lambda} \left[\sum_{k=1}^K \rho_k(s) + \sum_{m=1}^M H_m(s)n(s) \right] \\
 & - \frac{\beta}{\Lambda} n(s) + \sum_i \lambda_i c_i(s) + u(s), \tag{A14}
 \end{aligned}$$

and

$$sc_i(s) = -\lambda_i c_i(s) + \frac{\beta_i}{\Lambda} n(s) . \tag{A15}$$

The simultaneous solution of Eqs. A14 and A15 yields

$$n(s) = H_s(s) \left[\frac{N_0}{\Lambda} \sum_{k=1}^K \rho_k(s) + u(s) \right], \tag{A16}$$

where $H_s(s)$ is the overall system source transfer function given by

$$H_s(s) = \frac{H_{s0}(s)}{1 - \frac{N_0}{\Lambda} H_{s0}(s) \sum_{m=1}^M H_m(s)}, \tag{A17}$$

in which $H_{s0}(s)$ represents the zero power reactor source transfer function given by

$$H_{s0}(s) = \frac{\Lambda}{s(\Lambda + \sum_i \frac{\beta_i}{s + \lambda_i})}, \tag{A18}$$

If it is noted that $s = i\omega$, and $\Lambda = \ell$ for a critical reactor, the power spectral density of neutron fluctuations can be derived from Eq. A16 by

$$\phi_{n,gl}(\omega) = |n(\omega)|^2 = n(\omega)n^*(\omega), \quad (A19)$$

or

$$\phi_{n,gl}(\omega) = |H_s(\omega)|^2 \left[\frac{N_o}{\ell} \phi_\rho(\omega) + \phi_u(\omega) \right], \quad (A20)$$

where

$$\phi_\rho(\omega) = \sum_{k=1}^K |\rho_k(\omega)|^2 + \sum_{i=1}^N \sum_{\substack{j=1 \\ i \neq j}}^N \rho_i(\omega) \rho_j^*(\omega), \quad (A21)$$

is the spectral density of the extraneous reactivity inputs, and

$$\phi_u(\omega) = |u(\omega)|^2 = \frac{N_o \bar{v}D}{\ell}, \quad (A22)$$

is the spectral density of the noise equivalent source.

In derivation of Eq. A20 it has been assumed that the source term $u(\omega)$ is uncorrelated with the random reactivity terms $\rho_k(\omega)$.

Eq. A20 can also be written in the form

$$\phi_{n,gl}(\omega) = |H_r(\omega)|^2 [\phi_\rho(\omega) + \phi_{\rho_u}(\omega)], \quad (A23)$$

where $H_r(\omega)$ is the reactivity transfer function given by

$$H_r(\omega) = \frac{N_o}{\ell} H_s(\omega), \quad (A24)$$

and $\phi_{\rho_u}(\omega)$ is the spectral density of noise equivalent

reactivity source [7] given by

$$\phi_{\rho_u}(\omega) = \frac{\ell \bar{v} D}{N_o} . \quad (\text{A25})$$

XII. APPENDIX B: VOID FRACTION FLUCTUATIONS
AND THEIR AUTO- AND CROSS-SPECTRA

A. Void Fraction Fluctuations

Following the formulation of Kosaly, et al. [15], the number density of bubbles of volume v at the position z along a boiling channel can be represented as

$$B(z,t,v) = B_0(z,v) + b(z,t,v), \quad (B1)$$

with a corresponding equation for bubble current density given by

$$J(z,t,v) = J_0(z,v) + j(z,t,v). \quad (B2)$$

In Eqs. B1 and B2 the first terms on the right hand side represent time averaged values and the second terms represent fluctuating components.

The bubble number density and bubble current density are related to each other by the relationship

$$J(z,t,v) = V(z)B(z,t,v), \quad (B3)$$

in which $V(z)$ is the average bubble speed at position z in the channel, and which also holds for the mean and fluctuating components as given in Eqs. B1 and B2.

Along the same line, the bubble source at any position z can be written as

$$G(z, t, v) = G_0(z, v) + g(z, t, v). \quad (\text{B4})$$

If two axial positions z_1 and z_2 are considered, with $z_1 \leq z \leq z_2$, the bubble current at position z_2 can be written as

$$J(z_2, t, v) = J(z_1, t - \tau_{z_1, z_2}, v) + \int_{z_1}^{z_2} G(z, t - \tau_{z, z_2}, v) dz, \quad (\text{B5})$$

where τ_{z_1, z_2} and τ_{z, z_2} stand for the mean transit times of bubbles between z_1 and z_2 , and z and z_2 respectively. Eq. (B5) represents an equation of continuity in bubble current density, which does not take into account any variation in bubble volume between positions z_1 and z_2 .

The fluctuations in the void fraction at any position z can be written as

$$\alpha(z, t) = \frac{\int_0^{v_m} vb(z, t, v) dv}{\int_0^{v_m} dv}, \quad (\text{B6})$$

or

$$\alpha(z, t) = \frac{1}{v_m V(z)} \int_0^{v_m} vj(z, t, v) dv, \quad (\text{B7})$$

where v_m is the maximum possible value for bubble volume in the channel.

With the use of Eqs. B2, B3, and B4, Eq. B5 can be written as

$$\begin{aligned}
 V(z_2)B_o(z_2, v) + V(z_2)b(z_2, t, v) = \\
 V(z_1)B_o(z_1, v) + V(z_1)b(z_1, t - \tau_{z_1, z_2}, v) + \\
 \int_{z_1}^{z_2} G_o(z, v) dz + \int_{z_1}^{z_2} g(z, t - \tau_{z, z_2}, v) dz, \quad (B8)
 \end{aligned}$$

which at steady state reduces to

$$V(z_2)B_o(z_2, v) = V(z_1)B_o(z_1, v) + \int_{z_1}^{z_2} G_o(z, v) dz . \quad (B9)$$

If Eq. B9 is subtracted from Eq. B8 a relationship between the small fluctuating terms is found to be

$$\begin{aligned}
 V(z_2)b(z_2, t, v) = V(z_1)b(z_1, t - \tau_{z_1, z_2}, v) + \\
 \int_{z_1}^{z_2} g(z, t - \tau_{z, z_2}, v) dz. \quad (B10)
 \end{aligned}$$

If this equation is multiplied by v and integrated over v the result is

$$V(z_2)\alpha(z_2, t) = V(z_1)\alpha(z_1, t - \tau_{z_1, z_2}) + \frac{1}{v_m} \int_0^{v_m} v \, dv \int_{z_1}^{z_2} g(z, t - \tau_{z, z_2}, v) \, dz, \quad (\text{B11})$$

where Eq. B6 has been used.

The fluctuations in void fraction at position z_2 can be found from Eq. B11 to be

$$\alpha(z_2, t) = \frac{V(z_1)}{V(z_2)} \alpha(z_1, t - \tau_{z_1, z_2}) + \alpha'(z_1, z_2, t), \quad (\text{B12})$$

where

$$\alpha'(z_1, z_2, t) = \frac{1}{v_m V(z_2)} \int_0^{v_m} v \, dv \int_{z_1}^{z_2} g(z, t - \tau_{z, z_2}, v) \, dz \quad (\text{B13})$$

represents additional fluctuations in void fraction at z_2 which are introduced between z_1 and z_2 .

B. The Auto- and Cross-Spectra of Void Fraction Fluctuations

The fluctuations in void fraction at any position along the voided channel can be written as

$$\alpha(z, t) = \frac{1}{v_m V(z)} \int_0^{v_m} \int_0^z v g(z_0, t - \tau_{z_0, z}, v) \, dz_0 \, d_v, \quad (\text{B14})$$

where Eq. B7 has been used with the understanding that

$$j(z, t, v) = \int_0^z g(z_0, t - \tau_{z_0, z}, v) dz. \quad (B15)$$

The auto-correlation function (ACF) of void fraction fluctuations is by definition given by

$$R_\alpha(z, \epsilon) = E[\alpha(z, t)\alpha(z, t+\epsilon)], \quad (B16)$$

where E stands for the expectation operator.

Application of Eq. B14 in B16 yields

$$R_\alpha(z, \epsilon) = \frac{1}{v_m^2 V^2(z)} E \left[\int_0^{v_m} \int_0^z v' g(z', t - \tau_{z', z}, v') dz' dv' \right. \\ \left. \int_0^{v_m} \int_0^z v'' g(z'', t + \epsilon - \tau_{z'', z}, v'') dz'' dv'' \right],$$

which reduces to

$$R_\alpha(z, \epsilon) = \frac{1}{v_m^2 V^2(z)} \int_0^{v_m} v' dv' \int_0^z dz' \int_0^{v_m} v'' dv'' \\ \int_0^z dz'' R_{g', g''}(\tau_{z', z} + \epsilon - \tau_{z'', z}). \quad (B17)$$

In Eq. B17, $R_{g', g''}$ stands for the cross-correlation function (CCF) between the bubble sources $g(z', t - \tau_{z', z}, v')$ and $g(z'', t - \tau_{z'', z}, v'')$. If it is assumed that there is no correlation between these two sources unless $z' = z''$ and $v' = v''$, the CCF $R_{g', g''}$ reduces to the ACF $R_{g'}$, and Eq. B17

reduces to

$$R_{\alpha}(z, \varepsilon) = \frac{1}{v_m^2 V^2(z)} \int_0^{v_m} v'^2 dv' \int_0^z R_g(z', \varepsilon, v') dz'. \quad (\text{B18})$$

The spectral density of the void fraction fluctuations is found by taking the Fourier transform of Eq. B18, and is given by

$$\phi_{\alpha}(z, \omega) = \frac{1}{v_m^2 V^2(z)} \int_0^{v_m} v'^2 dv' \int_0^z \phi_g(z', \omega, v') dz'. \quad (\text{B19})$$

To evaluate the spectral density $\phi_g(z', \omega, v')$ of the bubble source $g(z', t, v')$ it is assumed that the fluctuations in the bubble source are band-limited white noise, from which it follows [9] that the spectral density is a constant given by

$$\phi_g(z', v') = \frac{1}{2W} \overline{g^2(z', t, v')} \quad (\text{B20})$$

where W is the bandwidth.

Thus to evaluate the spectral density ϕ_g it will be necessary to evaluate the mean-square value of source fluctuations.

It can be seen from Eq. B4 that

$$g^2 = (G - G_0)^2$$

the mean-square value of which is by definition given by

$$\overline{g^2} = E[(G-G_0)^2],$$

or

$$\overline{g^2} = \overline{G^2} - G_0^2,$$

which means that $\overline{g^2}$ is equal to the variance of the bubble source $G(z,t,v)$.

If it is assumed that G is a Poisson distributed source, then the variance of G is equal to its mean value G_0 , so that

$$\overline{g^2} = G_0,$$

which when used in Eq. B20 yields

$$\phi_g(z',v') = \frac{1}{2W} G_0(z',v'). \quad (B21)$$

Application of Eq. B21 in B19 yields

$$\phi_\alpha(z,\omega) = \frac{1}{2v_m^2 V^2(z)W} \int_0^{v_m} v'^2 J_0(z,v') dv', \quad (B22)$$

where the relationship

$$J_0(z,v') = \int_0^z G_0(z',v') dz'$$

has been used.

Eq. B22 can be written in a more fundamental form as

$$\phi_\alpha(z,\omega) = \frac{\alpha(z) \overline{v^2(z)}}{2v_m \overline{v(z)} V(z)W}, \quad (B23)$$

where $\overline{v^2(z)}$, the second moment of the bubble volume at the axial position z , is given by

$$\overline{v^2(z)} = \frac{\int_0^{v_m} v^2 B_o(z, v) dv}{\int_0^{v_m} B_o(z, v) dv}, \quad (\text{B24})$$

and $\alpha(z)$, the local mean void fraction, is given by

$$\alpha(z) = \frac{\overline{v(z)}}{v_m} \int_0^{v_m} B_o(z, v') dv', \quad (\text{B25})$$

where $\overline{v(z)}$ is the mean bubble volume at position z .

If it is assumed that

$$\overline{v^2(z)} \approx \overline{v(z)}^2 \quad (\text{B26})$$

Eq. B23 can be written as

$$\phi_\alpha(z, \omega) = C \frac{\alpha(z) \overline{v(z)}}{\overline{v(z)}}, \quad (\text{B27})$$

where C is a constant given by

$$C = \frac{1}{2v_m W}.$$

The cross-spectral density function of void fraction fluctuations at two axial positions can be found by noting that the CCF is given by

$$R_{\alpha; z_1, z_2}(\epsilon) = E[\alpha(z_1, t)\alpha(z_2, t+\epsilon)]. \quad (\text{B28})$$

Application of Eq. B12 in B28 yields

$$R_{\alpha; z_1, z_2}(\epsilon) = E\left[\frac{V(z_1)}{V(z_2)} \alpha(z_1, t)\alpha(z_1, t-\tau_{z_1, z_2} + \epsilon) + \alpha(z_1, t)\alpha'(z_1, z_2, t+\epsilon)\right],$$

which reduces to

$$R_{\alpha; z_1, z_2}(\epsilon) = \frac{V(z_1)}{V(z_2)} R_{\alpha}(z_1, \epsilon - \tau_{z_1, z_2}). \quad (\text{B29})$$

The cross-spectral density function is found by Fourier transformation of Eq. B29, and is given by

$$\Psi_{\alpha; z_1, z_2}(\omega) = \frac{V(z_1)}{V(z_2)} \Phi_{\alpha}(z_1, \omega) e^{-i\omega\tau_{z_1, z_2}}. \quad (\text{B30})$$

With the application of Eq. B27, Eq. B30 can be written in the form

$$\Psi_{\alpha; z_1, z_2}(\omega) = C \frac{\alpha(z_1)\overline{v(z_1)}}{V(z_2)} e^{-i\omega\tau_{z_1, z_2}}. \quad (\text{B31})$$

XIII. APPENDIX C: FLUCTUATIONS IN FLUX AS A FUNCTION
OF FLUCTUATIONS IN VOID FRACTION

To solve Eq. 11 for fluctuations in flux as a function of fluctuations in void fraction it is assumed that $\bar{D}(z,t)$, $\bar{\Sigma}_a(z,t)$, and $\phi(z,t)$ can be divided into a constant and a time varying component as suggested by Kosaly [13], i.e.,

$$\bar{D}(z,t) = \bar{D}(z) + \delta\bar{D}(z,t), \quad (C1)$$

$$\bar{\Sigma}_a(z,t) = \bar{\Sigma}_a(z) + \delta\bar{\Sigma}_a(z,t), \quad (C2)$$

and

$$\phi(z,t) = \phi(z) + \delta\phi(z,t) . \quad (C3)$$

Substitution of Eqs. C1, C2 and C3 in Eq. 11 with the assumption that $\bar{D}(z)$, and $\bar{\Sigma}_a(z)$ are constant over the volume of sensitivity yields

$$\left[\bar{D} \frac{\partial}{\partial z} + \frac{\partial}{\partial z} \delta\bar{D}(z,t) \right] \frac{\partial}{\partial z} [\phi(z) + \delta\phi(z,t)]$$

$$[\bar{\Sigma}_a + \delta\bar{\Sigma}_a(z,t)] [\phi(z) + \delta\phi(z,t)] = \frac{1}{v_n} \frac{\partial}{\partial t} \delta\phi(z,t),$$

which in expanded form is

$$\begin{aligned} & \bar{D} \frac{\partial^2}{\partial z^2} \phi(z) + \frac{\partial}{\partial z} \delta\bar{D}(z,t) \frac{\partial}{\partial z} \phi(z) + \bar{D} \frac{\partial^2}{\partial z^2} \delta\phi(z,t) + \\ & \frac{\partial}{\partial z} \delta\bar{D}(z,t) \frac{\partial}{\partial z} \delta\phi(z,t) - [\bar{\Sigma}_a \phi(z) + \bar{\Sigma}_a \delta\phi(z,t) + \phi(z) \delta\bar{\Sigma}_a(z,t) \\ & + \delta\bar{\Sigma}_a(z,t) \delta\phi(z,t)] = \frac{1}{v_n} \frac{\partial}{\partial t} \delta\phi(z,t) . \end{aligned} \quad (C4)$$

At steady state Eq. C4 reduces to

$$\bar{D} \frac{\partial^2}{\partial z^2} \phi(z) - \bar{\Sigma}_a \phi(z) = 0, \quad (C5)$$

which is the usual steady state diffusion equation.

If Eq. C5 is subtracted from Eq. C4 the time varying part of the diffusion equation is found as

$$\begin{aligned} \bar{D} \frac{\partial^2}{\partial z^2} \delta\phi(z,t) + \frac{\partial}{\partial z} \delta\bar{D}(z,t) \frac{\partial}{\partial z} \delta\phi(z,t) + \\ \frac{\partial}{\partial z} \delta\bar{D}(z,t) \frac{\partial}{\partial z} \phi(z) - \bar{\Sigma}_a \delta\phi(z,t) - \phi(z) \delta\bar{\Sigma}_a(z,t) \\ - \delta\bar{\Sigma}_a(z,t) \phi(z) = \frac{1}{v_n} \frac{\partial}{\partial t} \delta\phi(z,t) . \end{aligned} \quad (C6)$$

If second order terms are ignored and it is assumed that $\phi(z)$ is a constant ϕ_z over the volume of sensitivity, Eq. C6 reduced to

$$\begin{aligned} \bar{D} \frac{\partial^2}{\partial z^2} \delta\phi(z,t) - \bar{\Sigma}_a \delta\phi(z,t) - \phi_z \delta\bar{\Sigma}_a(z,t) = \\ \frac{1}{v_n} \frac{\partial}{\partial t} \delta\phi(z,t) . \end{aligned} \quad (C7)$$

The Laplace transform of Eq. C7 is

$$\bar{D} \frac{\partial^2}{\partial z^2} \delta\phi(z,s) - \bar{\Sigma}_a \delta\phi(z,s) - \phi_z \delta\bar{\Sigma}_a(z,s) = \frac{s}{v_n} \delta\phi(z,s)$$

which after reordering becomes

$$\frac{\partial^2}{\partial z^2} \delta\phi(z, s) - \kappa^2 \delta\phi(z, s) = \frac{\phi z}{\bar{D}} \delta\bar{\Sigma}_a(z, s), \quad (C8)$$

where

$$\kappa^2 = \frac{\bar{\Sigma}_a + \frac{s}{v}}{\bar{D}}.$$

The solution to the corresponding homogeneous equation of Eq. C8 is

$$\delta\phi_h(z, s) = \zeta_1 e^{-\kappa z} + \zeta_2 e^{\kappa z}, \quad (C9)$$

where ζ_1 and ζ_2 are constants.

The particular solution of Eq. C8 can be found using the method of variation of parameters [5], which yields a solution of the form

$$\delta\phi_p(z, s) = \eta_1(z) e^{-\kappa z} + \eta_2(z) e^{\kappa z}, \quad (C10)$$

with conditions

$$\eta_1' = \frac{\xi_2 \psi}{W(\xi_1, \xi_2)}, \quad \eta_2' = \frac{\xi_1 \psi}{W(\xi_1, \xi_2)}, \quad (C11)$$

where

$$\xi_1 = e^{-\kappa z},$$

$$\xi_2 = e^{\kappa z},$$

$$\psi = \frac{\phi z}{\bar{D}} \delta\Sigma_a(z, s),$$

and

$$\begin{aligned} W(\xi_1, \xi_2) &= \xi_1 \xi_2' - \xi_1' \xi_2 \\ &= 2\kappa . \end{aligned}$$

Conditions C11 can thus be written as

$$\eta_1' = \frac{-e^{\kappa z} \frac{\phi_z}{\bar{D}} \delta \bar{\Sigma}_a(z, s)}{2\kappa},$$

and

$$\eta_2' = \frac{e^{-\kappa z} \frac{\phi_z}{\bar{D}} \delta \bar{\Sigma}_a(z, s)}{2\kappa},$$

which can be solved for η_1 and η_2 to give

$$\eta_1(z) = - \frac{\phi_z}{2\kappa \bar{D}} \int^z e^{\kappa x} \delta \bar{\Sigma}_a(x, s) dx ,$$

and

(C12)

$$\eta_2(z) = \frac{\phi_z}{2\kappa \bar{D}} \int^z e^{-\kappa x} \delta \bar{\Sigma}_a(x, s) dx .$$

The general solution of Eq. C8 is the sum of the homogeneous and particular solutions, which can be found by combining Eqs. C9, C10 and C12 to get

$$\begin{aligned}
\delta\phi(z,s) = & \zeta_1 e^{-\kappa z} + \zeta_2 e^{\kappa z} - \frac{\phi_z e^{-\kappa z}}{2\kappa\bar{D}} \int_0^z e^{\kappa x} \delta\bar{\Sigma}_a(x,s) dx \\
& + \frac{\phi_z e^{\kappa z}}{2\kappa\bar{D}} \int_z^\infty e^{-\kappa x} \delta\Sigma_a(x,s) dx . \quad (C13)
\end{aligned}$$

The first term in Eq. C13 becomes infinite as z goes to $-\infty$, and the second term becomes infinite as z goes to $+\infty$. Thus ζ_1 and ζ_2 must be taken to be zero. With appropriate limits on the integrals Eq. C13 can be written in the final form as

$$\begin{aligned}
\delta\phi(z,s) = & - \frac{\phi_z}{2\kappa\bar{D}} \int_{-\infty}^z e^{-\kappa(z-x)} \delta\Sigma_a(x,s) dx \\
& - \frac{\phi_z}{2\kappa\bar{D}} \int_z^\infty e^{-\kappa(x-z)} \delta\Sigma_a(x,s) dx , \quad (C14)
\end{aligned}$$

where the negative signs signify that an increase in absorption cross section reduces the flux.

To find a relationship between the fluctuations of macroscopic absorption cross section and fluctuations in void fraction a unit volume of the coolant fluid is assumed to have m_w and m_v mass units of water and void respectively. The density of the coolant in the unit cell is thus given by

$$\bar{\rho} = \frac{m_w + m_v}{I},$$

or

$$\bar{\rho} = \frac{\bar{\rho}_w V_w + \bar{\rho}_v V_v}{V_w + V_v}, \quad (C15)$$

where $\bar{\rho}_w$ and $\bar{\rho}_v$ are densities of water and void respectively, and V_w and V_v are volumes of water and void respectively.

From Eq. C15 the density of the coolant can be written as

$$\bar{\rho} = \bar{\rho}_w(1-\alpha) + \alpha\bar{\rho}_v,$$

or to a good approximation

$$\bar{\rho} \approx \bar{\rho}_w(1-\alpha), \quad (C16)$$

where α is the void fraction in the unit cell defined by

$$\alpha = \frac{V_v}{V_w + V_v}.$$

The macroscopic absorption cross section is by definition

$$\bar{\Sigma}_a = \frac{\bar{\rho} A_v \sigma_a}{M}, \quad (C17)$$

where A_v is the Avogadro's number, σ_a is the microscopic absorption cross section, and M is the molecular weight.

If Eq. C16 is used, Eq. C17 transforms to

$$\bar{\Sigma}_a = \frac{\bar{\rho}_w \sigma_{aw} A_v}{M} (1-\alpha)$$

or $\bar{\Sigma}_a = \text{constant} (1-\alpha)$. (C18)

If it is assumed that $\bar{\Sigma}_a$ and α have mean value and fluctuating parts, Eq. C18 can be written as

$$\bar{\Sigma}_a(z) + \delta\bar{\Sigma}_a(z,t) = \text{const.} [1-\alpha(z)-\alpha(z,t)],$$

which can be broken up into

$$\bar{\Sigma}_a(z) = \text{const.} [1-\alpha(z)],$$

and

$$\delta\bar{\Sigma}_a(z,t) = -\text{const.} \alpha(z,t),$$

or

$$\delta\bar{\Sigma}_a(z,s) = -C \alpha(z,s) . \quad \text{(C19)}$$

The negative sign in Eq. C19 denotes that an increase in void fraction decreases the macroscopic absorption cross section.

At this point the quantity

$$\kappa^2 = \frac{\bar{\Sigma}_a + \frac{s}{v_n}}{\bar{D}}$$

used in Eq. C8 is studied, and it is noted that since $v_n = 2200$ m/s for thermal neutrons a good approximation for κ^2 is

$$\kappa^2 \approx \frac{\bar{\Sigma}_a}{\bar{D}} = \frac{1}{L^2} = \mu^2, \quad (\text{C20})$$

where L is the thermal neutron diffusion length.

Application of Eqs. C19 and C20 in Eq. C14 yields

$$\begin{aligned} \delta\phi(z, s) = & C \frac{\phi_z}{2\mu\bar{D}} \int_{-\infty}^z e^{-\mu(z-x)} \alpha(x, s) dx \\ & + C \frac{\phi_z}{2\mu\bar{D}} \int_z^{\infty} e^{-\mu(x-z)} \alpha(x, s) dx. \end{aligned} \quad (\text{C21})$$

XIV. APPENDIX D: AUTO- AND CROSS-SPECTRAL DENSITIES
OF DETECTOR CURRENT FLUCTUATIONS DUE TO
FLUCTUATIONS IN LOCAL VOID FRACTION

The spectral density of detector current fluctuations is by definition given by

$$\phi_{i,\ell}(z,\omega) = i(z,\omega)i^*(z,\omega), \quad (D1)$$

which with the use of Eq. 14 becomes

$$\begin{aligned} \phi_{i,\ell}(z,\omega) = C\phi_z \int_{z-\frac{d}{2}}^{z+\frac{d}{2}} \left\{ \int_{-\infty}^{z'} e^{-\mu(z'-x')} \alpha(x',\omega) dx' + \right. \\ \left. \int_{z'}^{\infty} e^{-\mu(x'-z')} \alpha(x',\omega) dx' \right\} dz' \times \\ C\phi_z \int_{z-\frac{d}{2}}^{z+\frac{d}{2}} \left\{ \int_{-\infty}^{z''} e^{-\mu(z''-x'')} \alpha^*(x'',\omega) dx'' + \right. \\ \left. \int_{z''}^{\infty} e^{-\mu(x''-z'')} \alpha^*(x'',\omega) dx'' \right\} dz''. \end{aligned} \quad (D2)$$

Eq. D2 can be written in the expanded form as

$$\begin{aligned}
\phi_{i,\ell}(z,\omega) = C\phi_z^2 \int_{z-\frac{d}{2}}^{z+\frac{d}{2}} dz' \int_{z-\frac{d}{2}}^{z+\frac{d}{2}} dz'' \{ & \int_{-\infty}^{z'} dz' \int_{-\infty}^{z''} dx'' \\
& e^{-\mu(z'-x')} e^{-\mu(z''-x'')} + \\
& \int_{-\infty}^{z'} \int_{z''}^{\infty} e^{-\mu(z'-x')} e^{-\mu(x''-z'')} + \\
& \int_{z'}^{\infty} \int_{-\infty}^{z''} e^{-\mu(x'-z')} e^{-\mu(z''-x'')} + \\
& \left. \int_{z'}^{\infty} \int_{z''}^{\infty} e^{-\mu(x'-z')} e^{-\mu(x''-z'')} \right\} \alpha(x',\omega) \alpha^*(x'',\omega). \tag{D3}
\end{aligned}$$

The quantity $\alpha(x',\omega)\alpha^*(x'',\omega)$ is the cross-spectral density of void fraction fluctuations at axial positions x' and x'' , which with the aid of Eq. 10 can be written as

$$\psi_{\alpha;x',x''}(\omega) = C \frac{\alpha(x')\overline{v(x')}}{V(x'')} e^{-i\omega\tau_{x',x''}}. \tag{D4}$$

If it is assumed that $\alpha(x')$, $V(x'')$, and $\overline{v(x')}$ do not vary much over the detector length, they can be replaced by their respective values at position z , and Eq. D4 can be written as

$$\Psi_{\alpha, x'x''}(\omega) = C \frac{\alpha(z)\overline{v(z)}}{V(z)} e^{-i\omega \frac{x''-x'}{V(z)}} \quad (D5)$$

With the application of Eq. D5, Eq. D3 can be written as

$$\begin{aligned} \phi_{i,\ell}(z,\omega) = C\phi_z^2 \frac{\alpha(z)\overline{v(z)}}{V(z)} \int_{z-\frac{d}{2}}^{z+\frac{d}{2}} dz' \int_{z-\frac{d}{2}}^{z+\frac{d}{2}} dz'' \{ \\ e^{-\mu z'} \int_{-\infty}^{z'} e^{(\mu+i\frac{\omega}{V})x'} dx' \cdot e^{-\mu z''} \int_{-\infty}^{z''} e^{(\mu-i\frac{\omega}{V})x''} dx'' + \\ e^{-\mu z'} \int_{-\infty}^{z'} e^{(\mu+i\frac{\omega}{V})x'} dx' \cdot e^{\mu z''} \int_{z''}^{\infty} e^{-(\mu+i\frac{\omega}{V})x''} dx'' + \\ e^{\mu z'} \int_{z'}^{\infty} e^{-(\mu-i\frac{\omega}{V})x'} dx' \cdot e^{-\mu z''} \int_{-\infty}^{z''} e^{(\mu-i\frac{\omega}{V})x''} dx'' + \\ e^{\mu z'} \int_{z'}^{\infty} e^{-(\mu-i\frac{\omega}{V})x'} dx' \cdot e^{\mu z''} \int_{z''}^{\infty} e^{-(\mu+i\frac{\omega}{V})x''} dx'' \}, \quad (D6) \end{aligned}$$

where V is a mean bubble speed along the channel.

Eq. D6 integrates to

$$\begin{aligned}
\phi_{i,\ell}(z,\omega) = C\phi_z^2 \frac{\alpha(z)\overline{v(z)}}{V(z)} \{ & \\
\frac{1}{\mu^2 + \frac{\omega^2}{V^2}} \int_{z-\frac{d}{2}}^{z+\frac{d}{2}} e^{\frac{i\omega}{V}z'} dz' \int_{z-\frac{d}{2}}^{z+\frac{d}{2}} e^{-\frac{i\omega}{V}z''} dz'' + & \\
\frac{1}{(\mu + \frac{i\omega}{V})^2} \int_{z-\frac{d}{2}}^{z+\frac{d}{2}} e^{\frac{i\omega}{V}z''} dz' \int_{z-\frac{d}{2}}^{z+\frac{d}{2}} e^{-\frac{i\omega}{V}z''} dz'' + & \\
\frac{1}{(\mu - \frac{i\omega}{V})^2} \int_{z-\frac{d}{2}}^{z+\frac{d}{2}} e^{\frac{i\omega}{V}z'} dz' \int_{z-\frac{d}{2}}^{z+\frac{d}{2}} e^{-\frac{i\omega}{V}z''} dz'' + & \\
\frac{1}{\mu^2 + \frac{\omega^2}{V^2}} \int_{z-\frac{d}{2}}^{z+\frac{d}{2}} e^{\frac{i\omega}{V}z'} dz' \int_{z-\frac{d}{2}}^{z+\frac{d}{2}} e^{-\frac{i\omega}{V}z''} dz'' \}. & \tag{D7}
\end{aligned}$$

Eq. D7 factors out and integrates to

$$\begin{aligned}
\phi_{i,\ell}(z,\omega) = C\phi_z^2 \frac{\alpha(z)\overline{v(z)}}{V(z)\frac{\omega}{V^2}} \cdot \frac{4\mu^2}{(\mu^2 + \frac{\omega^2}{V^2})^2} \cdot \\
[e^{\frac{i\omega}{V}(z+\frac{d}{2})} - e^{\frac{i\omega}{V}(z-\frac{d}{2})}] [e^{-\frac{i\omega}{V}(z+\frac{d}{2})} - e^{-\frac{i\omega}{V}(z-\frac{d}{2})}],
\end{aligned}$$

which simplifies to

$$\Phi_{i,l}(z,\omega) = C\phi_z^2 \frac{\alpha(z)\overline{v(z)}}{V(z)} \frac{4\mu^2}{(\mu^2 + \frac{\omega^2}{V^2})^2} \frac{[1 - \cos(\frac{\omega d}{V})]}{\frac{\omega^2}{V^2}}. \quad (D8)$$

Eq. D8 can be written in the alternate form

$$\overline{\Phi}_{i,l}(z,\omega) = C \frac{\alpha(z)\overline{v(z)}}{V(z)} H_\mu(\omega) H_d(\omega), \quad (D9)$$

where

$$H_\mu(\omega) = \frac{1}{(1 + \omega^2 \tau_\mu^2)^2}, \quad (D10)$$

and

$$H_d(\omega) = \frac{\sin^2(\omega \tau_d)}{(\omega \tau_d)^2}, \quad (D11)$$

where

$$\tau_\mu = \frac{1}{\mu V},$$

and

$$\tau_d = \frac{d}{2V}$$

are time constants associated with the volume of sensitivity and detector length respectively, and where

$$\overline{\Phi}_{i,l}(z,\omega) = \frac{\Phi_{i,l}(z,\omega)}{\overline{I}^2(z)}$$

is the auto-spectral density of detector current fluctuations, due to fluctuations in void fraction, normalized by the square of mean detector current output, which is proportional to mean neutron flux.

The cross-spectral density function of detector current fluctuations, due to fluctuations in void fraction for two detectors centered at positions z_1 and z_2 along the channel is by definition given by

$$\Psi_{i,l;z_1,z_2}(\omega) = i(z_1,\omega)i^*(z_2,\omega) . \quad (D12)$$

With the application of Eq. 14, Eq. D12 can be written as

$$\begin{aligned} \Psi_{i,l;z_1,z_2}(\omega) = C\phi_{z_1} \int_{z_1-\frac{d}{2}}^{z_1+\frac{d}{2}} \left\{ \int_{-\infty}^{z'} e^{-\mu(z'-x')} \alpha(x',\omega) dx' + \right. \\ \left. \int_{z'}^{\infty} e^{-\mu(x'-z')} \alpha(x',\omega) dx' \right\} dz' \times \\ C\phi_{z_2} \int_{z_2-\frac{d}{2}}^{z_2+\frac{d}{2}} \left\{ \int_{-\infty}^{z''} e^{-\mu(z''-x'')} \alpha^*(x'',\omega) dx'' + \right. \\ \left. \int_{z''}^{\infty} e^{-\mu(x''-z'')} \alpha^*(x'',\omega) dx'' \right\} dz'' . \quad (D13) \end{aligned}$$

Eq. D13 can be integrated in the same way as Eq. D2 with the final result given by

$$\bar{\Psi}_{i, \ell; z_1, z_2}(\omega) = C \frac{\alpha(z_1) \bar{v}(z_1)}{V(z_2)} H_{\mu}(\omega) H_d(\omega) e^{-i\omega T_{12}}, \quad (D14)$$

where

$$\bar{\Psi}_{i, \ell; z_1, z_2}(\omega) = \frac{\Psi_{i, \ell; z_1, z_2}(\omega)}{\bar{I}(z_1) \bar{I}(z_2)}$$

is the normalized cross-spectral density function, and

$$T_{12} = \frac{z_2 - z_1}{\bar{V}_{12}}, \quad z_2 > z_1 \quad (D15)$$

is the bubble travel time between positions z_1 and z_2 along the channel, where \bar{V}_{12} is the mean bubble speed between z_1 and z_2 .

XV. APPENDIX E: ALGORITHM FOR THE CALCULATION
OF SPECTRA

In this appendix the steps necessary to calculate desired spectra from time series data are explained.

Due to limited available in-core memory capacity of the ALRR PDP-15 computer, the size of the time series data sequence, N , from either channel was limited to 512 words. With the anti-aliasing filters set at 10 Hz, and the associated analog to digital sampling rate, f_s , set at 25.6 samples per second, the length of each data segment, T , in either channel was fixed at 20 seconds.

Thus, the physical limitations of the system dictate that the time interval between sample values is given by

$$h = \frac{1}{f_s} = \frac{1}{25.6} = 0.0390625 \text{ s}, \quad (\text{E1})$$

the Nyquist frequency or folding frequency is given by

$$f_c = \frac{f_s}{2} = 12.8 \text{ Hz}, \quad (\text{E2})$$

and the discrete spectral points are separated by the resolution bandwidth given by

$$B_e = \frac{1}{T} = \frac{1}{20} = 0.05 \text{ Hz} . \quad (\text{E3})$$

The first step in the algorithm is to calculate the mean value of each data sequence, and subtract it from

the data to obtain zero-mean time series data.

The second step involves application of a window function to the data to reduce the amplitude of side bands in the calculated spectra. It was found experimentally that the best window function for the present work is a complete cosine squared function [20] given by

$$w(t) = \cos^2 \frac{\pi t}{T} \quad -\frac{T}{2} \leq t \leq \frac{T}{2} \quad (\text{E4})$$

where t has discrete values given by

$$t = \pm nh \quad n = 0, 1, 2, \dots, \frac{N}{2} - 1 . \quad (\text{E5})$$

The Fourier transform of the two real-valued records is computed simultaneously by inserting one record $x(n)$ as the real part and one record $y(n)$ as the imaginary part of a complex record $z(n)$, or

$$z(n) = x(n) + iy(n) \quad n = 0, 1, 2, \dots, N-1 . \quad (\text{E6})$$

The Fourier transform of $z(n)$ is now computed via FFT to give the transforms

$$Z(k) \quad \text{for } k = 0, 1, 2, \dots, N-1 .$$

The two real-valued records $x(n)$ and $y(n)$ have Fourier transforms $X(k)$ and $Y(k)$ respectively given by

$$X(k) = \frac{Z(k) + Z^*(N-k)}{2}, \quad (E7)$$

and

$$Y(k) = \frac{Z(k) - Z^*(N-k)}{2i}, \quad (E8)$$

where the Nyquist cut-off frequency occurs when $k = \frac{N}{2}$, so that unique results occur only for $k = 0, 1, 2, \dots, \frac{N}{2}$.

The raw estimates of the auto power spectral densities are given by

$$\tilde{G}_x(k) = |X(k)|^2, \quad (E9)$$

and

$$\tilde{G}_y(k) = |Y(k)|^2. \quad (E10)$$

The raw estimate of the cross power spectral density is given by

$$\begin{aligned} \tilde{G}_{xy}(k) &= X^*(k)Y(k) \\ &= \tilde{C}_{xy}(k) - i\tilde{Q}_{xy}(k). \end{aligned} \quad (E11)$$

The discrete frequency points are given by

$$f_k = \frac{k}{T}. \quad (E12)$$

The transforms $X(k)$, $Y(k)$ and $Z(k)$ can be expressed in terms of their real and imaginary parts as:

$$X(k) = a(k) + ib(k),$$

$$Y(k) = c(k) + id(k),$$

and

$$Z(k) = e(k) + if(k).$$

With the application of Eqs. E7 and E8, the real and imaginary parts of $X(k)$ and $Y(k)$ are given by

$$a(k) = [e(k)+e(N-k)]/2,$$

$$b(k) = [f(k)-f(N-k)]/2,$$

$$c(k) = [f(k)+f(N-k)]/2,$$

and

$$d(k) = [e(N-k)-e(k)]/2.$$

The raw estimates of APSD functions of Eqs. E9 and E10 are then given by

$$\tilde{G}_x(k) = a^2(k) + b^2(k) ,$$

and

$$\tilde{G}_y(k) = c^2(k) + d^2(k) .$$

The raw estimates of the real and imaginary components of the CPSD function of Eq. E11 are given by

$$\tilde{C}_{xy}(k) = a(k)c(k) + b(k)d(k),$$

and

$$\tilde{Q}_{xy}(k) = b(k)c(k) - a(k)d(k).$$

The above estimates are raw estimates of the spectra, where each estimate is governed by a χ^2 distribution with 2 degrees of freedom. To reduce statistical variability of the spectra the results from q separate time slices of length T are averaged. The time segment averaged spectra are then given by

$$\hat{G}_k = \frac{1}{q} [\tilde{G}_{k,1} + \tilde{G}_{k,2} + \dots + \tilde{G}_{k,q}], \quad (\text{E13})$$

which is applied to \tilde{G}_x , \tilde{G}_y , \tilde{C}_{xy} , and \tilde{Q}_{xy} , separately.

The quantity \hat{G}_k is a χ^2 variable with $2q$ degrees of freedom, and normalized standard error of

$$\varepsilon' = \sqrt{1/q}. \quad (\text{E14})$$

The frequency resolution is a constant value throughout the spectrum as given by Eq. E3. Since lower frequency resolution can be tolerated at the higher frequency end of the spectra, averaging of neighboring frequency components of the spectral estimates is desirable.

It was decided to average two neighboring spectral points between 2 Hz to 4 Hz, and four neighboring spectral points between 4 Hz and 10 Hz. The averaged spectral points are considered to represent the value of the spectrum at the midpoint of the smoothed frequency interval.

Since spectral estimates at frequency spacing $\frac{1}{T}$ are essentially uncorrelated, then if l neighboring frequency

components are averaged, the smoothed spectral estimate is given by

$$G(k) = \frac{1}{\ell} [\hat{G}_k + \hat{G}_{k+1} + \dots + \hat{G}_{k+\ell-1}], \quad (\text{E15})$$

which is a χ^2 variable with $2\ell q$ degrees of freedom, and normalized standard error of

$$\epsilon = \sqrt{1/\ell q}. \quad (\text{E16})$$

The frequency resolution, Δf , and the normalized standard error, ϵ , for the measured spectra are given in Table E-1.

Table E-1. Frequency resolutions and normalized standard errors for the measured spectra

Frequency range, Hz	Frequency resolution, Hz	ℓ	q	ϵ
0-2	0.05	1	64	0.125
2-4	0.10	2	64	0.0884
4-10	0.20	4	64	0.0625

Finally, to obtain normalized spectra, the following normalization factors are used

$$\begin{aligned}
 NF_x &= \frac{1}{0.5} \frac{1}{CF^2} \frac{1}{DC_x^2} \frac{1}{G_x^2} \frac{2h}{N}, \\
 NF_y &= \frac{1}{0.5} \frac{1}{CF^2} \frac{1}{DC_y^2} \frac{1}{G_y^2} \frac{2h}{N}, \tag{E17}
 \end{aligned}$$

and

$$NF_{xy} = \frac{1}{0.5} \frac{1}{CF^2} \frac{1}{DC_x} \frac{1}{DC_y} \frac{1}{G_x G_y} \frac{2h}{N},$$

where $\frac{1}{0.5}$ is a correction factor for the cosine squared window function, CF is the analog to digital converter conversion factor, DC_x and DC_y are the DC voltages of signals x and y, G_x and G_y are amplification gains of signals x and y, and $\frac{2h}{N}$ is a transformation factor.

The normalized spectra are now given by

$$NAAPSD (f_k) = NF_x G_x(k), \tag{E18}$$

$$NBAPSD (f_k) = NF_y G_y(k), \tag{E19}$$

and

$$NCPSD (f_k) = NF_{xy} [C_{xy}^2(k) + Q_{xy}^2(k)]^{1/2}, \tag{E20}$$

where NAAPSD and NBAPSD are the normalized auto-power spectral densities of current fluctuations of detectors A and B, and NCPSD is the normalized cross spectral density of current fluctuations of detectors A and B.

The phase of the cross spectral density function is found from the relation

$$\text{PHASE}(f_k) = \frac{180.}{\pi} \tan^{-1} \left[\frac{Q_{xy}(k)}{C_{xy}(k)} \right], \quad (\text{E21})$$

with the correct quadrant determined from the signs of Q_{xy} and C_{xy} .

The input-output transfer function is found from the relation

$$\text{TRNSFN}(f_k) = \frac{\text{NCPSD}(f_k)}{\text{NAAPSD}(f_k)}. \quad (\text{E22})$$

The coherence function is found using the relation

$$\text{CHRNCF}(f_k) = \frac{C_{xy}^2(k) + Q_{xy}^2(k)}{G_x(k) \cdot G_y(k)}, \quad (\text{E23})$$

where it should be emphasized that G_x , G_y , C_{xy} and Q_{xy} are segment averaged and frequency smoothed quantities.

The normalized mean square value is estimated by

$$\text{NMSV} = B e^{\sum_{k=1}^{N/2} \text{NAAPSD}(k)} \quad (\text{E24})$$

with a normalized standard error of

$$\epsilon'' = \sqrt{1/q}. \quad (\text{E25})$$